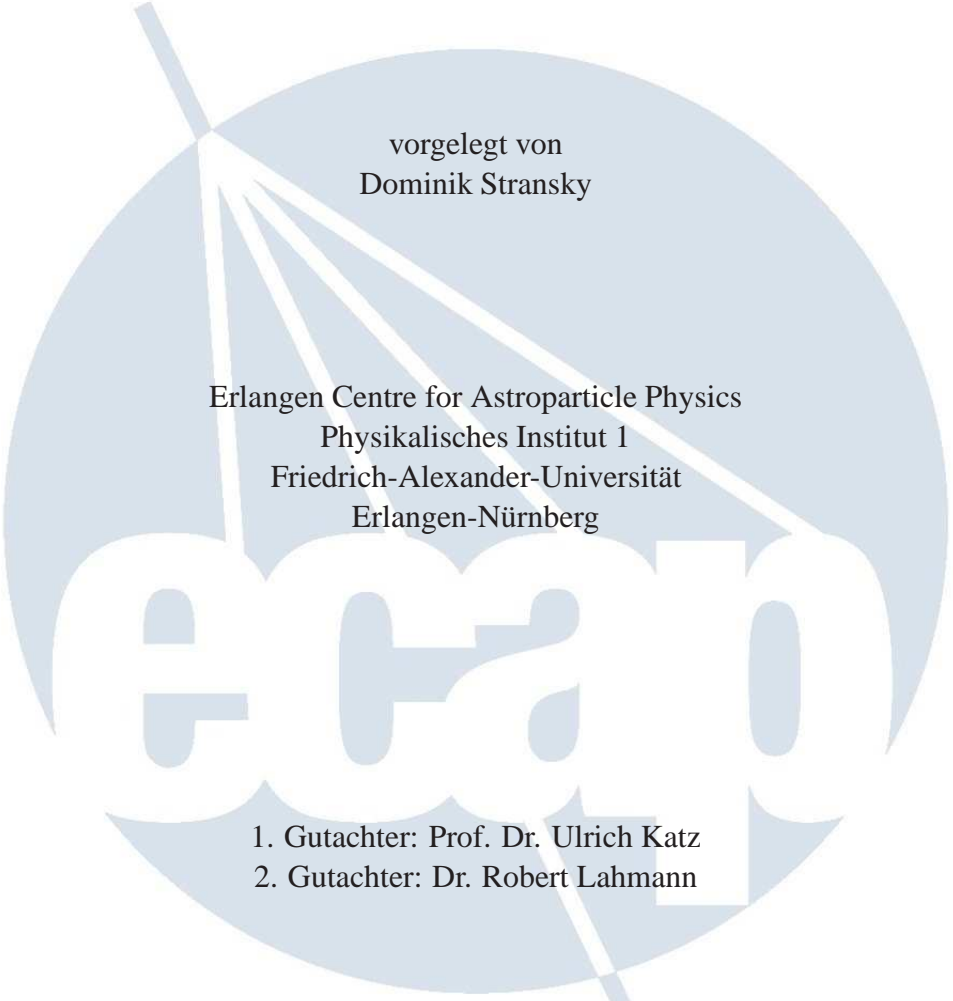# Cosmogenic Neutrinos
in the Deep-Sea Neutrino Telescope
KM3NeT

Diplomarbeit

vorgelegt von
Dominik Stransky

Erlangen Centre for Astroparticle Physics
Physikalisches Institut 1
Friedrich-Alexander-Universität
Erlangen-Nürnberg

1. Gutachter: Prof. Dr. Ulrich Katz
2. Gutachter: Dr. Robert Lahmann

Tag der Abgabe: 26. 07. 2012

Contents

Chapter 1

Motivation

Why is the cosmogenic neutrino flux so important to physics? The short answer would be because its verification would reveal essential information about ultra high energy cosmic rays (UHECR) and thus about the universe. For the long answer one should know how the cosmogenic neutrino flux is created and what the current unknowns are concerning the cosmic rays. First evidence of cosmic rays was found by Victor Hess (1911-1912) as he measured an increase of the ionizing radiation with height in the atmosphere during balloon flights at altitudes of up to 5 km. Since then, as the field of astronomy expanded creating the branches of astrophysics and astroparticle physics, cosmic rays have been investigated in every respect, revealing large parts of their spectrum, composition and sources (see section 2). The most energetic observed events have energies of up to $10^{11.5}$ GeV [1] corresponding to 50 Joule 'carried' by just one particle. However, until now, not many ultra high energy events have been observed leaving behind great uncertainties in this energy regime.

Astrophysical neutrinos are produced when cosmic rays interact with matter or radiation fields on the way through the cosmos (see section 3.1). UHECR interactions with the cosmic microwave background (CMB) create the so-called Greisen-Zatsepin-Kuzmin (GZK) cutoff [2, 3] in the energy spectrum of the cosmic rays. When UHECR interact with interstellar and intergalactic photon fields, a special kind of neutrino flux is generated, named the 'cosmogenic neutrino flux', the investigation of which this work is about. Many authors made considerations and calculated possible cosmogenic neutrino spectra [4–7] which highly depend on the characteristics of the UHECR. However, as the UHECR interactions during cosmic ray propagation alter the cosmic rays measured at earth (primary and secondary cosmic rays), creating for instance the aforementioned GZK cutoff, the cosmogenic spectrum mainly depends on the characteristics of the cosmic radiation as it is produced at the sources, the so-called primordial cosmic rays [8] (section 3.2). The parameter space, like for instance the chemical composition of these primordial cosmic rays is what a measurement of the cosmogenic neutrino flux can greatly constrain.

Due to their special characteristics like the low interaction probability (chapter 4), neutrinos are capable of communicating to us unique information about the primordial cosmic rays, especially about the mystery which sources and processes are able to accelerate cosmic rays to the highest energies. This is because they are, unlike most cosmic rays, unaffected by intergalactic magnetic fields and may cross also cosmic gas clouds, unlike gamma rays, virtually undisturbed. On the other hand the same neutrino characteristics force scientists to build huge structures, like the future deep-sea neutrino telescope KM3NeT, in the scope of which the study was done, with a planned instrumented volume of approximately 3 km^3 (section 5.3). The major background for the detection of diffuse cosmic neutrinos like the cosmogenic neutrino flux, is produced when cosmic rays interact in the atmosphere forming the atmospheric neutrino flux (section 3.3).

High energy neutrinos are detected by measuring the Cherenkov light which is produced from charged secondary particles generated in neutrino interactions. Depending on these secondaries, and

thus on the neutrino flavour and interaction type, neutrino events differ in their appearance in the detector (section 5.1). The most important measure of the performance of a detector is its effective area. This quantity includes the detection efficiency and determines the expected event rates in the neutrino telescope. For the determination of the effective area, simulations of all possible event types in all relevant energy ranges are necessary.

In the scope of this thesis, presented in chapter 6, simulation tools from ANTARES, the first working deep-sea neutrino telescope and KM3NeT's predecessor (section 5.2), are investigated in the context of their capability of simulating highest energy neutrino events. In addition first simulations with the simulation tool Geant4 were performed, which will replace a part of the hitherto existing event simulation software framework of KM3NeT.

The main part of this work, which is the calculation of the expected event rates of the cosmogenic neutrino flux in KM3NeT, is presented in chapter 7. As mentioned, the expected event rates depend on the effective area, the determination of which for the ultra high energy regime goes beyond the scope of this work. Therefore a perfect detection efficiency is assumed for the event rate calculation. However, first considerations regarding the detectability of high energy events and thus the effective area are made and presented in section 7.1. The work concludes with a short outlook on the relevance of the cosmogenic neutrino flux to astroparticle physics.

Chapter 2

Cosmic Rays

Cosmic rays are a fundamental ingredient for the production of astrophysical high energy neutrinos. As the resulting neutrino fluxes depend highly on the characteristics of cosmic rays, like their spectrum, chemical composition and their sources, the measurement of the resulting neutrino fluxes can give valuable information about current uncertainties in these characteristics. Therefore, the known features of the cosmic rays will be described shortly in the following together with the main unknowns.

2.1 Spectrum and Sources

The spectrum of cosmic rays measured on earth is shown in Figure 2.1. Above $10\,\mathrm{GeV}$ the spectrum can be characterized by a broken power law:

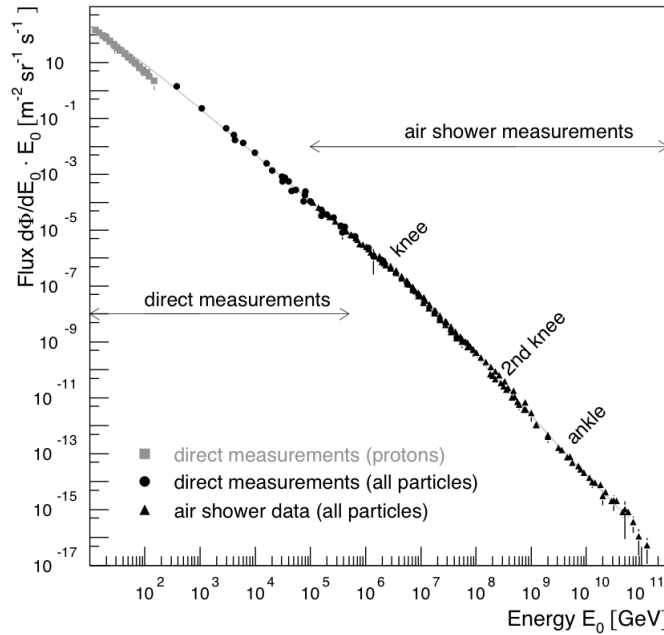$$\frac{\mathrm{d}N}{\mathrm{d}E} = N_0 E^{-\gamma} \tag{2.1}$$

Figure 2.1: Direct and indirect measurements of the energy weighted cosmic ray spectrum. The main features of the spectrum are indicated including the two knees and the ankle. Around $60\,\mathrm{EeV}$ ($6 \cdot 10^{11}\,\mathrm{GeV}$) the GZK cutoff sets in. Figure taken from [9].
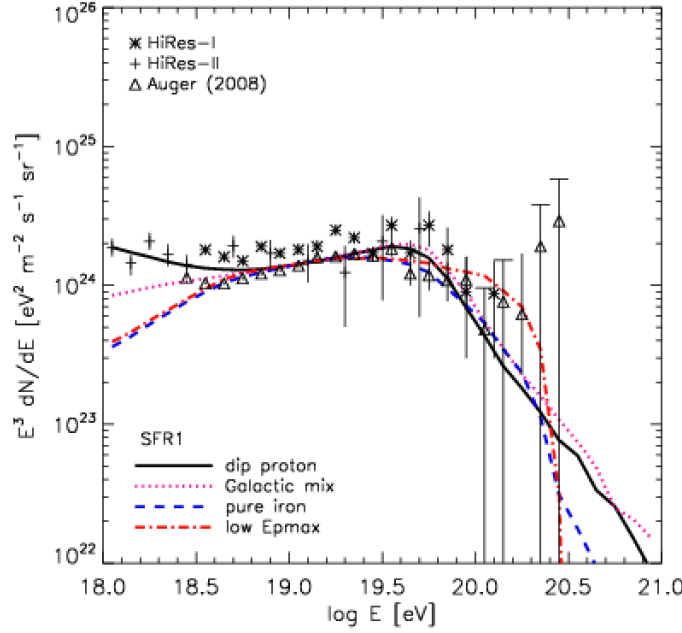
Figure 2.2: The high energy end of the cosmic ray spectrum as measured by HiRes-I and HiRes-II [12] and the Auger Observatory [1] weighted with E^3. Adjusted to the data are propagated cosmic ray spectra from simulations which are done for different source evolution models by Kotera et al. [7] where the Figure is taken from. See also section 3.2.1.

where γ is the spectral index and N_0 is a normalization constant both, determined by the cosmic ray measurements. From the measurements follow two major breaks in the spectrum where the power index changes. At about 4 PeV, at the so-called knee, the index changes from $\gamma \approx 2.7$ to $\gamma \approx 3.2$ [10]. There might be a second knee at roughly 400 PeV where the spectrum gets even steeper. One interpretation of the knees is the galactic containment, which describes that charged particles, until a certain energy that depends on the charge number Z, are trapped in the galaxy by the galactic magnetic field. The first knee might then be a 'proton knee' while the second one would result from heavier particles with higher Z. At the second major break, the so-called ankle at about 3 EeV, the spectrum gets harder again to $\gamma \approx 2.8$. The ankle is commonly interpreted as the galactic to extragalactic transition, i.e. the energy region where cosmic rays coming from outside of our galaxy begin to predominate over those coming from within our galaxy. However, models exist in which this transition already begins at the second knee[1]. Around 60 EeV the Greisen-Zatsepin-Kuzmin (GZK) cutoff [2, 3] sets in and the spectrum drops exponentially. This strong suppression is explained by the fact that ultra high energy cosmic rays lose energy in the interaction with the cosmic microwave background (CMB). This interaction eventually leads to the production of the cosmogenic neutrino flux which therefore depends highly on the characteristics of the highest energy cosmic rays. Predictions for the cosmogenic neutrinos are made by modelling the ultra high energy cosmic rays at the sources and simulating their propagation through the cosmos. The mean free path for the reaction of cosmic ray protons with the photon background is around 10 Mpc, meaning that all cosmic rays contributing to the formation of the cosmogenic neutrino flux, are of extragalactic origin. After the simulated propagation, when reaching earth, the modelled cosmic rays have to fit the high energy end of the spectrum measured at earth as it is believed to be solely composed of extragalactic cosmic rays. This high energy end is shown in detail in Figure 2.2. More on the cosmogenic neutrino

---

[1]See [11] for more detail on different transition models, and section 3.2 for the effect of different transition models on the cosmogenic neutrino flux.

flux and how it is affected by cosmic ray parameters is presented in section 3.2.

Galactic cosmic rays are believed to be accelerated by the Fermi mechanism which describes the stochastic energy gain of charged particles in plasma shock waves, e.g. in supernova remnants. Other acceleration mechanisms besides the Fermi acceleration are present in the vicinity of pulsars where the particles gain their energy in the enormous magnetic fields that are generated by the pulsars or in binary systems, consisting of a massive object like a neutron star or pulsar and a normal star. Matter from the normal star is dragged onto the massive object forming an accretion disk of hot plasma and producing strong electromagnetic fields in which particles are accelerated to very high energies [8]. Known candidates for galactic sources are believed to be able to accelerate single particles to energies of up to around 1 EeV at maximum.

Expected sources of particles up to the highest energies are active galactic nuclei (AGN) and gamma ray bursts (GRB). In an AGN, similar to the processes in a binary system, matter forming an accretion disk spirals towards a super massive black hole and is eventually, if not sucked into the black hole, emitted in high relativistic jets perpendicular to the accretion disk. It is assumed that due to the processes in these active nuclei and jets, single particles can reach the highest energies. Because of the enormous mass of the central black hole, these processes are powerful enough to produce luminosities almost as large as the entire host galaxy. On the other hand, GRBs are far from being understood. They appear as short bursts of gamma rays with durations of some milliseconds to several hundred seconds. They occur suddenly and unpredictably. A possible explanation for these ultra high-energy events is for instance the collision of two massive compact objects, e.g. neutron stars and black holes, or an enormous supernova explosion, called hypernova. For more details on GRBs and AGN see [8].

2.2   Chemical Composition

The chemical composition of cosmic rays has been measured copiously in the low energy regime. However, it is hard to determine in the energy regime where the cosmic particles can only be detected by their production of secondary particles, i.e. by indirect measurement methods. In the lower energy domain ($< 1\,\mathrm{GeV}$) the abundances are about 85 % for protons, 12 % for α particles and only 3 % for the total of all heavier nuclei, which is very similar to the composition in the solar system [8]. With rising energy the composition seems to get heavier. For example at energies below the knee the composition is mixed, i.e. the light component, which is the sum of the proton and α particle abundances, is roughly 54 % [10]. At the highest energies ($> 1\,\mathrm{EeV}$), results from the Pierre Auger Observatory [13] at the southern hemisphere indicate that the composition also seems to get heavier with rising energy, while results from the Telescope Array Experiment [14] favour a pure proton composition at these energies. The chemical composition at the highest energies is of big importance for the production of the cosmogenic neutrino flux (see section 3.2).

Chapter 3

Neutrino Production and Neutrino Fluxes

Astrophysical neutrinos are produced in cosmic ray interactions. The generated neutrino fluxes can be categorized into two different types, that is point-like or diffuse. Point-like fluxes are generated when the cosmic rays directly interact at the acceleration site, for example in supernova remnants or binaries. More about point-like neutrino sources can be read for example in [15]. This chapter begins with a description of the processes leading to neutrino production. Afterwards the cosmogenic and the atmospheric neutrino flux, two types of diffuse fluxes, are presented. While the investigation of the cosmogenic neutrino flux within the scope of KM3NeT represents the main goal of this work, the atmospheric neutrino flux forms the major background in the search for cosmogenic neutrinos.

3.1 Basic Production Processes

The basic process for the production of high energy neutrinos is the decay of charged pions and kaons:

$$\pi^{\pm}(K^{\pm}) \rightarrow \mu^{\pm} + \overset{(-)}{\nu_{\mu}} \tag{3.1}$$

and the subsequent decay of the muons:

$$\mu^{\pm} \rightarrow e^{\pm} + \overset{(-)}{\nu_e} + \overset{(-)}{\nu_{\mu}} \tag{3.2}$$

The short lived mesons are produced when high energy cosmic rays interact with matter (process (3.3)) or photon fields (process (3.4)) at their source forming neutrino point-like fluxes with galactic and extra galactic origin or in the earth's atmosphere forming the atmospheric background neutrino flux. In the processes, X represents any particles consistent with conservation laws.

$$p + X \rightarrow \begin{cases} \pi^0 + X \\ \pi^{\pm} + X \end{cases} \tag{3.3}$$

Another possibility is the interaction of high energy cosmic rays with the interstellar or intergalactic medium thus generating diffuse neutrino fluxes. Here, the reaction of UHECR with the cosmic photon background has to be emphasized which leads to the production of the cosmogenic neutrino flux (section 3.2).

$$p + \gamma \rightarrow \begin{cases} p + \pi^0 \\ n + \pi^+ \end{cases} \tag{3.4}$$

From this process, the threshold energy for protons can be calculated from four-momentum conservation assuming head-on collisions with the photons:

$$(q_p + q_\gamma)^2 = E_p^2 + 2\,E_p\,E_\gamma + E_\gamma^2 - p_p^2 + 2\,p_p\,p_\gamma - p_\gamma^2 \tag{3.5}$$

$$\approx m_p^2 + 4\,E_p\,E_\gamma \tag{3.6}$$

$$\overset{!}{=} (m_n + m_{\pi^+})^2 \tag{3.7}$$

$$= m_n^2 + 2\,m_n\,m_{\pi^+} + m_{\pi^+}^2 \tag{3.8}$$

with q_p, q_γ as the four-momenta of the proton and photon, respectively, $m_p \approx m_n$ and m_{π^+} as the nucleon and pion masses, E_p and E_γ as the proton and photon energies, p_p and p_γ as the magnitudes of the proton and photon momenta, with the approximation $p_p \approx E_p$ such that $2p_p p_\gamma \approx 2E_p E_\gamma$. The threshold proton energy for the reaction with a CMB photon at wavelength $\lambda_{\max} = b/T_{\mathrm{CMB}}$ is then given by ($b = 2.9 \cdot 10^{-3}\,\mathrm{m}/\mathrm{K}$ as the Wien displacement law constant, $T_{\mathrm{CMB}} = 2.7\,\mathrm{K}$ as the mean temperature of the CMB)

$$E_p \approx \frac{2\,m_n\,m_{\pi^+} + m_{\pi^+}^2}{4\,E_\gamma} = \frac{2\,m_n\,m_{\pi^+} + m_{\pi^+}^2}{4\,h\,T_{\mathrm{CMB}}\,/\,b} = 62\,\mathrm{EeV} \tag{3.9}$$

with $h = 4.1 \cdot 10^{-15}\,\mathrm{eV\,s}$ as Planck's constant, $m_n = 0.94\,\mathrm{GeV}$, $m_{\pi^+} = 0.14\,\mathrm{GeV}$.

From the neutrino production processes above follows a neutrino flavour ratio at the production site of $\Phi_{\nu_e} : \Phi_{\nu_\mu} : \Phi_{\nu_\tau} = 1:2:0$ for the neutrino fluxes Φ_ν. During propagation over cosmological distances, neutrinos of different flavour oscillate, leading to a ratio of $\Phi_{\nu_e} : \Phi_{\nu_\mu} : \Phi_{\nu_\tau} = 1:1:1$ observed at the earth. For further details on neutrino oscillation see for example [16, 17].

An upper bound for the diffuse neutrino flux from extra-galactic optically thin sources is given by

$$E^2 \frac{\mathrm{d}N}{\mathrm{d}E} = 1 \sim 5 \cdot 10^{-8} \frac{\mathrm{GeV}}{\mathrm{cm}^2\,\mathrm{s}\,\mathrm{sr}} \tag{3.10}$$

calculated by Waxman and Bahcall taking into account current high energy cosmic ray measurements and assuming a generic E^{-2} injection spectrum which generates the same energy density as the charged cosmic ray flux [18, 19].

3.2   The Cosmogenic Neutrino Flux

The so-called cosmogenic neutrinos are produced when ultra high energy cosmic rays interact with the cosmic photon background (see equation (3.4)). This includes the cosmic microwave background (CMB) and photons from the infrared regime to the optically up to the ultraviolet regime (IR-UV). The different wavelength regions have different impacts on the shape of the resulting neutrino flux. An example of the general shape of the cosmogenic neutrino flux is pictured in Figure 3.1. The IR-UV and CMB contributions generally form two distinct bumps in the cosmogenic spectrum while the contribution from the beta decay of neutrons produced in photo-disintegration processes of heavier nuclei present in cosmic rays, $n \to p\,e^-\,\bar{\nu}_e$, is less significant.

As the cosmic rays producing the cosmogenic neutrinos arise from very distant sources predictions of the cosmogenic neutrino flux not only have to take into account the general characteristics of the cosmic rays (see chapter 2) but also the source emissivity evolution and the photon background evolution with the redshift, i.e. with the age of the universe. In general, there are five major issues that highly affect the spectrum of the cosmogenic neutrino flux:
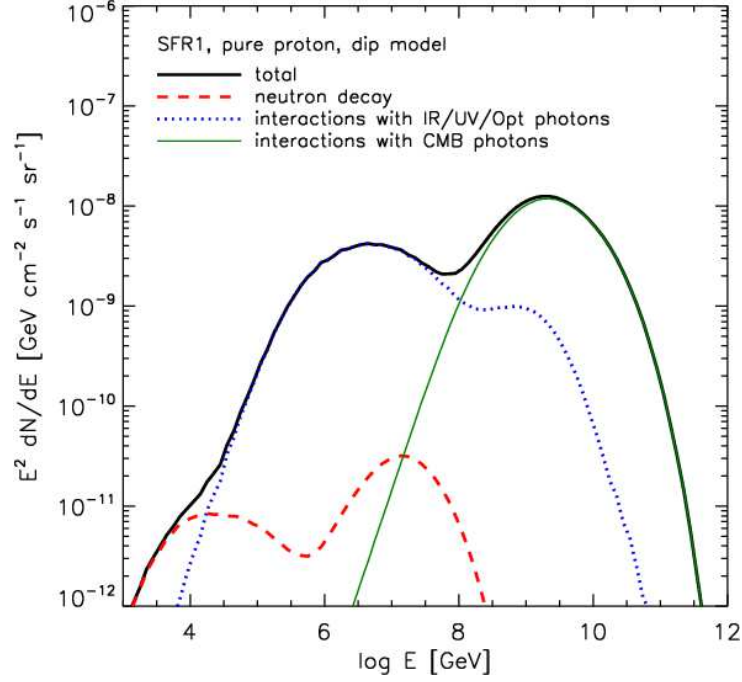
Figure 3.1: Different impacts of the different neutrino production channels on the cosmogenic neutrino flux, considering all neutrino flavours. The interactions of the cosmic rays with IR-UV photons (blue dashed line) and the CMB (green solid line) form two distinct bumps in the total cosmogenic neutrino flux spectrum (black solid line) peaked at $E_\nu \approx 5\,\mathrm{PeV}$ and $E_\nu \approx 5\,\mathrm{EeV}$, respectively. The neutron channel (red dashed line) only contributes a negligible fraction in the presented case (pure proton composition). However, for heavier chemical compositions the neutron channel contribution rises. In this plot a pure proton composition with a dip transition model and a star formation rate type source emissivity evolution is assumed. For more information on that see the description in the text. Figure taken from [7].

- the evolution of the cosmic photon background

- the source emissivity evolution

- the galactic to extragalactic transition model of the cosmic rays

- the chemical composition of the ultra high energy cosmic rays

- the maximum acceleration energy of the cosmic rays in the source

The evolution of the IR-UV photon background with redshift is directly correlated to the star formation rate and its evolution while the CMB photon density increases with redshift z in $(1 + z)^3$ [7]. The poor knowledge of the other four points results in great uncertainties for the prediction of the cosmogenic neutrino flux. Six models of cosmogenic neutrino fluxes ranging from very low to very high predictions are used in this work. The data for these models are taken from [7]. They are shown in Figure 3.2 and represent always the sum of all neutrino flavours. Due to neutrino oscillation as mentioned in section 3.1, the neutrino flavour ratios are $\Phi_{\nu_e} : \Phi_{\nu_\mu} : \Phi_{\nu_\tau} = 1 : 1 : 1$ on their arrival at earth.

In the following the parameter space of the above mentioned aspects and the effect of various models will be described shortly. The description mainly follows Kotera et al. [7], who made detailed studies and simulations of the production of the cosmogenic neutrino flux. Visit this reference also for more detail on the different models considered in this work.
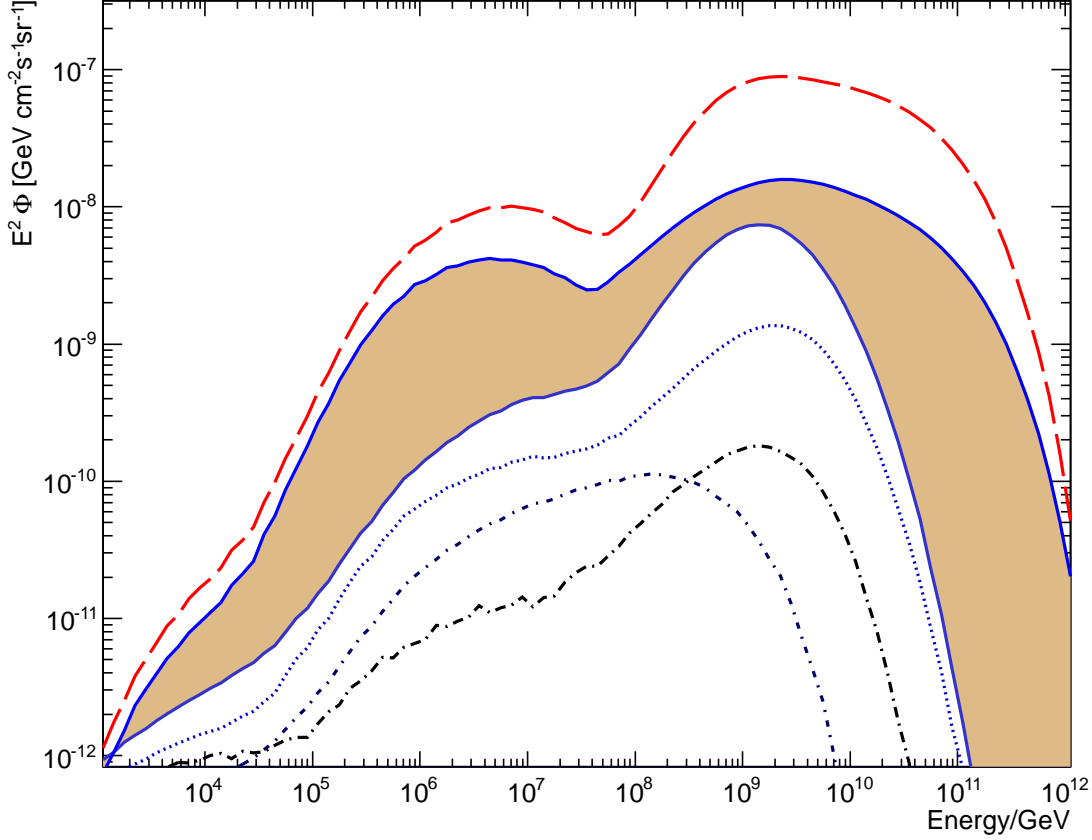
Figure 3.2: The different cosmogenic neutrino flux models considered in this work, always representing the sum of all neutrino flavours. The highest prediction presented as a red dashed line corresponds to a strong FRII source evolution model with a pure proton composition and a maximum acceleration energy $E_{p,\max} = 10^{0.5}$ ZeV. As a shaded area follows a region of realistic neutrino fluxes with a wide range of parameters. Not included in this range are uniform and FRII evolution models as well as iron rich (with low $E_{p,\max}$) and pure iron composition models. The next lower prediction also contributing to realistic models and presented as blue dotted line is the lowest prediction from above but including a uniform source emissivity evolution model. As the lowest predictions follow both with uniform evolution case the low $E_{p,\max}$, iron rich model and the pure iron ($E_{p,\max} = 100$ EeV) model presented as blue and black dashed dotted lines, respectively. How the cosmogenic neutrino flux especially is influenced by the different models and parameters is described in the text.

3.2.1 Source Emissivity Evolution

As mentioned in chapter 2, there are not many astrophysical objects which qualify for the production of ultra high energy cosmic rays, namely AGN and GRBs. Figure 3.3 shows evolution models for possible sources assumed to be origin of ultra high energy cosmic rays. There are considered two evolution models for GRBs and one for AGN as mentioned in chapter 2, more precisely Fanaroff-Riley type II (FRII) which is a special kind of AGN. Besides them a uniform evolution model and two different star formation rate (SFR) evolution models are plotted, as star formation regions generally are a tracer for matter density in the universe and therefore a tracer for possible sources of ultra high energy cosmic rays. Figure 3.4 shows the effects of these emissivity evolution models for the cosmogenic neutrino flux.
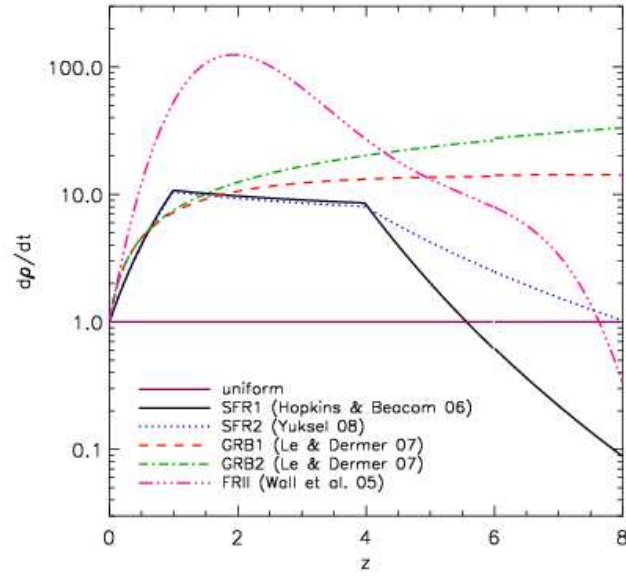
Figure 3.3: Different models of the source emissivity evolution with redshift z. Shown are two SFR type evolutions (black solid and blue dashed), two GRB type evolutions (red dashed and green dashed dotted), a FRII and a uniform evolution model. They are all normalized to unity at $z = 0$. It can be seen that the SFR and GRB models are similar up to $z = 4$ in contrast to the latter two models. See Figure 3.4 for their effect on the cosmogenic neutrino flux. Figure taken from [7].
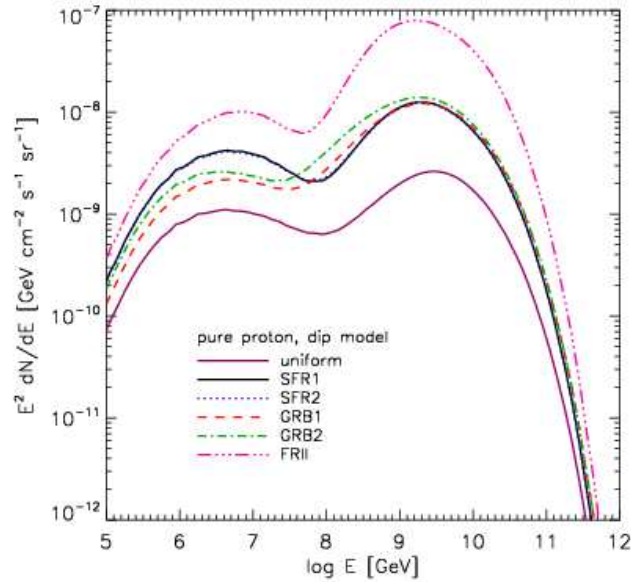
Figure 3.4: Impacts of the different source evolution models on the cosmogenic neutrino flux for a pure proton composition, dip transition model. It can be seen that the fluxes for the SFR and GRB models are very similar, while the strong FRII source evolution and the uniform evolution lead to a global increase or decrease of the spectrum, respectively, demonstrating that the difference in the evolution models above $z \approx 4$ has little effect on the neutrino production. Figure taken from [7].

Figure 3.5: Effect of various transition models on the cosmogenic neutrino flux for the case of a SFR type source evolution. The pure proton dip model with an injection spectrum of $\gamma_{\text{inj}} = 2.5$ (black solid line), together with the galactic mix model with an injection index of 2.1 and a transition slightly below the ankle (pink dotted line) and a pu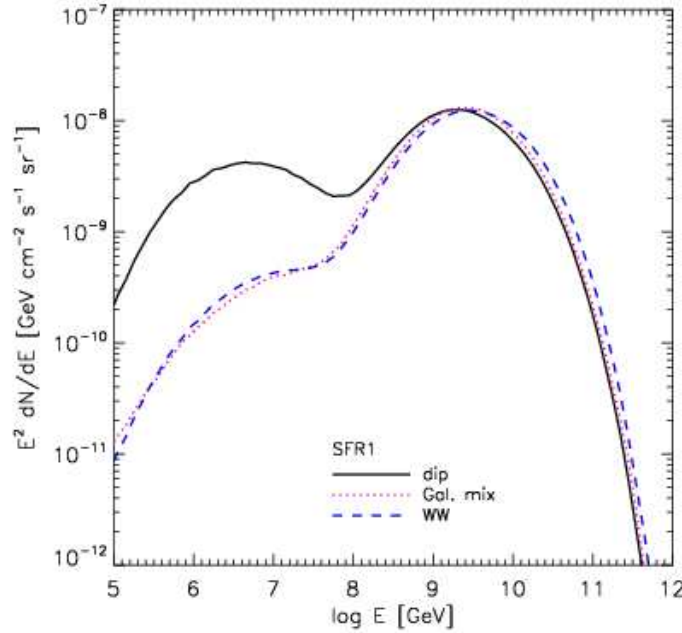re proton 'WW model' with $E_{\text{T}} > 10\,\text{EeV}$ and $\gamma_{\text{inj}} = 2.1$ is shown. The flux is normalized at 10 EeV. The lower presence of cosmic rays at lower energies for the galactic mix and the WW model compared to the dip model results in the big difference below 100 PeV. At highest energies the high injection index of the dip model is compensated on the one hand by the heavier composition of the galactic model and on the other hand by the fact that there are in general less extragalactic cosmic rays in the WW model so that the fluxes are similar of all three models. Figure taken from [7].

3.2.2   Transition Model

Generally the 'ankle' in the cosmic ray spectrum is associated with the galactic to extragalactic transition of the components of the cosmic rays. Yet there is little known about how exactly this transition looks like. Important parameters for the transition are in particular the spectral index of the injection spectrum of the cosmic rays γ_{inj}, the injected particle composition and the energy E_{T} where the extragalactic contribution begins to predominate over the galactic one. Since the cosmic ray spectrum at the observer that follows from these parameters has to fit the cosmic ray data that has been measured so far, the injection index and the injected particle composition are not independent from each other, as they both influence the shape of the cosmic ray spectrum after propagation. Figure 3.5 shows the effect of three different transition models on the cosmogenic neutrino flux spectrum. The so-called 'WW model' assumes an injection index of $2.0 \lesssim \gamma_{\text{inj}} \lesssim 2.4$ with a pure proton composition and a transition energy $E_{\text{T}} \gtrsim 10\,\text{EeV}$. Additionally, a 'galactic mix' model is considered which assumes an injection composition similar to that of low energy galactic cosmic rays. For this model the injection index γ_{inj} is around $2.2 - 2.3$ and the transition range begins at $E_{\text{T}} \approx 1\,\text{EeV}$ and ends at the ankle ($E_{\text{T}} \approx 3\,\text{EeV}$). Furthermore, a so-called 'dip model' exists where the transition occurs already at the so-called second knee in the cosmic ray spectrum in an energy region of $32\,\text{PeV} \lesssim E_{\text{T}} \lesssim 320\,\text{PeV}$. This requires a steeper injection spectrum of $2.3 \lesssim \gamma_{\text{inj}} \lesssim 2.7$ and the abundance of heavy nuclei may not exceed 10-15 %. How specific parameter values for these models effect the cosmogenic neutrino spectrum is shown in Figure 3.5. For further detail on different transition models see [11].
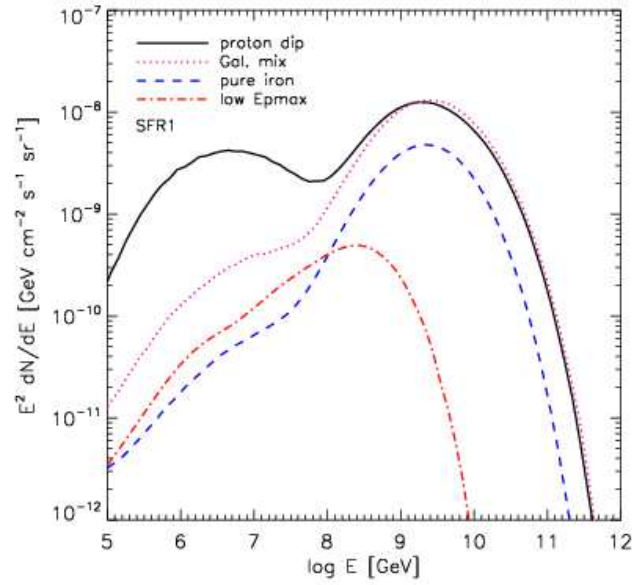
Figure 3.6: Impacts of different chemical compositions of the cosmic rays at injection for a SFR source evolution. Presented are the results for a pure proton dip transition model (black solid line), a proton dominated galactic type mixed composition (pink dotted line), a pure iron composition (blue dashed line) and a low E_p, max iron rich model (red dashed dotted line). The low maximum acceleration energy in addition to an iron rich composition leads to a drastic reduction of the whole cosmogenic neutrino flux. Apart from that, the CMB bump in the spectrum is only little affected by different compositions while the differences in the low energy bump are caused by the respective injection index needed to fit the observed cosmic ray spectrum. Namely, for a lighter composition a much higher injection index is required, resulting in more cosmic rays being present at lower energies and thus more neutrinos will be produced. Figure taken from [7].

3.2.3 Chemical Composition

The cosmogenic neutrino fluxes obtained from different chemical compositions of the cosmic rays at the acceleration site is shown in Figure 3.6. Four models are considered: a pure proton composition, a mixed composition based on lower energy galactic abundances, a pure iron composition and a mixed composition containing 30 % iron. It is assumed that for a maximum proton energy of $E_{p,\mathrm{max}}$ a nucleus of charge number Z has the maximum energy $E_{Z,\mathrm{max}} = Z \cdot E_{p,\mathrm{max}}$. For the last of the four models, to fit the observed cosmic ray data, a rather low maximum acceleration energy of $E_{p,\mathrm{max}} = 10\,\mathrm{EeV}$ is required, which leads to a drastic reduction of the whole neutrino spectrum. Latest results on the chemical composition of highest energy cosmic rays can be found in [13, 14]. Effects of higher maximum acceleration energies follow in the next section.

3.2.4 Maximum Acceleration Energy

Figure 3.7 presents the effect of different maximum acceleration energies $E_{p,\mathrm{max}}$ on the cosmogenic neutrino flux for the assumption of a pure proton dip transition model and an SFR1 type source evolution. The maximum energy particles contributing to the cosmic rays can reach, depends on the source and the physical parameters of its acceleration mechanism. While there is less known about the main sources of the highest energy particles in cosmic rays, even less can be said about what specific process leads to these high energies. Consequently, one tries to shed light on these question with high energy astroparticle experiments like KM3NeT.
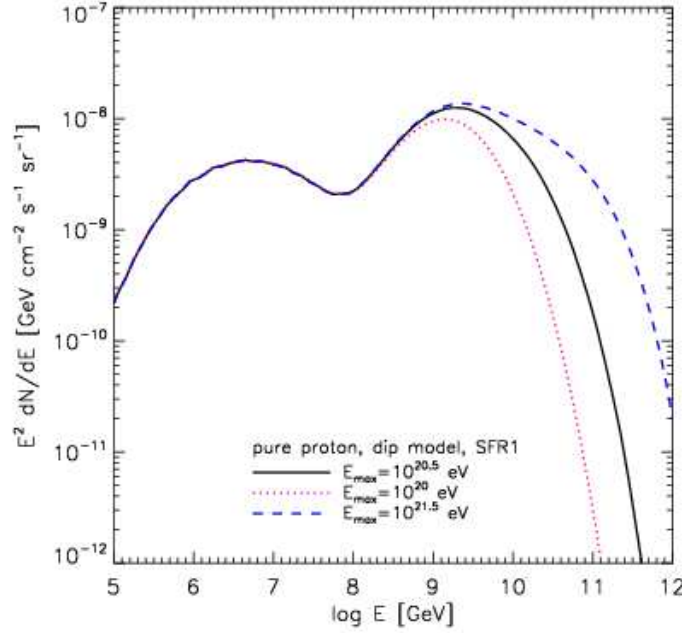
Figure 3.7: Impacts of different maximum acceleration energies on the cosmogenic neutrino flux assuming a SFR type source evolution with a pure proton dip model. Effects of $E_{p,\mathrm{max}} = 10^2$, $10^{2.5}$ and 10^3 EeV are presented as a pink dotted, black solid and blue dashed linke, respectively. While at highest energies the spectrum changes drastically according to the respective energy, the peak of the high energy bump is only mildly effected. Figure taken from [7].

3.3   Atmospheric Neutrino Flux

Atmospheric neutrinos form a major, irreducible background for experiments like KM3NeT in the search for cosmic neutrinos. They are produced when cosmic rays interact in the atmosphere following equations (3.3) and (3.1) as a by-product of extensive air showers. The contribution according to equation (3.2) is less important as most muons reach the detector before decaying. Thus the electron neutrino component is strongly suppressed. In addition, the atmospheric neutrino flux spectrum is much steeper than the primary cosmic ray flux due to the fact that with rising energy, the probability grows that the charged mesons interact with the surrounding matter before decaying resulting in a spectral index of $\gamma \approx 3.7$. Many different theoretical models for this so-called conventional atmospheric neutrino flux exist (see for example [20–24]) based on simulations of the interaction of the cosmic rays with the matter in the atmosphere.

With increasing energy of the cosmic rays, the production of particles with charm content becomes more and more important. These very short lived particles decay before interacting with the surrounding matter thus on the one hand making the atmospheric neutrino spectrum less steep and on the other hand causing the electron neutrino component to rise (see Figure 3.9). This component of the atmospheric neutrino flux is called the prompt neutrino flux. Because of the lack of information on charm production at these high energies, predictions of the prompt neutrino flux [25–28] vary strongly, resulting in an uncertainty larger than one order of magnitude. These predictions can be categorized into three types of models according to the underlying physics regarding the charm production:
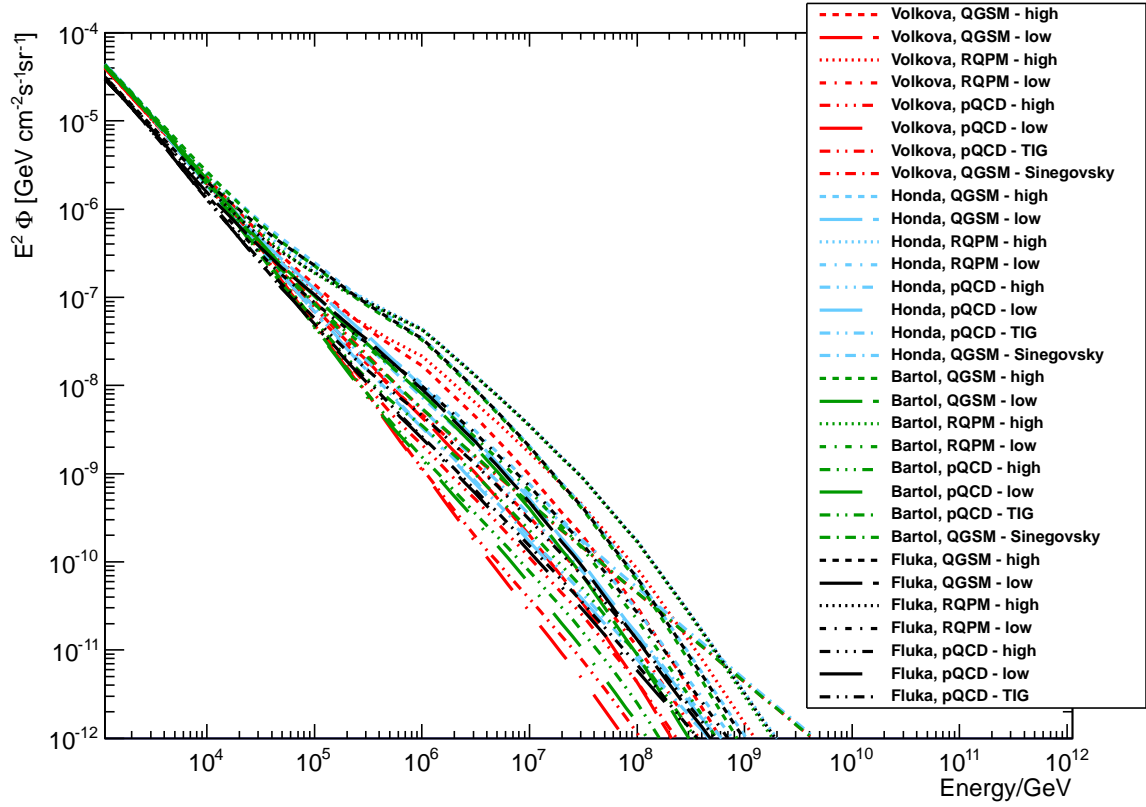
Figure 3.8: The different models of the atmospheric neutrino fluxes combined with different models of the prompt neutrino flux. In the energy range from $10^4 - 10^6$ GeV, depending on the model, the prompt component begins to dominate which can be seen as an explicit hardening of the spectrum. This Figure also illustrates the big differences of the various prompt models forming a large range of possible atmospheric fluxes.

- Quark Gluon String Model (QGSM), a semiempirical approach based on non-perturbative quantum chromodynamics (QCD) calculations.

- Recombination Quark Parton Model (RQPM), a phenomenological model also based on non-perturbative QCD calculations.

- A model based on perturbative QCD (pQCD) in which the charm production is explicitly evaluated.

These models and their consequences for the prompt neutrino flux are discussed in [25].

Figure 3.8 shows a plot of different combination of models for the conventional and for the prompt atmospheric neutrino flux. The prompt flux begins to dominate somewhere between $10^4 - 10^6$ GeV depending on the model.

The predictions for the conventional flux considered in this work are the Volkova [20], Bartol [23], Honda [29] and an updated FLUKA [21] model taken from the ANTARES software library.[1] This library also provides nine distinct data tables for the prompt neutrino flux which are taken from [25–27], seven of which are used.[2] In particular these are the TIG model from [27], which is a pQCD approach, and

---

[1]This software library also contains the data tables of three additional models [22, 24, 30], however, because of unsolvable problems with the ANTARES software library, only the four above-mentioned models could be used.

[2]For similar reasons as for the conventional models, not all could be used.
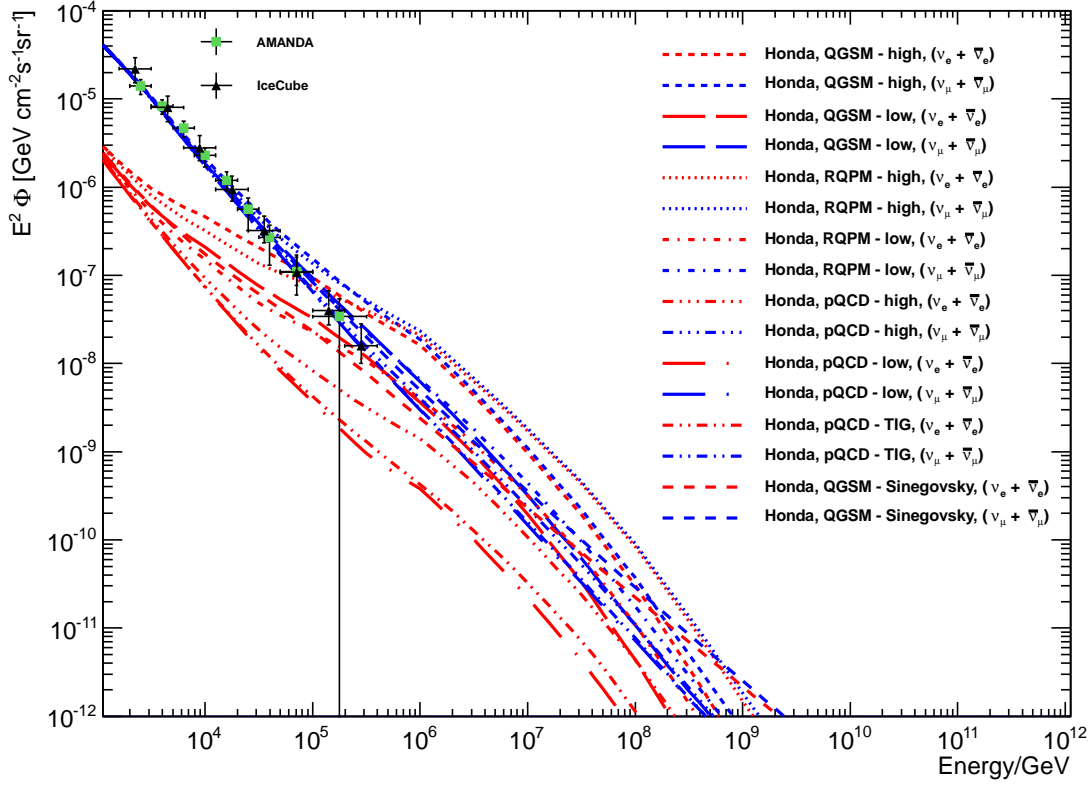
Figure 3.9: Comparison of the atmospheric electron and muon neutrino flux for the conventional model from Honda. The onset of the prompt flux can be seen as a rise compared with the conventional flux. Because of the low conventional electron neutrino flux the rise of that sort happens at lower energies. For the high QGSM and RQPM predictions the electron and muon neutrino contributions almost become equal while for the low pQCD and the TIG model the electron neutrino fraction always stays well below the muon neutrino one. Also included in this picture are measurements of the atmospheric muon neutrino flux made by AMANDA and IceCube that somewhat constrain the range of possible prompt fluxes.

the ones following from the charm production approaches mentioned above (QGSM, RQPM, pQCD). For each of those the lowest and the highest prediction is considered. Additionally a parametrization by Sinegovsky [28] for QGSM is used. In total this leads to 32 different combination of models considered here which define a wide range of possible atmospheric neutrino flux spectra. The uncertainties can be quantified by 20-25 % for the conventional flux and are larger than one order of magnitude for the prompt neutrino flux.

Figure 3.9 shows separately the atmospheric muon and electron neutrino flux. It demonstrates the suppression of the electron neutrino component at lower energies and its rise as the prompt component sets in. For prompt models favouring charm production the ν_e/ν_μ-ratio for high energies eventually becomes almost equal to one. Also shown in this plot are measurements of the atmospheric muon neutrino flux made by AMANDA [31] and IceCube [32]. These observations fit the conventional models very well and already seem to exclude the highest predictions for the prompt neutrino flux.

Consequently, as the conventional atmospheric neutrino flux up to energies of 10^4 GeV is well understood it can be used for the calibration of the neutrino detectors like KM3NeT and to assess its performance. Further observations of the prompt component can help understanding hadronic interactions at high energies.

Chapter 4

Neutrino Interaction

4.1 Kinematics and Neutrino Cross Section

Neutrinos interact through gravitation and the weak force. Due to their low mass, the only relevant interaction type for their detection is the weak interaction. In the energy ranges considered here, the predominant interaction process is the deep-inelastic scattering (DIS) between the neutrino and a nucleon N. This process is illustrated in Figure 4.1. Lepton-nucleon DIS is generally described by several
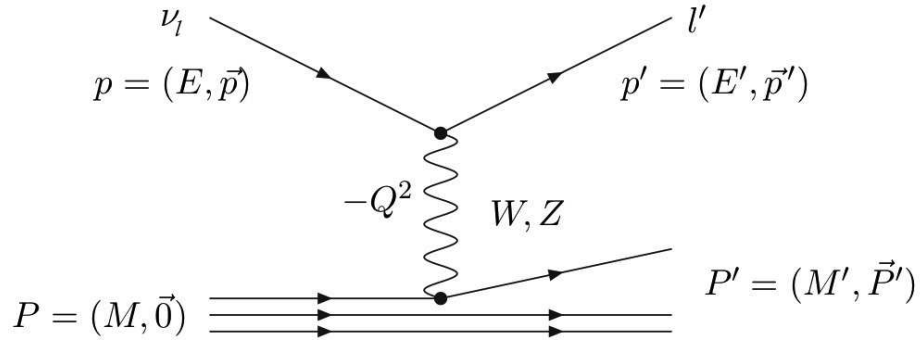
Figure 4.1: Kinematic situation for the deep-inelastic neutrino nucleon scattering. See also [33] where the figure is taken from. ν_l represents an incident neutrino of flavour l, while l' stands for the outgoing lepton. W and Z are the mediating bosons respectively. See text for more.

invariant[1] quantities, among them the Bjorken x and y variables and Q^2. Q^2 is defined as the negative squared of the four-momentum transfer $q = p - p'$ between the incoming lepton with four-momentum p and outgoing lepton with four-momentum p':

$$Q^2 := -q^2 = -(p - p')^2. \tag{4.1}$$

In the parton model, x describes the fraction of the nucleon's momentum carried by the struck quark. It is given by

$$x := \frac{Q^2}{2M\nu}. \tag{4.2}$$

where M is the mass of the nucleon. The invariant quantity $\nu = q \cdot P/M = E - E'$ is the neutrino's energy loss in the nucleon rest frame, which here is equivalent to the laboratory system. P is the initial

---

[1]Invariant under Lorentz transformation.

four-momentum of the nucleon while E and E' are the initial and final lepton energies in the nucleon rest frame. y is the fraction of the lepton's energy lost in the nucleon rest frame and plays an important role in neutrino detection (see also section 4.3). It is often referred to as the inelasticity:

$$y := \frac{q \cdot P}{p \cdot P} = \frac{\nu}{E}. \tag{4.3}$$

One distinguishes two kinds of weak interaction processes: charged current (CC) interactions mediated by a charged W boson and neutral current (NC) interactions mediated by the neutral Z boson. For the CC interactions, where a charged lepton is produced,

$$
\begin{aligned}
\overset{(-)}{\nu}_e + N &\to e^{\mp} + X, \\
\overset{(-)}{\nu}_\mu + N &\to \mu^{\mp} + X, \\
\overset{(-)}{\nu}_\tau + N &\to \tau^{\mp} + X,
\end{aligned} \tag{4.4}
$$

the νN total cross section is given by [34]

$$\sigma_{\text{CC}}(E_\nu) = \frac{2 G_F^2 M_N E_\nu}{\pi} \int\limits_0^1 \int\limits_0^1 \mathrm{d}y \, \mathrm{d}x \left(\frac{M_W^2}{Q^2 + M_W^2} \right)^2 \left[q_{\text{CC}} + (1-y)^2 \bar{q}_{\text{CC}} \right]. \tag{4.5}$$

For the NC interactions, where the neutrino remains in its initial state and only the hadronic cascade X is produced,

$$\overset{(-)}{\nu}_l + N \to \overset{(-)}{\nu}_l + X, \tag{4.6}$$

the νN total cross section is given by

$$\sigma_{\text{NC}}(E_\nu) = \frac{2 G_F^2 M_N E_\nu}{\pi} \int\limits_0^1 \int\limits_0^1 \mathrm{d}y \, \mathrm{d}x \left(\frac{M_Z^2}{Q^2 + M_Z^2} \right)^2 \left[q_{\text{NC}} + (1-y)^2 \bar{q}_{\text{NC}} \right]. \tag{4.7}$$

In these equations $G_F = 1.17 \cdot 10^{-5} \, \text{GeV}^{-2}$ is the Fermi coupling constant, M_N is the mass of the nucleon (0.9383 GeV for the proton, 0.9396 GeV for the neutron), $M_W = 80.4$ GeV and $M_Z = 91.2$ GeV are the masses of the mediating bosons, respectively, E_ν is the incident neutrino energy, x and y are the Bjorken variables and Q^2 is the negative four-momentum transfer squared. q_{CC}, $\bar{q}_{\text{CC}}$, q_{NC} and $\bar{q}_{\text{NC}}$ are the target parton distribution functions (PDFs) for the nucleon of the respective reaction which generally depend on x and Q^2. For the $\bar{\nu} N$ cross sections, the equations are the same with each distribution function replaced with the corresponding antiparticle distribution function and vice versa. For more details on the PDFs see [34] and references therein. The high energy νN cross section is shown in Figure 4.2. There is a rising uncertainty in the ultra high energy cross section. This is due to the fact that the PDFs are not known at these high energies and thus have to be extrapolated.

4.2 The Glashow Resonance

Generally for neutrino interactions, other processes besides deep-inelastic neutrino nucleon scattering can be neglected. However, in the energy range of a few PeV, electron antineutrinos may interact res-
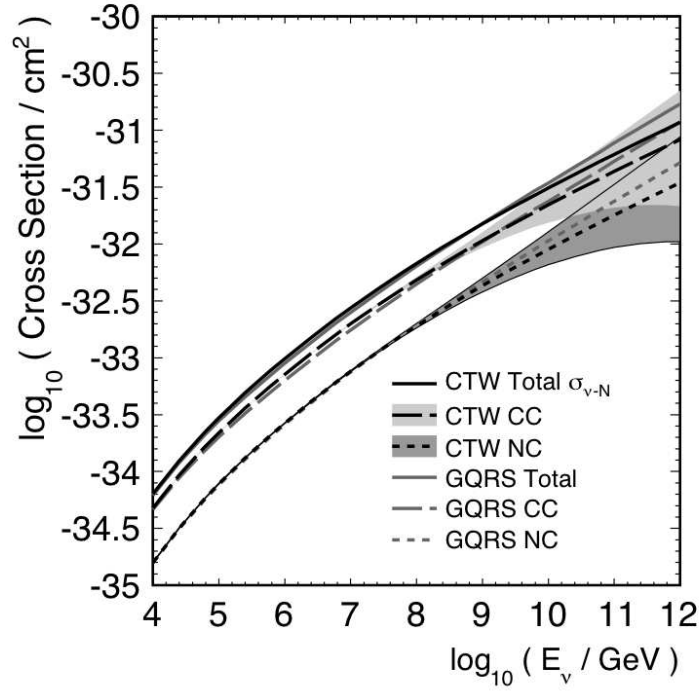
Figure 4.2: The high energy neutrino cross section for CC and NC νN DIS reactions with isoscalar targets as calculated by Connolly et al. [34], where the Figure is taken from, compared with earlier calculations (GQRS) [35]. Uncertainties due to unknown PDFs are indicated as shaded bands. The NC cross section uncertainties additionally are bounded by thin black lines.

onantly with electrons, thus generating a W^- Boson which thereupon decays into leptons or a quark-antiquark pair which produces a hadronic shower:

$$\bar{\nu}_e + e^- \rightarrow W^- \rightarrow \begin{cases} \bar{\nu}_e + e^- \\ \bar{\nu}_\mu + \mu^- \\ \bar{\nu}_\tau + \tau^- \\ (q + \bar{q}) \rightarrow X \end{cases} \tag{4.8}$$

This resonant W^- production is also called the Glashow resonance, whose main features will be described shortly in the following. It will become clear that this resonance plays an important role for high energy neutrino experiments.

The differential cross section for the $\bar{\nu}_e e^- \rightarrow \bar{\nu}_\mu \mu^-$ reaction is given in [36] as:

$$\frac{\mathrm{d}\sigma(\bar{\nu}_e e^- \rightarrow \bar{\nu}_\mu \mu^-)}{\mathrm{d}y} = \frac{2G_F^2 m_e E_\nu}{\pi} \cdot \frac{\left(1 - \frac{m_\mu^2 - m_e^2}{2m_e E_\nu}\right)^2}{\left(1 - \frac{2m_e E_\nu}{M_W^2}\right)^2 + \frac{\Gamma_W^2}{M_W^2}} \cdot (1 - y)^2. \tag{4.9}$$

The resonance cross sections for the three reactions with leptonic decay products are approximately the same. The cross section for the hadronic mode is given by:

$$\frac{\mathrm{d}\sigma(\bar{\nu}_e e^- \rightarrow X)}{\mathrm{d}y} = \frac{\mathrm{d}\sigma(\bar{\nu}_e e^- \rightarrow \bar{\nu}_\mu \mu^-)}{\mathrm{d}y} \cdot \frac{\Gamma(W \rightarrow q\bar{q})}{\Gamma(W \rightarrow \nu_\mu \mu)} \tag{4.10}$$

constant	meaning	value	unit
G_F	Fermi coupling constant	$1.1664 \cdot 10^{-5}$	GeV^{-2}
m_e	electron mass	$0.51100 \cdot 10^{-3}$	GeV
m_μ	muon mass	$105.66 \cdot 10^{-3}$	GeV
M_W	W boson mass	80.399	GeV
Γ_W	W boson width	2.085	GeV
$(\hbar c)^2$	conversion constant	$0.38938 \cdot 10^{-27}$	$\text{cm}^2\,\text{GeV}^2$
$\dfrac{\Gamma(W \to X)}{\Gamma(W \to \nu_\mu \mu)}$	ratio of partial widths	6.3955	

Table 4.1: Values of the constants used in the formulas in natural units, i.e. $\hbar = c = 1$. The values are taken from the Particle Data Group [37].

where $\Gamma(W \to q\bar{q})$ and $\Gamma(W \to \nu_\mu \mu)$ are the partial widths for a W boson decaying into a quark-antiquark pair or into a muon neutrino and muon. Equation (4.9) can be integrated[2] to get the total cross section:

$$\sigma(\bar{\nu}_e e^- \to \bar{\nu}_\mu \mu^-) = \frac{2G_F^2 m_e E_\nu}{3\pi} \cdot \frac{\left(1 - \frac{m_\mu^2 - m_e^2}{2m_e E_\nu}\right)^2}{\left(1 - \frac{2m_e E_\nu}{M_W^2}\right)^2 + \frac{\Gamma_W^2}{M_W^2}}. \tag{4.11}$$

The constants appearing in these and following formulas are summarized in Table 4.1, while like above E_ν is the neutrino energy and y is now the fraction of the energy transferred to the recoiling charged lepton. Figure 4.3 shows the Glashow resonance cross section $\sigma(\bar{\nu}_e e^- \to \text{anything})$ together with the DIS neutrino nucleon cross sections used in this work.

The resonance peak is reached when the denominator becomes minimal. Therefore the resonance energy is given by the following expression (which can also be obtained by evaluating the square of the neutrino-electron four momentum and set it equal to M_W^2):

$$E_\nu^{\text{res}} = \frac{M_W^2}{2m_e} = 6.325\,\text{PeV}. \tag{4.12}$$

Thus, as the numerator in the right fraction of equation (4.11) is approximately equal to unity at E_ν^{res}, the peak cross section is given by:

$$\sigma^{\text{res}}(\bar{\nu}_e e^- \to \bar{\nu}_\mu \mu^-) = \left(\frac{G_F M_W^2}{\sqrt{3\pi}\,\Gamma_W}\right)^2 = 5.402 \cdot 10^{-32}\,\text{cm}^2. \tag{4.13}$$

Table 4.2 summarizes the values for the cross section of different reactions at E_ν^{res}. The Glashow resonance cross section exceeds the deep-inelastic neutrino nucleon scattering cross section by a factor of approximately 240 which results in a rise of expected neutrino event rates by a factor of up to 20 in the energy region around E_ν^{res} considering all neutrino flavours and assuming the same flux for each neutrino flavour[3]. This visibly will affect the energy integrated event rates in an experiment like KM3NeT (see chapter 7).

---

[2]Evaluating the integral yields $\int_0^1 (1 - y)^2 \mathrm{d}y = \frac{1}{3}$.

[3]The factor is derived by dividing 240 by 6 as all neutrino types are considered, and again by 2 as the number of electrons is roughly half the number of nucleons considering standard interaction media.
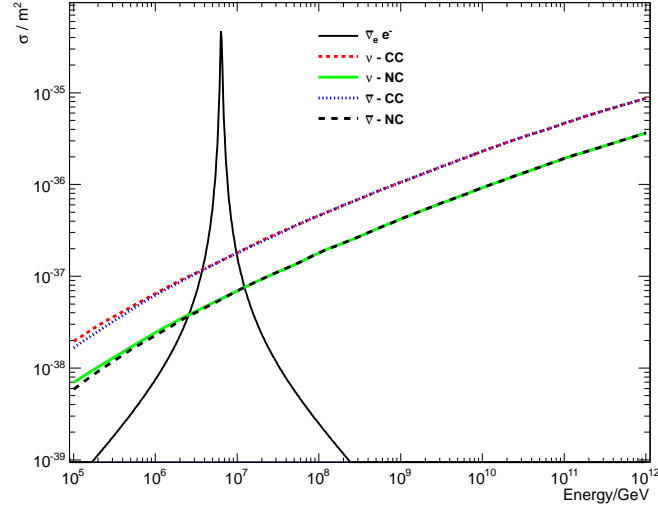
Figure 4.3: The cross sections in the very high energy regime used in this work for the calculation of the event rates (see chapter 7), which are the total $\bar{\nu}_e e^-$ cross section including all reaction channels and DIS neutrino nucleon cross section for all reaction types. The data of the deep-inelastic scattering cross section is taken from [38].

reaction			σ/cm^2
νN	$\rightarrow$	νX	$5.97 \cdot 10^{-34}$
νN	$\rightarrow$	$l^{\mp} X$	$15.5 \cdot 10^{-34}$
νN	$\rightarrow$	anything	$21.5 \cdot 10^{-34}$
$\bar{\nu}_e e^-$	$\rightarrow$	$\bar{\nu}_e e^-$	$5.40 \cdot 10^{-32}$
$\bar{\nu}_e e^-$	$\rightarrow$	$\bar{\nu}_\mu \mu^-$	$5.40 \cdot 10^{-32}$
$\bar{\nu}_e e^-$	$\rightarrow$	$\bar{\nu}_\tau \tau^-$	$5.40 \cdot 10^{-32}$
$\bar{\nu}_e e^-$	$\rightarrow$	$q\bar{q}$	$34.5 \cdot 10^{-32}$
$\bar{\nu}_e e^-$	$\rightarrow$	anything	$50.8 \cdot 10^{-32}$

Table 4.2: Summary of total neutrino cross sections at E_ν^{res}. ν in the first three reactions stands for any one kind of neutrino while $l^{\mp}$ in the second reaction represents any one kind of charged lepton corresponding to equations (4.4). The values for the Glashow resonance are calculated according to equations (4.13) and (4.10). The values for the νN cross section are interpolated according to the data from [38].

Not only because of this significant rise of event rates but also due to its special event characteristics the Glashow resonance can play an important role as Bhattacharya et al. [39] presented a way how the special event characteristics of the Glashow resonance (see also section 5.1.2) can be used to discriminate between different kinds of neutrino production channels (equations (3.3) and (3.4)).
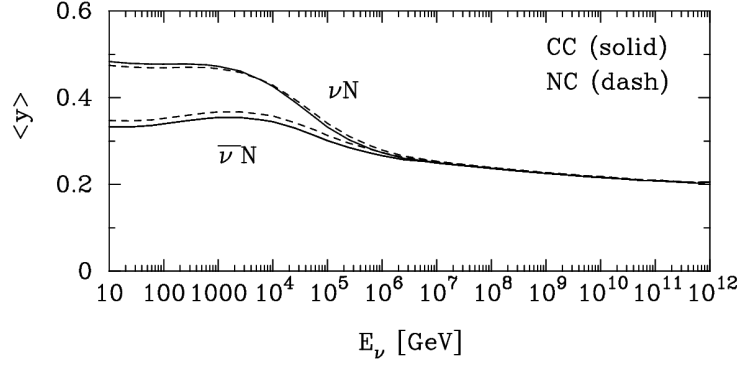
Figure 4.4: Mean inelasticity $\langle y \rangle$ as a function of the incident neutrino energy in the energy range from $10 - 10^{12}$ GeV for charged current (solid line) and neutral current (dashed line) neutrino and antineutrino nucleon interactions as calculated by Gandhi et al. [36] where the figure is taken from. For high energies the mean inelasticity approaches a value of $\langle y \rangle \lesssim 0.2$.

4.3 The Bjorken y Variable

While especially for smaller detectors and lower energy experiments muon searches have priority, i.e. detecting the muon produced in a CC interaction, cascade events, which are produced in every neutrino nucleon reaction as a hadronic shower, grow in importance with increasing detector volume and neutrino energy. The reason for this is on the one hand, that for kilometre-scale detectors the effective volume for cascade events becomes comparable to that for low energy muon detection. On the other hand, only a part of the muon energy is deposited in the detector while for contained cascade events, the total amount of light output that can be measured directly, allows the total shower energy to be inferred (see also section 5.1.2).

But to be able to make a general statement about a measured shower event, one needs to know the energy transferred from the incident neutrino to the cascade, and the corresponding energy which is consequently deposited in the detector. This is given by the Bjorken y variable also referred to as inelasticity, as it is the fraction of the neutrino energy transferred to the hadronic cascade. While the inelasticity varies statistically one can calculate the mean value $\langle y \rangle$, the distribution of which with respect to the incident neutrino energy is shown in Figure 4.4.

Connolly et al. [34] recently published parametrizations for the differential neutrino nucleon cross sections $d\sigma/dy$ in the ultra high energy regime $10^7 \leq E_\nu \leq 10^{12}$ GeV, in which the mean inelasticity does not differ significantly for all interaction types:

$$\frac{d\sigma}{dy} = \begin{cases} Y_s(C_0, C_1, C_2), & \text{for} \quad 0 < y < 10^{-3} \\ Y_h(D_0, D_1), & \text{for} \quad 10^{-3} < y < 1 \end{cases} \tag{4.14}$$

with

$$Y_s(C_0, C_1, C_2) = \frac{C_0}{(y - C_1)^{\frac{1}{C_2}}} \tag{4.15}$$

$$Y_h(D_0, D_1) = \frac{D_0}{y - D_1}, \tag{4.16}$$

where 's' and 'h' indicate the low ($y < 10^{-3}$) and high ($y > 10^{-3}$) inelasticity region, and C_0 and D_0 are normalization parameters, so that the distribution is normalized to unity. They are together with the other parameters C_1, C_2 and D_1 energy dependent. For the latter three parameters the energy dependence can also be parametrized:

	A_0	A_1	A_2	A_3
all νN	0.0	0.0941	4.72	0.456

	E_0	E_1	E_2	E_3
$\bar{\nu}N$ - CC	-0.0026	0.085	4.1	1.7
νN - CC	-0.008	0.26	3.0	1.7
$\bar{\nu}N$ - NC	-0.005	0.23	3.0	1.7
νN - NC	-0.005	0.23	3.0	1.7

	B_0	B_1	F_0	F_1	F_2
all νN	2.55	-0.0949	0.128	-0.197	21.8

Table 4.3: The constants appearing in equations (4.17) - (4.20).

$$C_1(\varepsilon) = A_0 - A_1 \cdot e^{-\frac{\varepsilon - A_2}{A_3}}, \tag{4.17}$$

$$C_2(\varepsilon) = B_0 + B_1 \cdot \varepsilon, \tag{4.18}$$

$$D_1(\varepsilon) = E_0 - E_1 \cdot e^{-\frac{\varepsilon - E_2}{E_3}}, \tag{4.19}$$

with $\varepsilon = \log_{10}(E/\text{GeV})$. In addition to that, a parametrization for the fraction of the cross section occupying the low y region exists:

$$F(\varepsilon) = F_0 \cdot \sin(F_1 \cdot (\varepsilon - F_2)). \tag{4.20}$$

The values for the constants are given in Table 4.3. These formulas are used in the following to calculate an analytical function for the distribution of the mean value of $\langle y \rangle$ for the energy region $10^7 \leq E \leq 10^{12}$ GeV. This function is used in section 6.1.2 to compare it with results of simulations of ultra high energy neutrino interactions. It should be mentioned that Connolly et al. also published a method to determine the distribution of $\langle y \rangle$ in the form of a software program, however, no analytical function for the $\langle y \rangle$-distribution was given.

Derivation of an Expression for the Mean Inelasticity

With the formulas given above the mean inelasticity $\langle y \rangle$ can be expressed as

$$\langle y \rangle = \frac{\int_0^1 y \cdot \frac{d\sigma}{dy} \, dy}{\int_0^1 \frac{d\sigma}{dy} \, dy} = \frac{\int_0^{10^{-3}} y \cdot Y_s \, dy + \int_{10^{-3}}^1 y \cdot Y_h \, dy}{\int_0^{10^{-3}} Y_s \, dy + \int_{10^{-3}}^1 Y_h \, dy}. \tag{4.21}$$

Due to the fact that the parameters C_0 and D_0 in Y_s and Y_h from equation (4.15) and (4.16) are not known, this cannot be calculated directly. So in a sense the following calculation corresponds to an elimination

of these two parameters. For a better readability the following abbreviations and definitions are made:

$$y_m := 10^{-3},$$

$$\bar{y} := \int_0^1 y \cdot \frac{d\sigma}{dy} \, dy, \qquad \bar{y}_s := \int_0^{y_m} y \cdot \frac{d\sigma}{dy} \, dy = \int_0^{y_m} y \cdot Y_s \, dy, \qquad \bar{y}_h := \int_{y_m}^1 y \cdot \frac{d\sigma}{dy} \, dy = \int_{y_m}^1 y \cdot Y_h \, dy,$$

$$\sigma := \int_0^1 \frac{d\sigma}{dy} \, dy, \qquad \sigma_s := \int_0^{y_m} \frac{d\sigma}{dy} \, dy = \int_0^{y_m} Y_s \, dy, \qquad \sigma_h := \int_{y_m}^1 \frac{d\sigma}{dy} \, dy = \int_{y_m}^1 Y_h \, dy,$$

$$\langle y \rangle_s := \frac{\bar{y}_s}{\sigma_s}, \qquad \langle y \rangle_h := \frac{\bar{y}_h}{\sigma_h}, \qquad n_s := \frac{\sigma_s}{\sigma}, \qquad n_h := \frac{\sigma_h}{\sigma}.$$

Now $\langle y \rangle$ can be written as

$$\langle y \rangle = \frac{\bar{y}}{\sigma} = \frac{\bar{y}_s + \bar{y}_h}{\sigma} = \frac{\bar{y}_s}{\sigma} + \frac{\bar{y}_h}{\sigma}$$

$$= \frac{\sigma_s}{\sigma} \cdot \frac{\bar{y}_s}{\sigma_s} + \frac{\sigma_h}{\sigma} \cdot \frac{\bar{y}_h}{\sigma_h}$$

$$= n_s \cdot \langle y \rangle_s + n_h \cdot \langle y \rangle_h,$$

where $n_s = F$ is given by equation (4.20) and it holds $n_h = 1 - n_s$. The unknown parameters C_0 and D_0 in $\langle y \rangle_s$ and $\langle y \rangle_h$, respectively, cancel out such that the latter two quantities can be calculated:

$$\langle y \rangle_s = \frac{\displaystyle\int_0^{y_m} y \cdot Y_s \, dy}{\displaystyle\int_0^{y_m} Y_s \, dy} = \frac{\displaystyle\int_0^{y_m} y \cdot (y - C_1)^{-\frac{1}{C_2}} \, dy}{\displaystyle\int_0^{y_m} (y - C_1)^{-\frac{1}{C_2}} \, dy} \tag{4.22}$$

$$\langle y \rangle_h = \frac{\displaystyle\int_{y_m}^1 y \cdot Y_h \, dy}{\displaystyle\int_{y_m}^1 Y_h \, dy} = \frac{\displaystyle\int_{y_m}^1 y \cdot (y - D_1)^{-1} \, dy}{\displaystyle\int_{y_m}^1 (y - D_1)^{-1} \, dy} \tag{4.23}$$

Evaluation of the integrals yields

$$\langle y \rangle_s = \frac{C_2 - 1}{2C_2 - 1} \cdot \frac{(y_m - C_1)^{2 - \frac{1}{C_2}} - (-C_1)^{2 - \frac{1}{C_2}}}{(y_m - C_1)^{1 - \frac{1}{C_2}} - (-C_1)^{1 - \frac{1}{C_2}}} + C_1 \tag{4.24}$$

$$\langle y \rangle_h = \frac{1 - y_m}{\ln\left(\frac{1 - D_1}{y_m - D_1}\right)} + D_1, \tag{4.25}$$
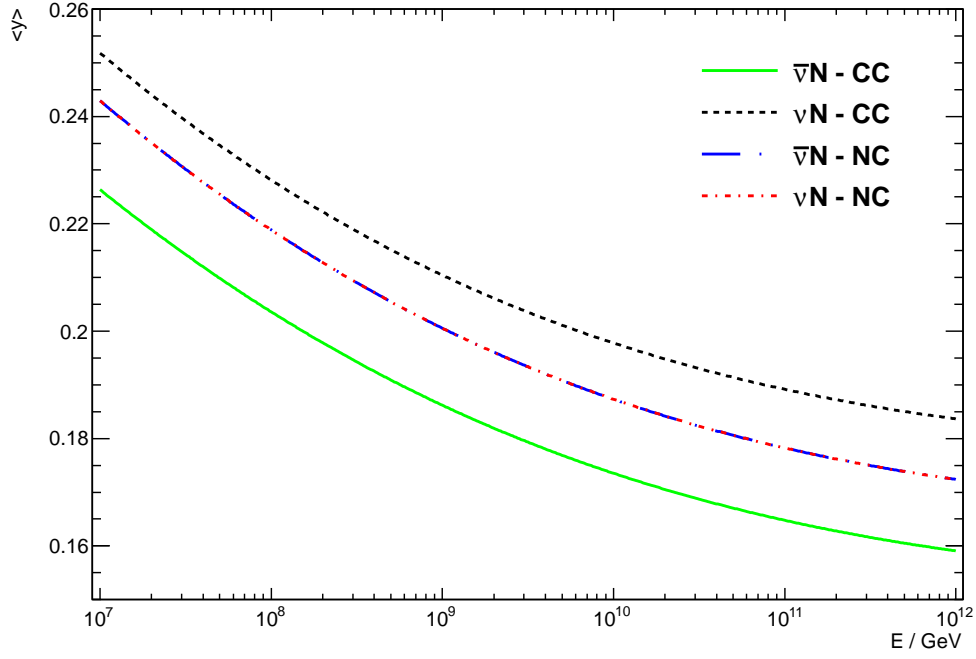
Figure 4.5: The energy dependence of the mean inelasticity as given by equation (4.26) for νN and $\bar{\nu} N$ CC and NC reactions.

so that the final expression for $\langle y \rangle$ is given by:

$$\langle y \rangle = F \cdot \left(\frac{C_2 - 1}{2C_2 - 1} \cdot \frac{(y_{\mathrm{m}} - C_1)^{2 - \frac{1}{C_2}} - (-C_1)^{2 - \frac{1}{C_2}}}{(y_{\mathrm{m}} - C_1)^{1 - \frac{1}{C_2}} - (-C_1)^{1 - \frac{1}{C_2}}} + C_1 \right) + (1 - F) \cdot \left(\frac{1 - y_{\mathrm{m}}}{\ln\left(\frac{1 - D_1}{y_{\mathrm{m}} - D_1}\right)} + D_1 \right), \qquad (4.26)$$

where, as a reminder, the parameters C_1, C_2, D_1 and F are energy-dependent and given by equations (4.17) to (4.20). This distribution is plotted in Figure 4.5 for $7 < \varepsilon < 12$ and will be used in section 6.1.2 for comparison with simulation results of high energy neutrino interaction.

Chapter 5

Mediterranean Deep-Sea Neutrino Telescopes

In this chapter, an overview is given of ANTARES, as the first working deep-sea neutrino telescope, and the KM3NeT-Project, the successor of ANTARES and in the scope of which this study is done. This overview is preceded by a brief description of the physics behind under water neutrino detection.

5.1 Under Water Neutrino Detection

5.1.1 Detection Principle

As seen in the previous chapter, high energy neutrino interactions produce a charged lepton and/or hadronic showers that exhibit charged secondary particles . If charged particles move faster than the speed of light in the surrounding medium they emit Cherenkov light. This light is emitted under a characteristic angle θ_C with respect to the particle track:

$$\cos \theta_C = \frac{1}{\beta \cdot n} \tag{5.1}$$

where $\beta = v/c$ is the velocity of the particle relative to the speed of light c, and n is the refractive index of the surrounding medium which depends on the photon wavelength. For characteristic values of $n = 1.34$ and $\beta = 1$ the Cherenkov angle is approximately $42°$. A schematic comparison of light emission from a muon and a shower is illustrated in Figure 5.1. This characteristic emission allows the reconstruction of the direction of the interaction products. Due to the fact that for sufficiently high energies, the secondary
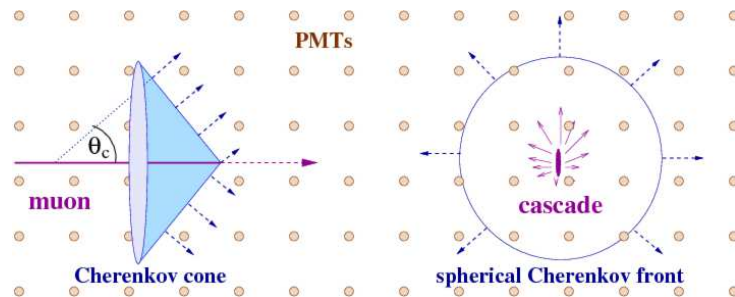

Figure 5.1: Schematic Cherenkov light emission from a muon (left) and a shower (right). The emission from the muon generates a light cone while the Cherenkov light from a shower is emitted in the full solid angle peaked at the Cherenkov angle with respect to the shower axis. The light is measured with photomultiplier tubes (PMTs), which are indicated as small circles. Figure taken from [40].

λ/nm	L_a/m	L_s/m
290	0.0	16.6
310	11.9	20.2
330	16.4	23.8
350	20.6	27.6
375	29.5	32.5
412	48.5	40.2
440	67.5	46.2
475	59.0	53.9
488	55.1	56.8
510	26.1	61.8
532	19.9	66.8
555	14.7	72.1
650	2.8	94.2
676	2.3	100.3
715	1.0	109.4
720	0.0	109.4

Table 5.1: Absorption length L_a and scattering length L_s in water as a function of the wavelength λ as used in KM3NeT. The numbers are taken from an internal KM3NeT document [41].

particles follow the initial neutrino direction with only a small deviation, the neutrino direction can be reconstructed. The energy loss per path length, a particle with charge $z e$ sustains due to the Cherenkov effect is given by

$$-\left(\frac{\mathrm{d}E}{\mathrm{d}x}\right)_C = \frac{2\pi z^2 \alpha h}{c} \int\limits_{\beta \cdot n(\nu) \geq 1} \nu \left(1 - \frac{1}{\beta^2 \cdot n^2(\nu)}\right) \mathrm{d}\nu. \qquad (5.2)$$

Here α is the fine structure constant, h the Planck constant and ν the frequency of the Cherenkov light. From this follows that a single charged particle emits almost 400 Cherenkov photons per cm in a wavelength region of 300 nm $\leq \lambda \leq$ 700 nm, the region where water is transparent to a good approximation (see also Table 5.1). This in principle allows the energy reconstruction of secondaries and therefore an estimation of the neutrino energy.

However, to successfully reconstruct the direction and energy information one not only requires efficient detection elements but one also needs to know the details of the propagation of light in water. Two main effects affect the photon propagation: absorption and scattering. The numbers N_a and N_s of unscattered or unabsorbed photons, respectively, decreases exponentially as a function of the photon path length d

$$N_a = N_0 \cdot \mathrm{e}^{-d/L_a}, \qquad N_s = N_0 \cdot \mathrm{e}^{-d/L_s}, \qquad (5.3)$$

with L_a and L_s denoting the absorption and scattering lengths, respectively. These two characteristic quantities are measured with artificial light sources as is the scattering function $\chi(\theta, \lambda)$, which describes the fraction of photons with wavelength λ scattered under an angle θ. Table 5.1 shows values for the absorption and scattering length in the transparency window of water.

As absorption just reduces the total amount of photons measured, scattering effectively delays the propagation of photons between their origin and the point of detection and therefore deteriorates time

information [40]. Consequently both effects constrain a viable event reconstruction as a high amount of photons clearly is useful for both the energy and direction reconstruction and a precise time information is important for the direction reconstruction.

5.1.2 Event signatures

Due to the fact that high energy neutrino interactions, depending on the neutrino flavour and reaction type, yield many different particles as reaction products, different neutrino events will differ in the information they leave in the detector. Generally, neutrino event features can be categorized into cascade-like and track-like signatures. These can be distinguished when looking at the Cherenkov light pattern they generate (see also Figure 5.1).

Track-like events are produced by high energy muons and ultra high energy taus[1] as they travel large distances before decaying. They produce a Cherenkov light cone, the measurement of which allows the reconstruction of the particle track, when it crosses the detector and therefore provides a good directional resolution. Because of the long range, especially of muons, it is possible to measure an event even if its origin is far outside the instrumented volume. However, the energy estimation of the corresponding primary event is then strongly handicapped as the measured energy provides only a lower limit for the primary muon energy.

Cascade-like events result from electromagnetic and hadronic showers. The energy of most involved particles is deposited in a relatively small volume with a length of several metres and a diameter of a few centimetres. Any charged particles produced in the shower will generate Cherenkov light if their energy is above the Cherenkov threshold. As their directions differ from one another, Cherenkov photons are emitted in every direction with a strong peak at the Cherenkov angle (measured from the incident neutrino direction). This makes the direction reconstruction more difficult. Because of the relatively small spread of a shower compared with the spacing of the detector elements, these events will look approximately point-like in the detector. Due to light absorption in water, the event has to be at least in the vicinity of the instrumented volume, in order to be detected. In this case, when the neutrino interaction vertex lies inside the detector, one speaks of a 'contained event'.

With that information, these event signatures can now be assigned to the different interaction types and channels (equations (4.4), (4.6) and (4.8)). In NC events, the only signature produced is a hadronic cascade, where the unmeasurable energy fraction $1 - y$ is carried away by the outgoing neutrino. In an electron neutrino CC event, an electromagnetic cascade is produced in addition to the hadronic cascade. Thus, the total neutrino energy is deposited in the detector. But as there is no possibility to distinguish between hadronic and electromagnetic cascades, one will not know if there was a NC event or an electron neutrino CC event. In addition, approximately 70 % of Glashow resonance events will produce a hadronic cascade while about 10 % of them will produce an electromagnetic cascade. Therefore, all the aforementioned event types can be summarized to appear solely as cascade-like events. And assuming the same flux for all neutrino flavours, this will lead to the fact that from energies $E_\nu \gtrsim E_\nu^{\rm res} \approx 6\,{\rm PeV}$, approximately 50 % of νN reactions[2] and nearly 80 % of $\bar\nu_e e^-$ reactions are of that type of signature.

$\nu_\mu N$ and $\nu_\tau N$ CC events will also generate a hadronic cascade. Nevertheless, at higher energies ($E_\nu \gtrsim 6\,{\rm PeV}$) all of these events also appear track-like. While in a muon neutrino event the produced muon always leaves a track behind, a tau neutrino interaction can have various signatures depending on the energy and the decay mode of the tau. At low energies, the tau decays in the direct vicinity of the event vertex while at higher energies, the tau will itself produce a track until it eventually decays. With a probability of 18 % the tau will decay into a muon, thus again leaving a track behind. In the other cases, a shower is produced so that, at high energies, a second cascade is produced at some distance from the first

---

[1]Taus with energy $E_\tau = 10\,{\rm PeV}$ travel roughly 500 m on average before decaying while a muon with the same energy has a mean range of several kilometres.

[2]The ratio $\sigma_{\rm CC} : \sigma_{\rm NC}$ is roughly 5:2 so that the fraction of solely cascade-like νN events is $\frac{2}{7} + \frac{5}{7} \cdot \frac{1}{3} = \frac{11}{21} \approx 50\,\%$.
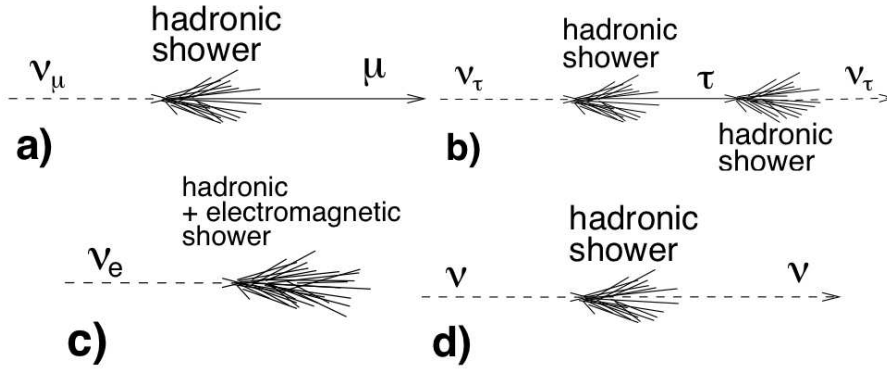
Figure 5.2: The possible νN-signatures. a) ν_μ - CC, b) ν_τ - CC, c) ν_e - CC, d) all ν - NC. See text for a detailed description. Figure taken from [33].

one. This event type, if both cascades lie in the detector, is also referred to as 'double bang' event. If just one cascade lies in the detector with a track leading to or away from it, the event is called 'lollipop' [18]. Figure 5.2 shows these possible signatures schematically.

As high energy muons and ultra high energy taus travel far distances before decaying, one will often only observe the particle crossing the detector without seeing its origin or decay. Thus, such an event appears as solely track-like. Contrariwise, as opposed to all aforementioned event types, a contained Glashow resonance event with an outgoing muon or tau produces two additional signature types. On the one hand, if a muon is produced, one has a track starting in the detector without having a cascade at its origin. On the other hand, if a tau is produced, it is possible to have a contained lollipop event. These two signatures allow for the direct measurement of the Glashow resonance [39].

A big drawback for solely track-like events is the fact that only the energy loss dE/dx, which by approximation is proportional to the particle's energy (see also section 7.1.1), can be measured and therefore, only a lower limit for the initial neutrino energy can be given.

5.2   The ANTARES Neutrino Telescope

ANTARES (Astronomy with a Neutrino Telescope and Abyss environmental RESearch) [42] is a deep-sea neutrino telescope located 40 km off the French Coast in the Mediterranean Sea at a depth of 2475 m. The schematic setup is shown in Figure 5.3. It consists of 12 detection lines, each with a length of 450 m and equipped with 25 so-called storeys at intervals of 14.5 m. The first storey on each line is located 100 m above the sea bottom. Each storey comprises 3 optical modules, each holding a 10-inch photomultiplier tube (PMT). The PMTs are oriented 45° downward with respect to the vertical recording mainly upward-going neutrino events, as ANTARES is built for an energy regime where the muon background from above does not allow for the detection of downward-going neutrino events. The lines are anchored to the sea bottom at distances of 60-70 m from each other and are hold taut by buoys at their top. Thus the total instrumented volume is roughly 10^{-2} km^3. A further line called 'instrumentation line', carries devices for environmental monitoring. Additionally, 36 acoustic sensors are installed on 6 of the ANTARES storeys, forming the AMADEUS (ANTARES Modules for the Acoustic Detection Under the Sea) [43] system which investigates the feasibility of acoustic neutrino detection.
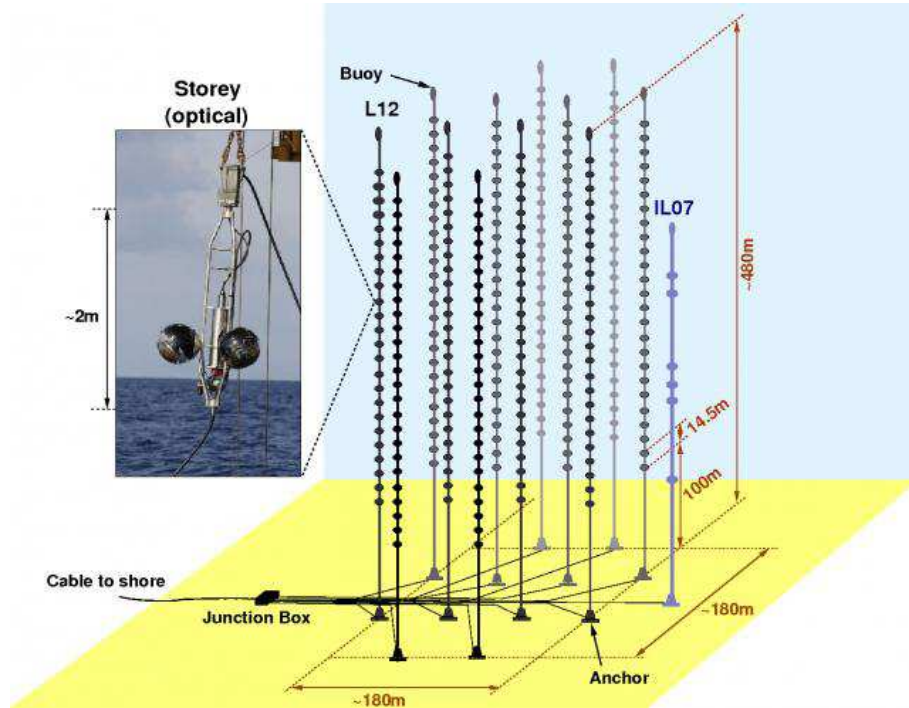
Figure 5.3: Schematic design of the ANTARES detector with its 12 lines and the instrumentation line 'IL07'. Also shown is a storey carrying 3 optical modules.

5.3 KM3NeT - Research Infrastructure in the Mediterranean Sea

Besides ANTARES, two other European neutrino observatory projects were initiated in the 1990s, called NEMO and NESTOR, which focused on research and development work. The NEMO project is directed by Italian groups while NESTOR started out as a Greece-centred, originally international collaboration [40]. The collaborations of these three groups joint together to form the KM3NeT consortium with the goal to build a cubic kilometre sized neutrino telescope in the Mediterranean Sea, the KM3NeT detector. Up to now, two major achievements are a Conceptual Design Report [44] and a Technical Design Report [45]. The final detector layout is not yet fixed. Nevertheless, important steps have been made towards a final design, regarding the individual components of the telescope, as the preparatory phase (PP) ended end of February 2012, which was supported by the EU. Figure 5.4 shows a schematic design of KM3NeT. The total instrumented volume is expected to be roughly $6 \, \text{km}^3$ containing 320 vertical structures called detection units (DUs) or towers. These DUs, each with a height of nearly 1 km, will be placed on the sea bottom in a distance of about 150-180 m from one another. Every single tower consists of 20 storeys, which are 40 m apart and each of which will hold a vertical bar structure of 6 m length (see Figure 5.5). The towers are constructed in such a way that two successive bar structures will be perpendicular to each other, which is illustrated in Figure 5.5. On the end of each bar a spherical so-called digital optical module (DOM) is attached. A DOM is composed of 31 three inch photomultiplier tubes (PMTs) which are the actual detection elements that measure the Cherenkov-Radiation eventually arising from the neutrino events. The layout of the DOM and a PMT is shown in Figure 5.6. Also included in the DOMs is the data acquisition system.

   Therefore, when fully constructed according to this design, KM3NeT will host 396,800 PMTs in 12,800 DOMs in total. In this study, a smaller configuration was used which was up to date to the beginning of the study, defined as part of the preparatory phase. This configuration is about half the size described above, with 154 DUs and a total instrumented volume of roughly $3 \, \text{km}^3$, which is a cylinder with a radius of 1.16 km and a height of 0.76 km starting 100 m above the sea bottom. An important value
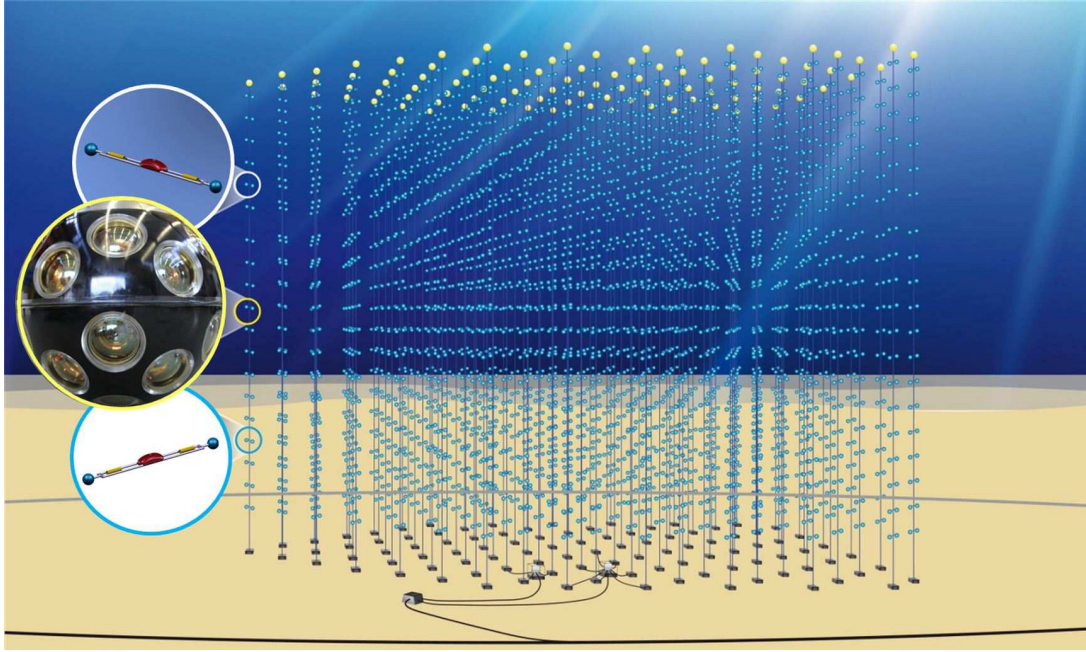
Figure 5.4: Schematic view of KM3NeT

Figure 5.5: The planned storeys in KM3NeT: The left Figure shows the layout of a storey. The Figure on the right illustrates how two consecutive storeys are positioned with respect to each other.

for simulations is the so called-can volume, which is the volume in which detectable Cherenkov light can be produced. It is an extension of the instrumented volume by several times the maximum photon absorption length in water (see also section 7.1). For this configuration the can volume is roughly $6\,\mathrm{km}^3$.

Figure 5.6: The digital optical module (left) and a photomultiplier tube (right) as planned to be used in KM3NeT.
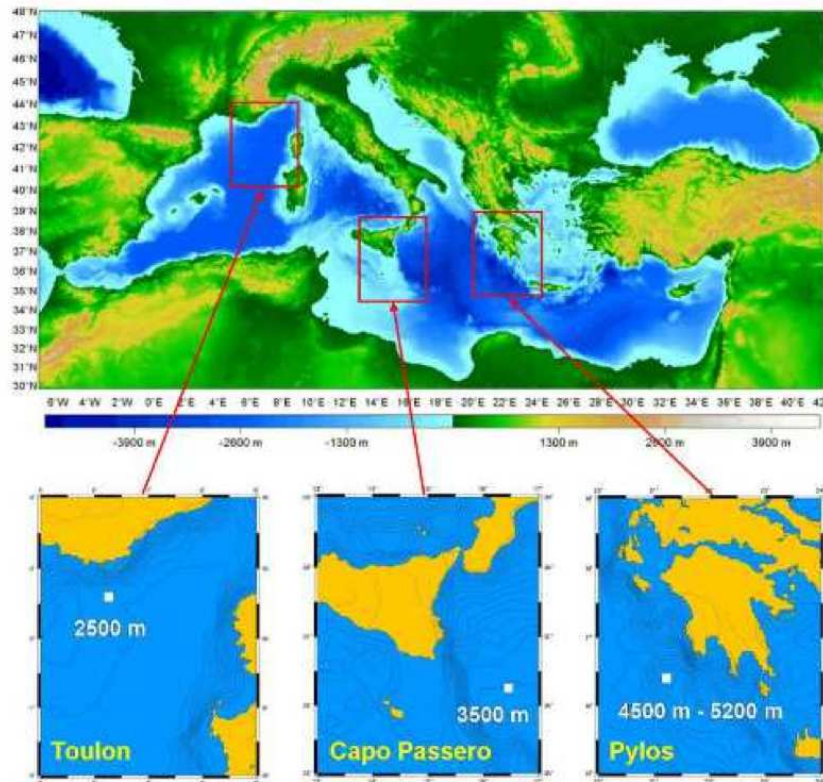

Figure 5.7: Possible sites of KM3NeT

As of the time of this study, no decision on the site of the detector has been made. Possible sites include the locations of the existing projects, ANTARES near Toulon with a depth of 2500 m, NEMO near Capo Passero off the coast of Sicily with a possible depth of 3500 m and NESTOR of the Greek coast near Pylos with a depth up to 5200 m. The possible sites are depicted in Figure 5.7. The site plays an important role, as for example a great depth will on the one hand reduce background like atmospheric muons, but on the other hand will demand higher robustness of the detector components and will make the construction more difficult.

Chapter 6

ANTARES Simulation Software

For the simulation of neutrino events in the ANTARES and KM3NeT deep-sea neutrino telescopes, neutrino interactions are generated in the vicinity of the detector. The secondary particles produced in these interactions are recorded and afterwards propagated through the sensitive volume of the detector. The same is done for atmospheric background muons. For both shower- and track-like events, Cherenkov light is produced and propagated to the detector elements. Together with the optical background present in the deep sea, hits triggering the detector and all hits in a given time window around these hits are recorded, from which the reconstruction of the simulated events can be performed.

For all parts of this simulation chain dedicated software exists for ANTARES, most of which is supposed to be adopted for high energy event simulation in KM3NeT. In the scope of this study the software packages GENHEN and GEASIM were investigated. The former is responsible for the generation of neutrino interactions while the latter simulates the detector response to particle showers. Both of these two packages turn out to be not fully suitable for the simulation of ultra high energy events. In the following sections, these packages are described further together with the problems that have been encountered. This chapter will be concluded with the results from first simulations with Geant4, a simulation software for particle tracking, that have been done in the scope of this work.

6.1 GENHEN

GENHEN [46, 47] is the first step of the simulation chain for Monte Carlo production in ANTARES. It is responsible for the generation of neutrino events of all flavours. All secondary particles produced in the generated neutrino events are stored, together with detailed information on the interaction, in an output file so that they can be processed further. The functionality and the basic content of the output files will be characterized in the following. Afterwards the issues that have been encountered by evaluating these output files are discussed.

6.1.1 Functionality

GENHEN generates high energy neutrino events in the so-called generation volume and stores the outcomes of these interactions. The generation volume exceeds the instrumented volume of the detector such that it will contain all potentially observable neutrino interactions of a given energy range. Thus, the extents of the generation volume depend on the generated neutrino and the simulated interaction type. As the CPU-time required for the simulation grows with the generation volume, the user needs to determine which neutrino type and which interaction type to simulate, so that only the smallest required volume is used for the simulation. As seen in section 5.1.2, charged current ν_μ and ν_τ interactions as well as the Glashow resonance, produce track like events for which, consequently, the generation volume exceeds the can volume of the detector. Since the range of the produced muons and taus depend on the energy, different

energy regions are treated separately, too. For all neutral current interactions and charged current ν_e interaction far beyond the Glashow resonance, the generation volume is equal to the can volume as only cascades are produced.

In events with a track-like signature, that are generated outside the can volume, the muon or tau that is produced in the neutrino interaction is propagated through the surrounding medium using dedicated propagation code. The events are stored if they reach the surface of the can, by recording their position, direction and energy. Otherwise, they are discarded. Every secondary particle resulting from an interaction generated inside the can is stored the same way. The stored events are written to an output file that is meant to be further processed with appropriate software tools. Besides the position, direction and energy of the produced secondaries, corresponding quantities for the generated neutrino are stored, too, together with the Bjorken kinematic variables x and y of the interaction. To account for the probability that a generated event occurs, additionally the interaction cross section of each simulated event is written to the output file together with other quantities that allows for assigning a weight to the event (see [48]).

The user of GENHEN also defines the energy range of the generated neutrinos. For the KM3NeT experiment and especially for the simulation of cosmogenic neutrinos reaching highest energies, a comprehensive simulation tool capable of simulating interactions up to 10^{12} GeV, in the scope of known errors (see chapter 4), is necessary. However, as will be seen in the next section, from energies of about 10^8 GeV, interactions simulated with GENHEN show unphysical behaviour regarding the interaction cross section and the distribution of the Bjorken y variable.

6.1.2   Behaviour at High Energies

To study the behaviour of GENHEN at high energies, simulations have been performed for each (anti-)neutrino flavour as well as for each interaction type in an energy region of 10^8 GeV $\leq E_\nu \leq 10^{11}$ GeV. With the particle and antiparticle of each flavour, together with the neutral and charged current interactions, this gives a total of $2 \cdot 3 \cdot 2 = 12$ event output files that were analysed. For each particle and interaction type the number of generated neutrinos was chosen such that the number of detectable interactions is sufficiently large to obtain good statistics. For this reason the number of simulated interactions with track-like signature was several orders of magnitude higher than for interaction types that only have to be produced in the can. As the regarded energy region is far beyond the Glashow resonance, all $\bar{\nu}_e$ events are cascade-like and therefore their generation volume is equal to the can volume. Table 6.1 summarizes the parameters used for each simulation including generation volume and number of produced detectable events.

The behaviour of the cross section σ_{tot} and the distribution of the inelasticity y given by the simulation was analysed. The cross section that is calculated in the GENHEN simulation is shown in Figure 6.1 together with the cross sections from Figure 4.3 as a function of the energy. The simulated cross sections grow stronger until $E_\nu \approx 10^{9.5}$ GeV by comparison, but still in the scope of known errors. This can be explained by the fact that different extrapolations of the parton distributions are used in GENHEN compared with those that were used to calculate the cross sections from Cooper-Sarkar et al. which are used in this work. In GENHEN PDFs from the CTEQ collaboration are used, while Cooper-Sarkar et al. used HERAPDF1.5 parton distributions. For $E_\nu \gtrsim 10^{9.3}$ GeV for CC events and $E_\nu \approx 10^{9.8}$ GeV for NC events the cross section shows unphysical behaviour by dropping down far below theoretical values.

For the analysis of the inelasticity, the energy range from 10^8 to 10^{11} GeV is divided into 6 bins of equal size and for each bin the mean value is formed. Its distribution with energy is shown in Figure 6.2 together with the mean distribution developed in section 4.3 (Figure 4.5). The values determined in the simulations strongly deviate from the theoretical calculations.
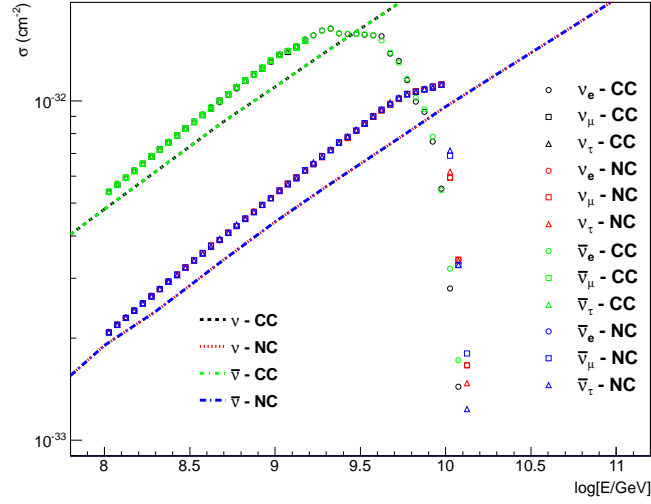
Figure 6.1: The cross section as calculated in GENHEN simulations (markers) compared to the cross section from [38] (dashed lines). Until they start to drop, the simulated cross sections for CC and NC events, respectively, are the same for all types of neutrinos. The stronger rise compared to the cross sections used in this work until $E_\nu \approx 10^{9.3}$ GeV and $E_\nu \approx 10^{9.8}$ GeV, respectively can be explained by the use of different PDFs for their calculation.
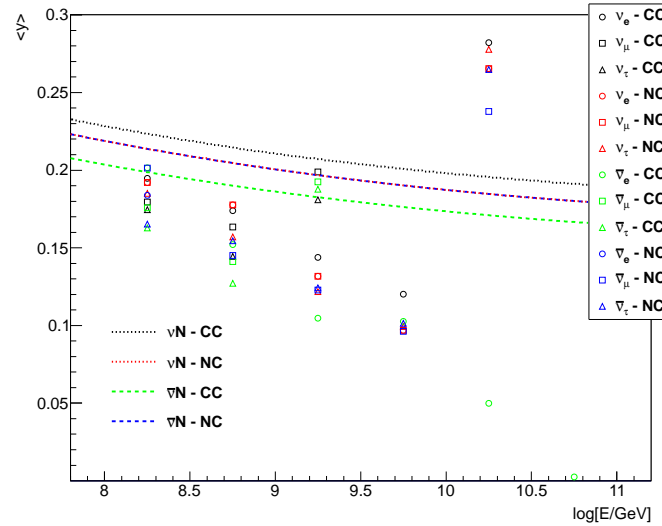

Figure 6.2: The mean inelasticity $\langle y \rangle$ as simulated with GEHEN (markers) compared to the analytical distribution of $\langle y \rangle$ developed in section 4.3 (black line). The values determined from the simulations are below the theoretical ones, except for the second to last bin where they are higher. This indicates an incorrect simulation of the physics at high energies by GENHEN. The number of entries in each energy bin is of the order of 10^2-10^3. For the last bin only entries for $\bar{\nu}_e$ - CC simulations exist, all of which are equal to zero.

Interaction	N_{gen}	N_{det}	$V_{\text{gen}}/\text{km}^3$
ν_e - CC	10^3	946	5.67
ν_μ - CC	$5 \cdot 10^7$	1938	$2.40 \cdot 10^5$
ν_τ - CC	$5 \cdot 10^7$	1137	$2.40 \cdot 10^5$
ν_e - NC	10^3	946	5.67
ν_μ - NC	10^3	946	5.67
ν_τ - NC	10^3	932	5.67
$\bar{\nu}_e$ - CC	10^3	1059	5.67
$\bar{\nu}_\mu$ - CC	$5 \cdot 10^7$	1892	$2.40 \cdot 10^5$
$\bar{\nu}_\tau$ - CC	$5 \cdot 10^7$	1102	$2.40 \cdot 10^5$
$\bar{\nu}_e$ - NC	10^6	11166	5.67
$\bar{\nu}_\mu$ - NC	10^3	946	5.67
$\bar{\nu}_\tau$ - NC	10^3	932	5.67

Table 6.1: The quantities for the different simulated νN interactions with GENHEN in the energy range 10^8 to 10^{11} GeV. The can volume of the detector used in the simulations is $V_{\text{can}} = 5.67\,\text{km}^3$. N_{gen} is the input number of neutrino interactions that are generated in V_{gen}. It can be seen that $V_{\text{gen}} \gg V_{\text{can}}$ where events with track-like signature are simulated. N_{det} is the number of produced detectable events. For most cases the simulation time exceeded the allowed CPU-time so that for a complete simulation N_{det} would be bigger for the same amount of generated neutrinos. Only the $\bar{\nu}_e$ - CC simulation was performed completely so that here N_{det} is in fact bigger than N_{gen}. This is due to the way how GENHEN calculates the number of generated interactions in each energy bin, so that the total number of generated events might differ from the user input N_{gen}.

6.2   GEASIM and GEANT

GEASIM [49] is a software package that simulates the detector response to particle showers in ANTARES by computing the Cherenkov light produced at the passage of charged particle tracks in water and its propagation. It is based on GEANT which is a software package developed at CERN for the simulation of the passage of particles through matter. GEASIM uses version 3.21 of GEANT which is written in Fortran. However, Geant3 is not capable of simulating highest energy particle showers satisfactorily (see below) and therefore the new generation of GEANT, Geant4 [50], is used which is supposed to be a future standard for simulations of that sort in KM3NeT. It is a complete rewrite in C++ and the first to use object oriented programming of GEANT. In the following the basic concepts and characteristics of GEASIM will be described and after a short description of Geant4, first results on simulations of electromagnetic showers with Geant4 will be presented.

6.2.1   GEASIM

GEASIM uses, among others, GENHEN shower simulation output files as input and is responsible for the generation of Cherenkov light output from electromagnetic and hadronic cascades. It propagates the produced Cherenkov photon through the deep-sea medium and simulates the hits in the detector elements. For this purpose a geometric volume in the form of a cuboid, filled with sea water, is defined as the volume (see also next section) in which the shower is generated. After propagation of the Cherenkov photons produced from this shower, the probability of producing a hit in a PMT is calculated. The

properties necessary to calculate the hit probabilities include the spectral quantum efficiency and angular acceptance of the PMT together with the transmissivity of the glass sphere covering the PMT. Hereupon, ^{40}K background hits can be added to the simulated signal hits. The user may specify a different detector geometry than given by the input file. Then, from the total of all photon hits, the detector response is simulated and stored in an ASCII file that thereupon can be used for event reconstruction.

Hadronic showers at higher energies (from about 100 PeV) grow in complexity in such a way that full simulations in GEASIM lead to a collapse of the programme. Therefore and for the acceleration of lower energy shower simulations, the one particle approximation (OPA) has been introduced [51, 52], which converts every single hadron, directly produced in a neutrino event, into an electromagnetic shower with an adjusted total energy output. The electromagnetic showers in GEASIM are not fully simulated but rather parametrized with a Cherenkov light output directly correlated to the shower profile and energy output in space and time. However, it turned out [53] that from energies of about 1 PeV the Cherenkov photon output in the OPA decreased notably in comparison with the complete shower simulation. To bypass these problems and enhance the OPA as well as to offer shower characteristics at highest energies, it was decided to use Geant4, the newest generation of GEANT, for the investigation of showers.

6.2.2 Simulations with Geant4

Like Geant3, Geant4 is a toolkit for the simulation of the passage of particles through matter. However, as opposed to Geant3 it is written in C++ and therefore offers object-oriented use. It is regularly updated and enhanced, the current version is 9.5. It is a very complex simulation tool, which to handle requires considerable expertise.

In the context of the simulation, the user chooses the geometry and media where the simulation shall take place. The geometry is defined by volumes, in the simplest case boxes, cylinders and spheres, that can also be placed into one another. Volumes are filled with material of user-defined chemical composition. For example, for a single element the user declares the atomic number Z and mass A. From single elements one can make molecules such that for pure water the user defines hydrogen ($Z = 1$, $A = 1$ g/mol) and oxygen ($Z = 8$, $A = 16$ g/mol) and puts them together with a ratio of 2 : 1 and an arbitrary molecular density ρ. To generate, for instance, deep-sea salt water the user just adds the respective elements and molecules. Volumes may also be declared as sensitive detector elements so that hits can be simulated. In addition electric and magnetic fields can be activated. The user specifies all particles that shall be producible and tracked, including all kinds of leptons and almost all kinds of mesons and baryons, and defines all physical processes which shall be simulated. This includes, among others, hadronic interactions, particle decays and more than 60 electromagnetic processes. Finally the user defines a 'particle gun' that generates particles of a chosen type at a given point in space with given energy and direction or momentum, respectively. These quantities may also be chosen to be generated randomly with a certain distribution or spectrum. The simulation itself, that is the tracking of each particle, is processed in steps. Each activated continuous physical process is applied along each step while discrete processes happen at the end of each step. The decision, whether the process happens, is made by computing the probability of the process occurring. Any produced particles are tracked and any energy loss and momentum change is stored at the end of each step as well as the position. With the aid of graphics software the simulations can be visualized in a three-dimensional fashion. For more on the functionality of Geant4 see also the online documentation [54].

In the scope of this thesis, first Geant4 simulations of electromagnetic showers have been performed to check the operability of Geant4 and to verify theoretical descriptions of electromagnetic showers. Following these descriptions (see for example [37]), the longitudinal profile of a shower can be parametrized as a gamma distribution:

$$\frac{\mathrm{d}E}{\mathrm{d}t} = E_0 \, b \, \frac{(bt)^{a-1} \, \mathrm{e}^{-bt}}{\Gamma(a)} \tag{6.1}$$
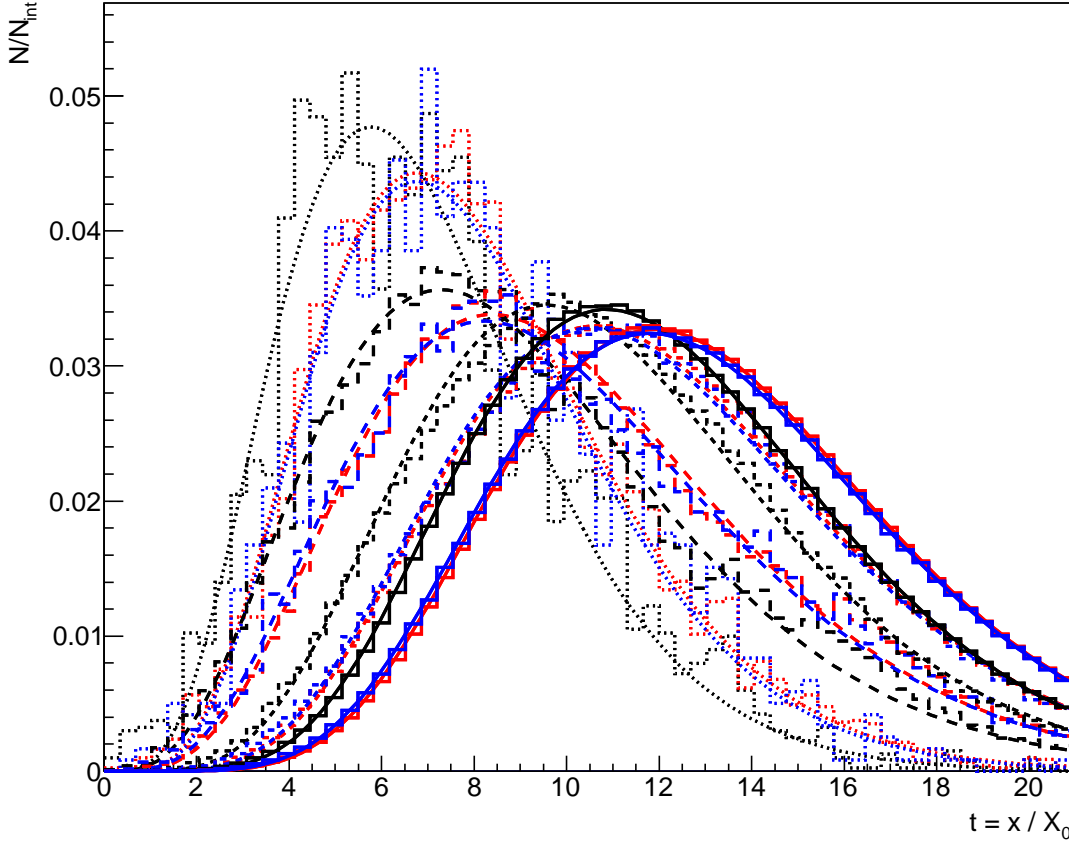
Figure 6.3: Geant4 simulation results for electromagnetic showers. The normalized number of particles N/N_{int} produced at a distance $t = x/X_0$ from the shower vertex is shown for γ (black), e^- (red) and e^+ (blue), for a primary electron particle energy of 100 GeV (dotted), 1 TeV (long dashed), 10 TeV (short dashed) and 100 TeV (solid). Also shown are fits of the gamma distribution (smooth curves) to the respective histograms.

with the gamma function $\Gamma(a)$ and parameters E_0, a and b. The distance $t = x/X_0$ is measured in units of radiation length X_0. For sea water at the ANTARES site $X_0 = 35$ cm. Figure 6.3 shows the results for sea water shower simulations with Geant4. Shown are the normalized numbers of gammas, electrons and positron produced for different shower energies (100 GeV, 1 TeV, 10 TeV and 100 TeV) together with fits of the gamma distribution. These results confirm qualitatively the results from earlier works [55–57] with simulations up to 1 PeV. The next steps would be a comprehensive quantitative confirmation of the shower energy deposition profile and thereupon the simulations of very high energy electromagnetic and hadronic showers with energies above 1 PeV. At these energies a suppression of the pair production and bremsstrahlung cross sections has to be taken into account, the so-called LPM effect, which leads to a vast increase of the radiation length [58].

Chapter 7

Calculation of Expected Event Rates

This chapter presents the expected event rates from cosmogenic neutrinos in KM3NeT. It will be compared to the expected background events from the atmospheric neutrino flux. In Figure 7.1, a comparison of models of these two fluxes is presented. It can be seen that the cosmogenic flux begins to predominate over the atmospheric flux roughly at around some PeV.
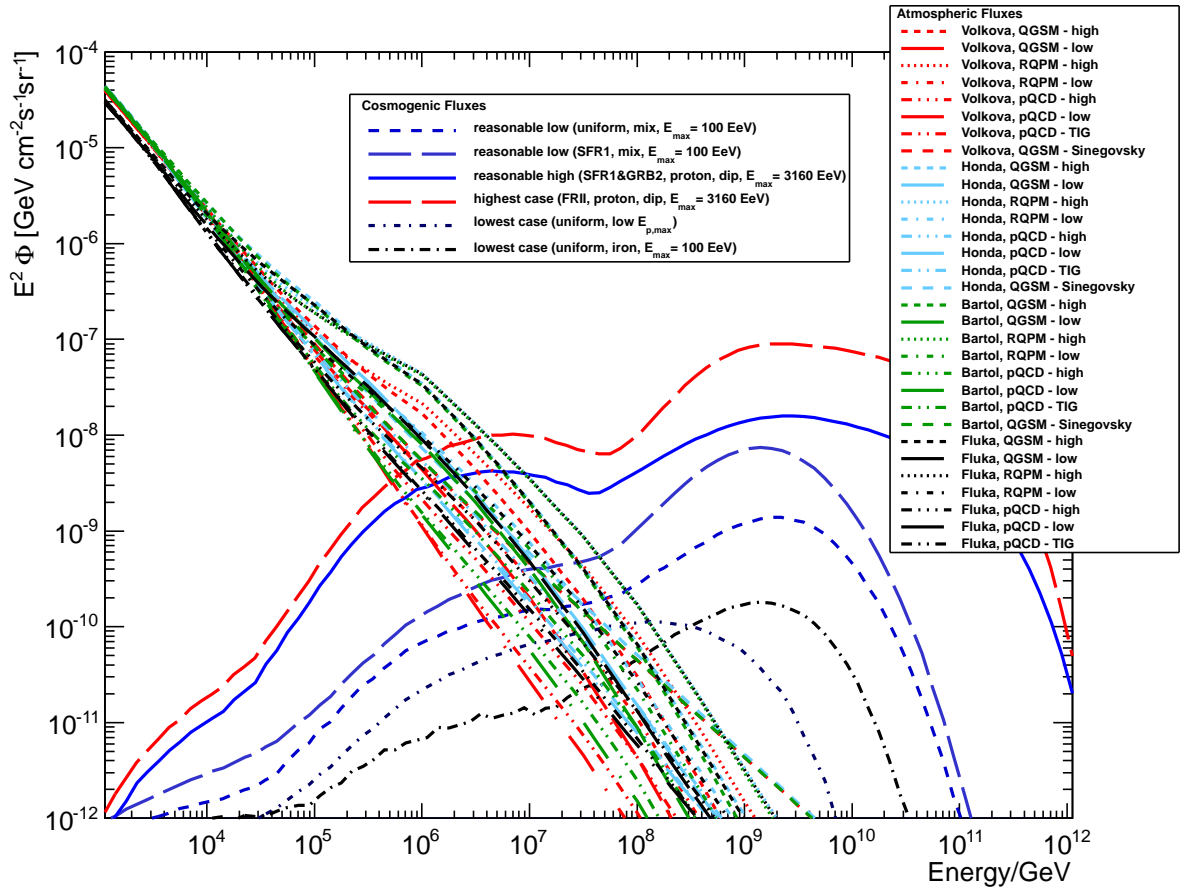

Figure 7.1: Comparison of the cosmogenic neutrino flux models with the models for the atmospheric neutrino flux. The cosmogenic flux begins to predominate somewhere in the energy range of 1 to 10 PeV for the moderate models. Considering also the extreme predictions, this energy region ranges from approximately 0.5 to 100 PeV.

For a given diffuse neutrino flux $\Phi(E)$, a rough calculation gives an estimate for the number of neutrinos crossing the detector in a given time: The flux tells us how many particles per unit time and area come from a direction $d\Omega$ in an energy range $E \leq E_\nu \leq E + dE$. Because the flux is isotropic, multiplication with 4π gives the number of particles from all directions. Due to the fact that absorption of neutrinos in the earth plays a major role at high energies, only the upper hemisphere is considered so that a value of 2π is taken. For simplicity of the calculation one can assume the detector as a sphere with can volume $V = 6\,\text{km}^3$, which gives a cross-sectional area of $A = \pi R^2$ with $R = 1.13\,\text{km}$. If we also assume the flux following an E^{-2}-spectrum so that $E^2\Phi(E)$ is constant, one gets the number of neutrinos N_ν with energies $E_1 \leq E_\nu \leq E_2$ crossing KM3NeT in a given time T by the following expression:

$$N_\nu = 2\pi^2 R^2 T\, E^2 \Phi(E) \cdot \left(E_1^{-1} - E_2^{-1}\right). \tag{7.1}$$

Taking $E_1 = 3\,\text{PeV}$, $E_2 = 100\,\text{PeV}$ and $E^2\Phi(E) = 10^{-8}\,\text{GeV}\,\text{s}^{-1}\,\text{cm}^{-2}\,\text{sr}^{-1}$ which corresponds approximately to the highest prediction of cosmogenic neutrino fluxes at $E_\nu = 3\,\text{PeV}$ (see figure 7.1) and is in the range of the Waxman-Bahcall bound (equation (3.10)), we get a number of neutrinos crossing the detector of 26 000 per year or 70 per day.

In section 7.2, it is calculated how many of these neutrinos will interact in the sensitive volume of the detector. The differential event rate as well as the cumulative event rate for the cosmogenic and atmospheric neutrino flux will be presented. It will also be seen that the Glashow resonance is an interesting feature in the event rate spectrum. In section 7.3, a model for the energy resolution of the detector is included in the calculations leading to an event rate spectrum as it would be measured by an, apart from the energy resolution, perfect detector. These event rates will be called smeared event rates. However, first of all, the effective area with which event rates are calculated and which is an important measure for the performance of a neutrino telescope will be discussed. The chapter will be concluded with a discussion on how the different neutrino flavours affect the various event rate spectra.

7.1 Effective Area

The number of detectable events N_ν generated from a diffuse neutrino flux $\Phi(E, \theta) = \sum_i \Phi_{\nu_i}(E, \theta)$ of all neutrino flavours in an energy range $E_1 \leq E \leq E_2$ and time window T is given by (see also [45])

$$N_\nu = 2\pi T \int\limits_{E_1}^{E_2} \int\limits_{-1}^{1} \sum_i \Phi_{\nu_i}(E, \theta) \cdot A_{\text{eff},\nu_i}(E, \theta)\, d\cos\theta\, dE. \tag{7.2}$$

Here 2π accounts for the integration over the azimuth angle and θ is the incident neutrino zenith angle in the coordinate system of the detector, so that $\theta = 0$ corresponds to a neutrino coming straight from above. The atmospheric neutrino flux varies with θ while the cosmogenic neutrino flux is expected to be independent of θ.

$A_{\text{eff},\nu_i}(E, \theta)$, which generally depends on the neutrino energy E and angle θ, is the effective area of the detector for one specific neutrino type $\nu_i \in \{\nu_e, \bar{\nu}_e, \nu_\mu, \bar{\nu}_\mu, \nu_\tau, \bar{\nu}_\tau\}$ and is given by

$$A_{\text{eff},\nu_i}(E, \theta) = \frac{\rho}{m_N} \cdot \sigma_{\nu_i}(E) \cdot V_{\text{eff},\nu_i}(E, \theta) \cdot P_{\text{earth},\nu_i}(E, \theta) \tag{7.3}$$

where $\rho = 1.025 \cdot 10^3\,\text{kg/m}^3$ is the density of deep-sea salt water and $m_N = 1.67 \cdot 10^{-27}\,\text{kg}$ is the mean nucleon mass of the target material, so that ρ/m_N is the nucleon density. $\sigma_{\nu_i}(E)$ is the 'effective sum' of cross sections for the interactions a specific neutrino type can undergo, so that $\sigma_{\nu_i}(E) = \sigma_{\text{CC}}(E) + \sigma_{\text{NC}}(E)$ for all neutrino types but electron antineutrinos and $\sigma_{\bar{\nu}_e}(E) = \sigma_{\text{CC}}(E) + \sigma_{\text{NC}}(E) + 0.556 \cdot \sigma_{\text{Gl}}(E)$. Here, σ_{CC} and σ_{NC} are the cross sections for deep-inelastic scattering charged and neutral current interaction

while σ_{Gl} is the Glashow resonance cross section (see section 4.2). The factor $10/18 \approx 0.556$ accounts for the fact that the Glashow resonance only occurs in interactions with electrons and that there are approximately 10 electrons per 18 nucleons in sea water.

$P_{earth,\nu_i}(E,\theta)$ is the transmission probability through the earth for a neutrino coming from direction θ. It is given by

$$P_{earth,\nu_i}(E,\theta) = \exp\left(-\frac{\sigma_{\nu_i}(E)}{m_N} \int \rho_\theta(l)\,dl\right) \tag{7.4}$$

with $\rho_\theta(l)$ as the density of the earth along the neutrino path through earth to the detector. In the formula, it is neglected that further neutrinos may originate from their interactions in the earth. For neutrinos coming from the upper hemisphere up to $\theta \lesssim 100°$ the transmission probability is approximately equal to unity. But especially for ultra high energy ($E_\nu \geq 1\,\text{PeV}$) upward-going neutrinos absorption in the earth becomes a crucial factor (for detailed simulations of the track of neutrinos through earth see [46]).

The effective volume $V_{eff,\nu_i}(E,\theta)$ accounts for the detection efficiency and is evaluated from the number of events $N_{rec,\nu_i}(E,\theta)$ being successfully reconstructed from a number of generated neutrino interactions $N_{gen,\nu_i}(E,\theta)$ in a generation volume $V_{gen,\nu_i}(E)$, so that

$$V_{eff,\nu_i}(E,\theta) = \frac{N_{rec,\nu_i}(E,\theta)}{N_{gen,\nu_i}(E,\theta)} \cdot V_{gen,\nu_i}(E). \tag{7.5}$$

For $N_{rec,\nu_i}(E,\theta)$ one can write:

$$N_{rec,\nu_i}(E,\theta) = \varepsilon_{\nu_i}(E,\theta) \cdot N_{gen,\nu_i}(E,\theta), \tag{7.6}$$

so that the effective volume can also be written as

$$V_{eff,\nu_i}(E,\theta) = \varepsilon_{\nu_i}(E,\theta) \cdot V_{gen,\nu_i}(E,\theta), \tag{7.7}$$

with the detection efficiency $\varepsilon_{\nu_i}(E,\theta)$. The detection efficiency will in general be different for each separate event signature (see section 5.1.2) so that one can define[1] ε_{sh}, ε_μ and ε_τ as the detection efficiencies for showers, muon and taus, respectively, that are produced in neutrino interactions. If additionally, one defines w_{Gl} as the probability that the Glashow resonance occurs in an $\bar{\nu}_e$ interaction[2], and given that for the cross sections $\sigma_{CC} : \sigma_{NC} \approx 5 : 2$ (see section 4.1) one can write

$$V_{eff} = \begin{cases} \varepsilon_{sh} V_{gen,\,sh} & \text{for } \nu_e, \\[2ex] (1 - w_{Gl})\,\varepsilon_{sh}\,V_{gen,\,sh} + w_{Gl}\,(\,0.78\,\varepsilon_{sh}\,V_{gen,\,sh} + 0.11\,\varepsilon_\mu\,V_{gen,\,\mu} + 0.11\,\varepsilon_\tau\,V_{gen,\,\tau}) & \text{for } \bar{\nu}_e, \\[2ex] \left(\frac{5}{7}\,\varepsilon_\mu\,V_{gen,\,\mu} + \frac{2}{7}\,\varepsilon_{sh}\,V_{gen,\,sh}\right) & \text{for } \nu_\mu, \bar{\nu}_\mu, \\[2ex] \left(\frac{5}{7}\,\varepsilon_\tau\,V_{gen,\,\tau} + \frac{2}{7}\,\varepsilon_{sh}\,V_{gen,\,sh}\right) & \text{for } \nu_\tau, \bar{\nu}_\tau. \end{cases}$$

Here, the values 0.78 and 0.11 account for the probabilities for the different reaction channels at the Glashow resonance and $V_{gen,sh/\mu/\tau}$ are the generation volumes for the specific signature types. In simulations, the size of the generation volumes is selected sufficiently large so that generated events outside of

---

[1]From this point on, the notation of the dependencies on neutrino type, energy and direction is omitted, though in general, all quantities still depend on those parameters.

[2]Due to time constraints $w_{Gl}(E)$ could not be calculated.

it would never be successfully measured or reconstructed. For showers typically $V_{\text{gen, sh}} = V_{\text{can}}$, with V_{can} as the volume of the so called can which is the region where detectable Cherenkov light can be produced (see also section 5.3). It is defined as an extension of the instrumented volume by several times the maximum photon absorption length in every direction. Its base is limited by the sea floor. For muons and taus the generation volume is adjusted to the respective particle ranges in water and rock. The detection efficiency is the probability that an event triggers the detector and is thereupon successfully reconstructed. Thus each detection efficiency $\varepsilon_i, i \in \{\text{sh}, \mu, \tau\}$, can be expressed as

$$\varepsilon_i = \varepsilon_{\text{trig}, i} \cdot \varepsilon_{\text{rec}, i} \tag{7.8}$$

where the trigger efficiency $\varepsilon_{\text{trig}, i}$ is the probability of an event triggering the detector and the reconstruction efficiency $\varepsilon_{\text{rec}, i}$ is the probability of an event being successfully reconstructed.

To determine the values of the detection efficiencies, detailed simulations of all possible event signatures have to be performed. Up to now, such simulations for deep-sea telescopes have been done for ANTARES and KM3NeT for specific event types up to energies of $\approx 10 \, \text{PeV}$ (see for example [33, 59–62]). For higher energies, i.e. for the simulation of ultra high energy neutrino events, no software capable of doing that is available, as also mentioned in chapter 6. Therefore, the determination of the exact effective area of KM3NeT to cosmogenic neutrinos goes beyond the scope of this work. Instead, the calculation of the event rates of the cosmogenic neutrino flux in KM3NeT will be made with the approximation $\varepsilon_{\nu_i}(E, \theta) = 1$ and the calculations of smeared event numbers will be limited to contained shower events. Figure 7.2 shows the effective area that follows from these approximation and which is used for the event rate calculation.

First attempts have been made to approximate the trigger efficiency for all kinds of signatures by doing Monte Carlo simulations for, on the one hand, the probability a shower generated in the can, and on the other hand, the probability a muon or tau, generated in their respective generation volumes produces detectable Cherenkov photons. These probabilities will be called observation probabilities and are discussed in the following section.

7.1.1   Observation Probability

The probability of an event triggering the detector, the trigger efficiency $\varepsilon_{\text{trig}}$, can be expressed as

$$\varepsilon_{\text{trig}} = \varepsilon_{\text{obs}} \cdot \varepsilon_{\text{ph}}, \tag{7.9}$$

where ε_{obs} is the probability that an event produces a certain amount of Cherenkov photons reaching the detector and ε_{ph} is the probability that these photons trigger the detector. The former one can also be interpreted as the probability that an event is observed by the detector (without triggering). By reason of that, this will be called the observation probability. In the following, simple studies of the observation probability for showers and muons and its effect on the effective volume are presented. As the exact amount of produced Cherenkov photons cannot yet be determined[3], approximations will be made for each event type. Unfortunately, due to time constraints, the results could not be included in the calculations of the event rates in section 7.2.

ε_{obs} for Showers

To determine the observation probability for showers, events with random position and random direction were generated inside the can volume. The energy dependence as well as the dependence on the distance to the instrumented volume is neglected in the following considerations. Thus, the only relevant parameter considered here is the shower direction. The detector volumes are considered as cylinders.

---

[3]For this purpose detailed event simulations are necessary.
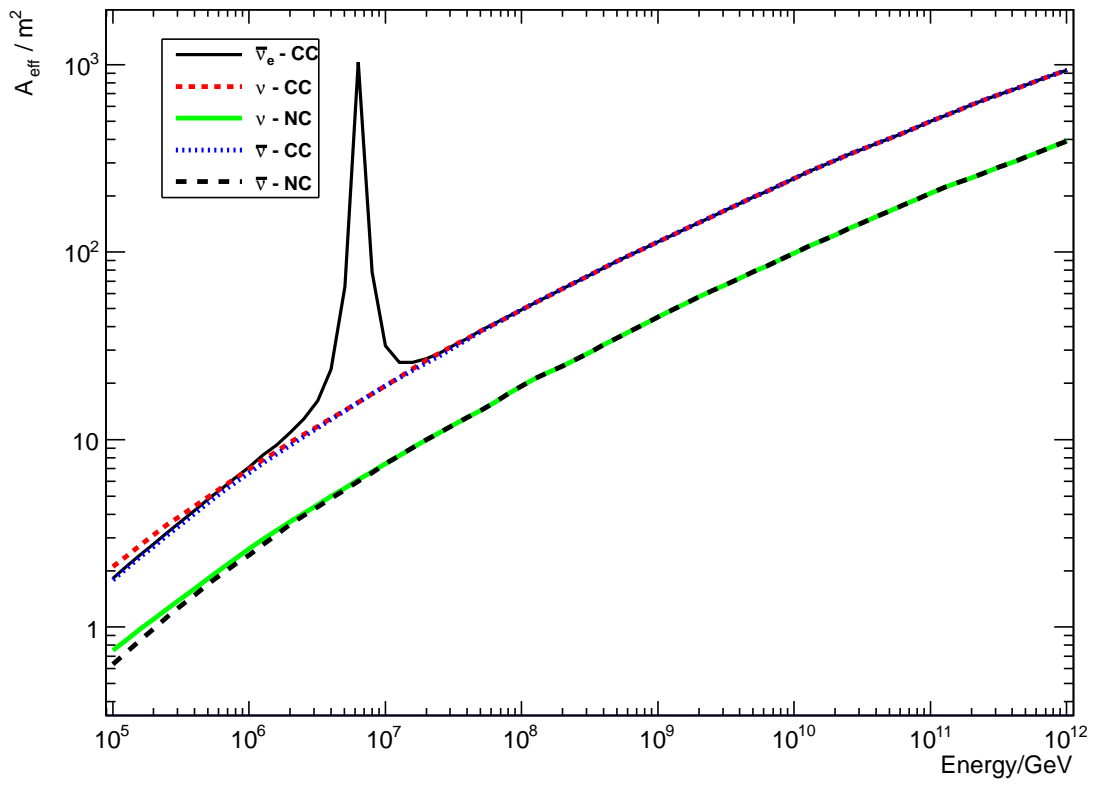
Figure 7.2: The effective area as calculated by equation (7.12). For illustration, the contributions from charged current and neutral current interactions are shown separately besides the effective area for $\bar{\nu}_e$ charged current events including the Glashow resonance.
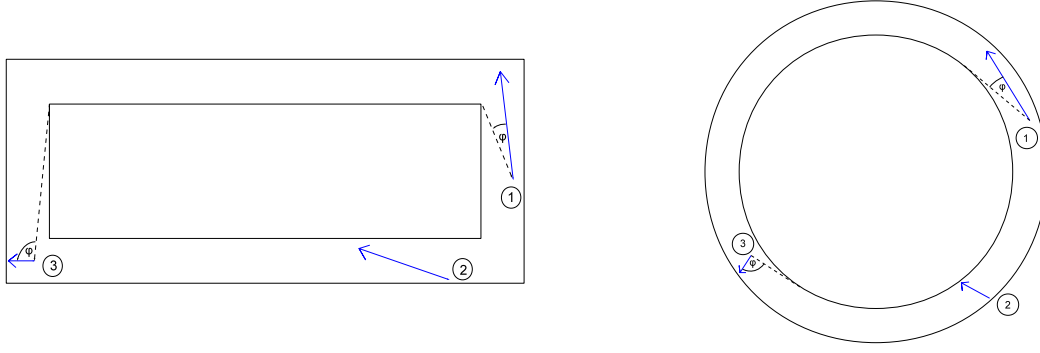
Figure 7.3: Schematic illustration of the simulation method, side view (left), top view (right). The smaller black framed area indicates the instrumented volume, the bigger one the can volume. 1) observed event pointing near the instrumented volume ($\varphi < \phi$), 2) observed event pointing to the instrumented volume, 3) unobserved event pointing too far away from the detector ($\varphi > \phi$).

ϕ	$0°$	$36°$	$\theta_C = 42°$	$72°$	$90°$	$126°$	$\gtrsim 140°$
$\varepsilon_{\text{out,obs}}$	0.349	0.546	0.607	0.839	0.943	0.99998	1
ε_{obs}	0.705	0.795	0.823	0.927	0.974	0.999991	1
$\varepsilon_{\text{obs}} V_{\text{can}}/\text{km}^3$	4.14	4.66	4.83	5.44	5.71	5.87	5.87

Table 7.1: The results of the simulations for the shower observation probability for some values of the limit angle ϕ. 10^6 events are generated inside the can for each value of ϕ. The table shows the values for the total observation probability ε_{out}, the observation probability $\varepsilon_{\text{out,obs}}$ for events produced outside the instrumented volume and the quantity $\varepsilon_{\text{obs}} V_{\text{can}}$ that goes into the effective volume.

The values used are $r_{\text{ins}} = 1.16\,\text{km}$, $h_{\text{ins}} = 0.76\,\text{km}$, $V_{\text{ins}} = 3.21\,\text{km}^3$ for the radius, height and volume of the instrumented volume, and $r_{\text{can}} = 1.34\,\text{km}$, $h_{\text{can}} = 1.04\,\text{km}$, $V_{\text{can}} = 5.87\,\text{km}^3$ for the can, so that the can is extended by $0.18\,\text{km}$ in every direction but the downward direction, which corresponds to three times the photon absorption length at $\lambda \approx 475\text{nm}$, $L_a(\lambda \approx 475\,\text{nm}) = 60\,\text{m}$. The extension downwards is $0.1\,\text{km}$. For events inside the instrumented volume $\varepsilon_{\text{obs}} \equiv 1$. For events outside the instrumented volume two cases are distinguished:

1) The shower points directly towards the instrumented volume. Then $\varepsilon_{\text{obs}} \equiv 1$.

2) The shower does not point towards the instrumented volume. Then, if the smallest angle φ between the shower direction and straight lines from the event to the boundaries of the detector is smaller than a given limit angle ϕ, $\varepsilon_{\text{obs}} \equiv 1$, otherwise $\varepsilon_{\text{obs}} \equiv 0$.

To determine if the shower points towards the instrumented volume, the shower direction is parametrized as a straight line in terms of linear algebra and it is checked if this line intersects the instrumented volume. Figure 7.3 shows this schematically.

    The simulation was performed for 11 different angles ϕ reaching from $\phi = 0°$ to $\phi = 180°$ in steps of $18°$ and additionally for the Cherenkov angle $\phi = \theta_C = 42°$. For each angle, 10^6 events were produced homogeneously distributed in the can volume and with an isotropic direction distribution. The results for certain angles are summarized in Table 7.1. Also given there is the value for $\varepsilon_{\text{obs}} V_{\text{can}} \equiv \varepsilon_{\text{obs}} V_{\text{gen}}$ which goes into the effective volume, and the probability $\varepsilon_{\text{out,obs}}$ that an event generated outside the instrumented volume will be observed. As expected, from an angle of $\phi \approx 140°$ all events are observed
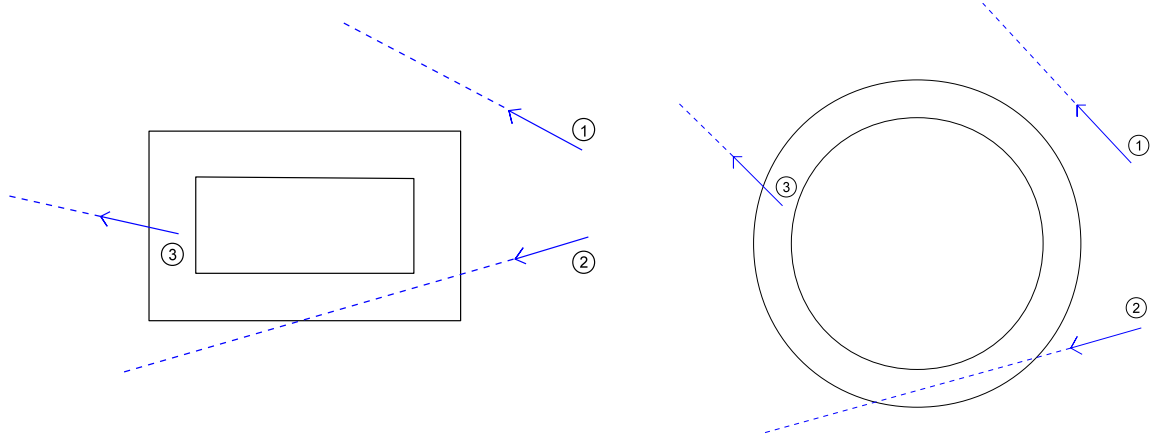
Figure 7.4: Schematic illustration of the simulation method, side view (left), top view (right). The smaller black framed area indicates the instrumented volume, the bigger one the can volume. 1) unobserved event not crossing the can, 2) observed event crossing the can, 3) unobserved event generated inside the can but outside the instrumented volume pointing too far away from the instrumented volume.

because this corresponds approximately to the highest possible angle φ an event can have. For $\phi = \theta_C$, roughly 18 % of generated events are not observed.

ε_{obs} for Muons and Taus

Similar simulations have been performed to determine the observation probability to muons and taus. The generation volume is adjusted to the energy dependent mean muon and tau range $x_{\mu/\tau}$. The muon range is determined by the ionization energy loss a and the sum of e^+e^- pair production, bremsstrahlung, and photonuclear energy losses b. These parameters vary only weakly with energy. To the approximation[4] that they are constant, the mean range of a muon with energy E is given by

$$x_\mu \approx \frac{1}{b} \ln\left(1 + \frac{b}{a} E\right).$$
(7.10)

The values used here for the range calculation are $a = 2\,\text{MeV}\,\text{cm}^2/\text{g}$ and $b = 3.5 \cdot 10^{-6}\,\text{cm}^2/\text{g}$ taken from [40]. With this formula simulations are done for muons over the whole energy range from 10^5 to 10^{10} GeV. For taus, as no such formula is known, the simulations are done for specific energies, where the tau range is derived from [64]. The generation volume for each simulation is then given by $r_{\text{gen}} = r_{\text{can}} + x_{\mu/\tau}$ and $h_{\text{gen}} = h_{\text{can}} + 2x_{\mu/\tau}$. The height is limited by the sea surface since a neutrino interaction in air above the sea surface is very unlikely. The fact that the mean range in rock (below the sea bottom) is shorter than in water is neglected in first approximation. For both the muons and taus the events are generated homogeneously and with an isotropic direction distribution within the generation volume. The particle is defined to be observed when it is generated within the can volume or, if it is generated outside of it, when it crosses the can. Figure 7.4 shows this schematically. The number of events that are generated inside the can is multiplied by the observation probability for showers as, like above, the event should not point too far away from the detector. Therefore, a reasonable value $\phi = 36°$ is chosen for the limit angle ϕ, for which $\varepsilon_{\text{obs}} = 0.795$, to get Cherenkov light from the particle track. For events generated outside the can, the particle's trajectory is parametrized as a straight line and it is checked if it crosses the can and if the distance to the can is smaller than the mean particle range. Table 7.2 summarizes the simulation results for muons and taus for given energies. Figure 7.5 presents the results for muons graphically. As a result,

---

[4]Exact values for $a(E)$ and $b(E)$ and detailed calculations on the muon range can be found in [63].

$E_{\mu/\tau}/\,$GeV	$10^{6.0}$	$10^{6.5}$	$10^{7.0}$	$10^{7.5}$	$10^{8.0}$	$10^{8.5}$	$10^{9.0}$
$x_\mu/\,$km	21.3	24.6	27.9	31.2	34.5	37.8	41.1
$V_{\mathrm{gen}}\cdot 10^{-3}/\,$km^3	40.0	59.4	84.3	115	153	199	252
$N_{\mathrm{gen}}\cdot 10^{-6}$	6.81	10.1	14.4	19.7	26.1	33.9	43.0
$N_{\mathrm{obs}}\cdot 10^{-3}$	12.6	14.5	15.9	17.3	19.1	20.2	21.8
$\varepsilon_{\mathrm{obs}}\cdot 10^3$	1.85	1.43	1.10	0.880	0.729	0.595	0.508
$\varepsilon_{\mathrm{obs}}\,V_{\mathrm{gen}}/\,$km^3	73.8	84.9	93.1	102	112	118	128
$x_\tau/\,$km	0.0491	0.155	491	1.55	4	10	17
$V_{\mathrm{gen}}/\,$km^3	6.90	9.48	21.3	109	672	5450	21700
$N_{\mathrm{gen}}\cdot 10^{-3}$	1.18	1.62	3.63	18.5	115	930	3690
$N_{\mathrm{obs}}\cdot 10^{-3}$	0.805	0.809	0.834	1.71	3.76	7.28	10.6
$\varepsilon_{\mathrm{obs}}\cdot 10^3$	684	500	230	92.0	32.8	7.84	2.88
$\varepsilon_{\mathrm{obs}}\,V_{\mathrm{gen}}/\,$km^3	4.72	4.74	4.89	10.0	22.1	42.7	62.3

Table 7.2: Simulation results for the observation probability to muons (upper part of the table) and taus (lower part) for specific energies. $E_{\mu/\tau}$ is the muon and tau energy, respectively, $x_{\mu/\tau}$ is the corresponding particle range in water. Until $E_\tau \approx 10^7$ the tau range is given by its decay length, the approximated tau range for higher energies is derived from [64]. For the number of generated particles, a constant density was chosen so that $N_{\mathrm{gen}} = 1000 \cdot V_{\mathrm{gen}}/V_{\mathrm{can}}$. Therefore, this number rises with the generation volume V_{gen} which itself rises with the particle range. The observation probability $\varepsilon_{\mathrm{obs}}$ is given by the number of observed events N_{obs} divided by the number of generated events N_{gen}. The quantity $\varepsilon_{\mathrm{obs}}\,V_{\mathrm{gen}}$ which goes into the effective Volume is of the order of $100\,$km^3 for muons. For low energy taus, due to their small range, the generation volume is approximately given by the can volume, and therefore $\varepsilon_{\mathrm{obs}}\,V_{\mathrm{gen}}$ is roughly constant. For high energy taus this quantity approximates the values for low energy muons.

it can be see that the observation volume $\varepsilon_{\mathrm{obs}}\,V_{\mathrm{gen}}$ rises by approximation logarithmically with energy or linearly with the particle range and reaches values up to $150\,$km^3. As also mentioned in section 5.1.2, a great drawback of ultra high energy track-like events is the fact that only a part of the energy is deposited in the detector. Additionally, the background of atmospheric muons will lower the detection capability, so that the effective area will not follow straightly the behaviour of the observation volume with energy.

7.2   Event Rates in the Detector

Following equation (7.2), one can write the differential event rate $\mathrm{d}N/\mathrm{d}E$ for neutrinos of energy E as

$$\frac{\mathrm{d}N}{\mathrm{d}E}(E) = 2\pi T \int_{-1}^{1} \sum_i \Phi_{\nu_i}(E,\theta) \cdot A_{\mathrm{eff},\nu_i}(E,\theta)\,\mathrm{d}\cos\theta. \qquad (7.11)$$

Again $\Phi(E,\theta) = \sum_i \Phi_{\nu_i}(E,\theta)$ is the sum of the fluxes for all neutrino flavours. In this section only events contained in the can ('contained events') are considered, which allow to draw conclusion about the measured neutrino spectrum. Looking just at the upper hemisphere and assuming a perfect detection efficiency as mentioned at the beginning of the previous section, the effective area is independent of the
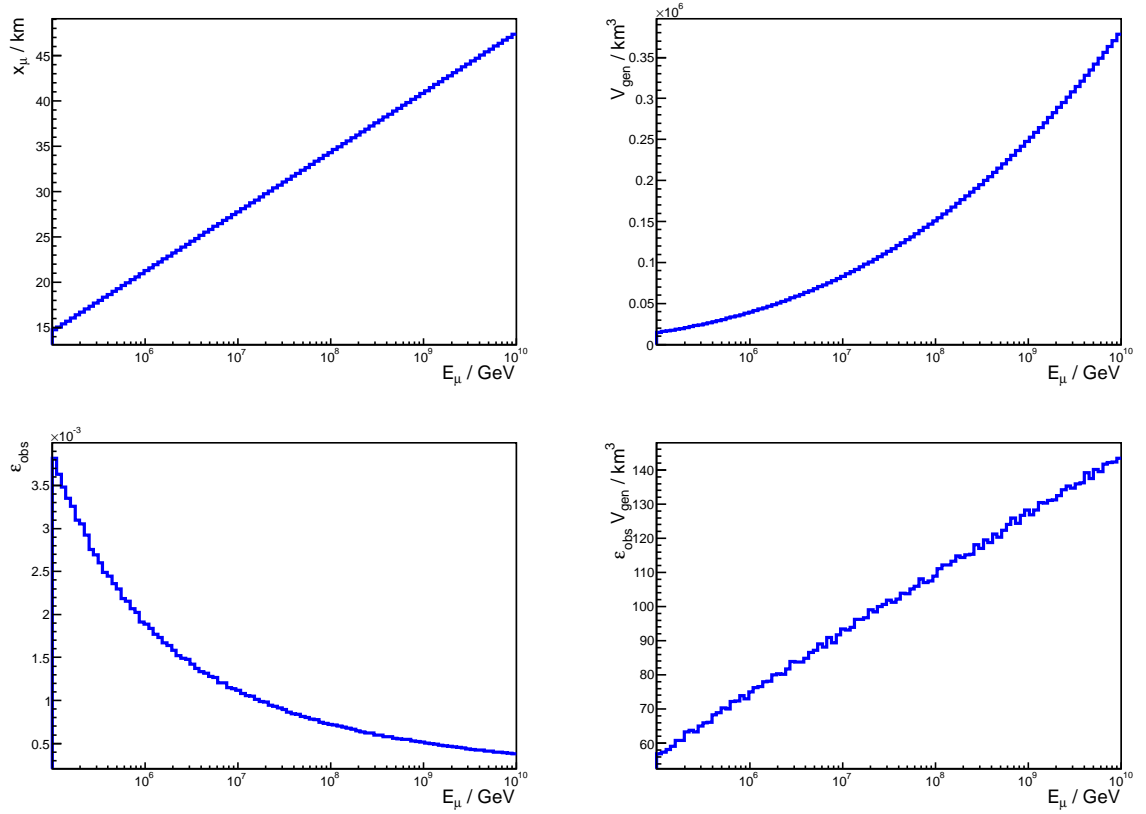
Figure 7.5: Simulation results for muons in the energy range 10^5 GeV$\leq E_\mu \leq 10^{10}$ GeV. Top left: muon range x_μ, top right: generation volume V_{gen}, bottom left: observation probability $\varepsilon_{\mathrm{obs}}$, bottom right: observation volume $\varepsilon_{\mathrm{obs}} V_{\mathrm{gen}}$. The muon range rises logarithmically with energy. As a result can be seen, that this is, by approximation, also true for the observation volume, so that $\varepsilon_{\mathrm{obs}} V_{\mathrm{gen}}$ rises linearly with the particle range.

zenith angle θ and can thus be written as

$$A_{\text{eff},\nu_i}(E) = \frac{\rho}{m_N} V_{\text{can}} \cdot \sigma_{\nu_i}(E) \tag{7.12}$$

which only differs for $\bar{\nu}_e$ from the other neutrino types as the Glashow resonance must be considered. This effective area as a function of the energy is shown in Figure 7.2. The integration over $\cos\theta$ (from 0 to 1) can then be evaluated which gives the zenith angle integrated neutrino flux $\Phi(E)$. Thus, the differential event rate for one specific neutrino type is now given by

$$\frac{\mathrm{d}N}{\mathrm{d}E}(E) = 2\pi T\, N_N \cdot \Phi(E) \cdot \sigma(E), \tag{7.13}$$

where the dependence on neutrino type is omitted and with $N_N = V_{\text{can}}\rho/m_N$ as the number of nucleons in the can volume.

From this equation follows that the event rate of neutrinos of a given type in an energy bin at energy E of width $s = \Delta E$ is given by

$$N(E) = 2\pi T\, N_N \int\limits_{E-\Delta E/2}^{E+\Delta E/2} \Phi(E) \cdot \sigma(E)\,\mathrm{d}E. \tag{7.14}$$

In a logarithmic plot this would lead to an ever-decreasing bin size $s = \log(\frac{E+\Delta E}{E})$ for constant ΔE. To avoid this, it is chosen to work with the logarithmic differential event rate:

$$\frac{\mathrm{d}N}{\mathrm{d}\log E} = \frac{\mathrm{d}N}{\mathrm{d}E} \cdot \frac{\mathrm{d}E}{\mathrm{d}\log E} = 2\pi T\, N_N\, \Phi(E)\, \sigma(E) \cdot E \ln(10) \tag{7.15}$$

which also will simplify further calculations (see section 7.3). The event rate per bin of constant width $s = \Delta \log E = \log E_2 - \log E_1 = \log(E_2/E_1)$ is then given by

$$N(E) = \int\limits_{\log E_1}^{\log E_2} \frac{\mathrm{d}N}{\mathrm{d}\log E}\,\mathrm{d}\log E \tag{7.16}$$

with

$$\log E_1 = \log E - \frac{\Delta \log E}{2}, \qquad \log E_2 = \log E + \frac{\Delta \log E}{2}, \tag{7.17}$$

so that $E = \sqrt{E_1 E_2}$ is the geometric mean of E_1 and E_2. To derive the expected event number per energy bin from the differential event rate, one can approximate the integral in equation (7.16). For a small bin size $s = \Delta \log E$, so that the differential event rate does not vary much over the region of a bin, the integral roughly yields

$$N(E) = \int\limits_{\log E_1}^{\log E_2} \frac{\mathrm{d}N}{\mathrm{d}\log E}\,\mathrm{d}\log E \approx \frac{\mathrm{d}N}{\mathrm{d}\log E} \cdot \Delta \log E, \tag{7.18}$$

so that, for example, a differential event rate of $\mathrm{d}N/\mathrm{d}\log E = 10$ gives 0.1 events per energy bin of size $s = \Delta \log E = 0.01$. If the differential event rate would be constant over one order of magnitude then its value would correspond to the actual event number occurring within that energy decade. Due to the small peak of the Glashow resonance, the bin size has to be chosen sufficiently small to resolve the entire peak of the resonance. For the calculations done in this chapter, $s = 0.01$ is chosen. Therefore, all given cross section and flux data had to be interpolated to get to the same resolution[5].
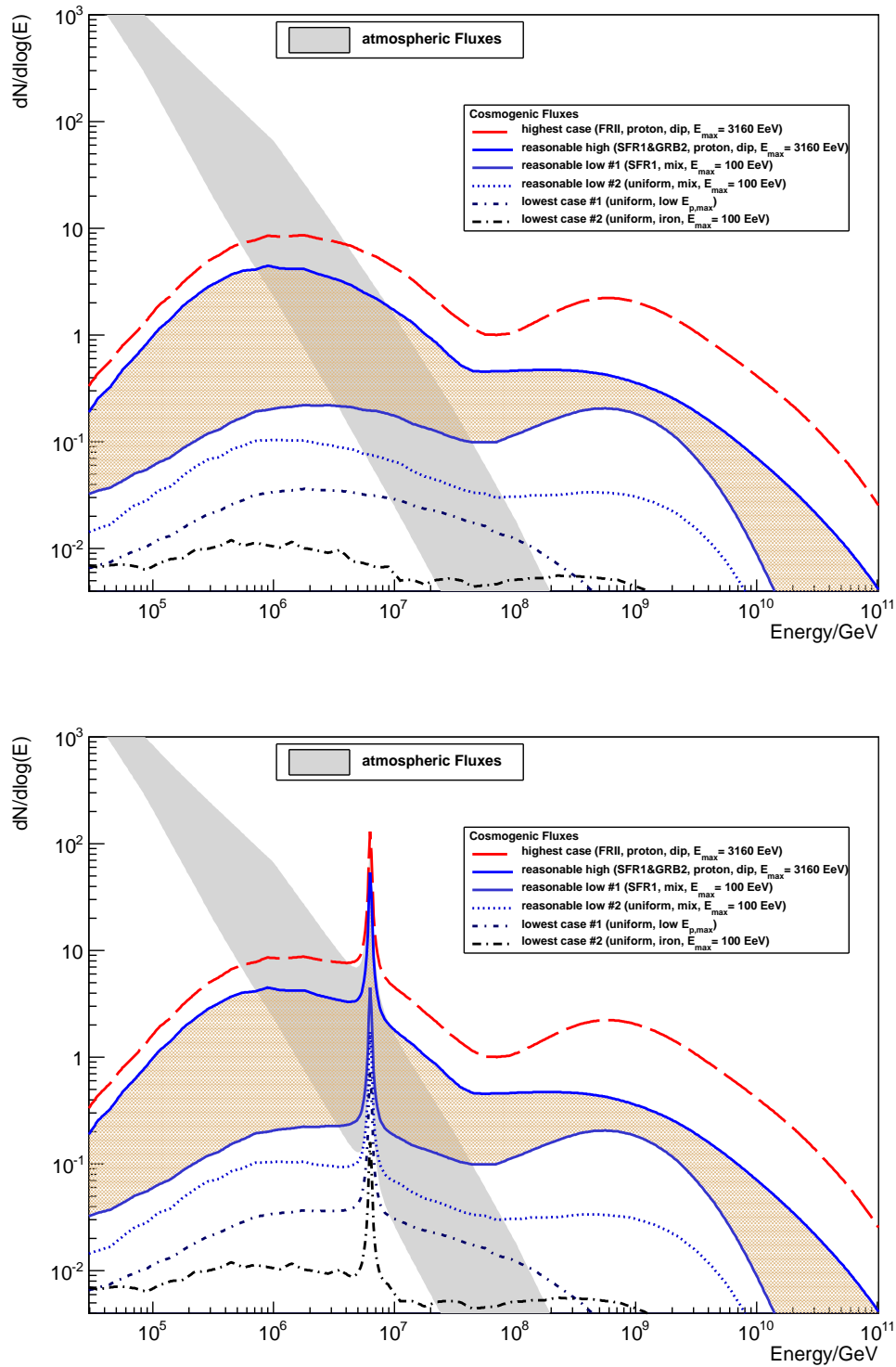
Figure 7.6: The logarithmic differential event rate for cosmogenic and atmospheric neutrinos with (top) and without (bottom) the Glashow resonance. The range of most reasonable cosmogenic models is plotted as a bright shaded area, while the range of the atmospheric models is presented as a grey shaded area. For a large part of the possible combinations of different models, the resonance peak is located in the range where the different models for the cosmogenic flux and atmospheric flux meet. This will have a high impact on the predicted event rate that can be measured for the cosmogenic neutrinos (see also Table 7.3). For which models limit the area for the atmospheric fluxes, see text to Figure 7.7.

The logarithmic differential event rates as calculated according to equation (7.15) with $T = 1$ year are plotted in Figure 7.6 for all used cosmogenic neutrino flux models together with the event rates for the atmospheric flux models. For each model the sum of all neutrino flavours is plotted. The event rates are illustrated with and without the Glashow resonance to emphasize its impact. The two bumps of the cosmogenic flux spectrum also form two bumps in the event rate spectrum. As already could be seen in the comparison of the fluxes (Figure 7.1) the energy range where the cosmogenic neutrinos start to predominate the spectrum lies at around 1 to 100 PeV. Since the peak of the Glashow resonance lies in this energy range, the resonance will highly effect the total, energy integrated event number that could be expected from the cosmogenic neutrinos while being clearly distinguishable from the atmospheric background event rate. While for high cosmogenic and low atmospheric predictions most events around the resonance peak come from cosmogenic neutrinos, the event rate in this region is predominated by atmospheric contributions for lower cosmogenic and higher atmospheric predictions. The consequences for the energy integrated event numbers, the so called cumulative event rates, are discussed in the following.

Cumulative event rate

The cumulative event rate N_C, which is an important quantity for the experiment, describes the number of events from a given energy E:

$$N_C(E) = \int_{\log E}^{\infty} \frac{dN}{d\log E} \, d\log E. \tag{7.19}$$

As mentioned in the previous section, there exists such an energy where the atmospheric background becomes negligible compared to the cosmogenic flux. Thus, with the cumulative event rate one can quantify the total number of events of cosmogenic neutrinos that can be expected in KM3NeT. The integral is here approximated by a sum, where the high resolution that has been introduced because of the small peak of the Glashow resonance is taken advantage of. Thus it can be written as

$$N_C(E) = \int_{\log E}^{\infty} \frac{dN}{d\log E}(E') \, d\log E' \tag{7.20}$$

$$\approx \Delta \log E \sum_{i=I(E)}^{N_\infty} \frac{dN}{d\log E}(E_i) \tag{7.21}$$

$$= 2\pi T \ln(10) \, \Delta \log E \sum_{i=I(E)}^{N_\infty} \Phi(E_i) \cdot A_{\text{eff}}(E_i) \cdot E_i \tag{7.22}$$

with $\Delta \log E = 0.01$ and the sum is evaluated such that E_i is the energy of the i-th data point, $I(E)$ corresponds to the data point at energy E and N_∞ is the total number of data points.

The cumulative event numbers are shown in Figure 7.7. Again it is plotted with and without the Glashow resonance. From the intersection points of the graphs of the cosmogenic numbers with the graphs of the atmospheric numbers one can get an impression of how many cosmogenic events can be expected per year in the detector volume of KM3NeT. The values for the event numbers and the corresponding energy from which cosmogenic events can be expected are summarized in Table 7.3. In the Table only the highest and lowest atmospheric model at a given energy is considered which are given as the borders of the shaded area in the plots. These limits are mainly given by the high RQPM and low pQCD prompt model. It follows that in the best cases, regarding the cosmogenic flux detection, a number of 22 events can be expected, the measurement of which would give clear evidence of its existence, while

---

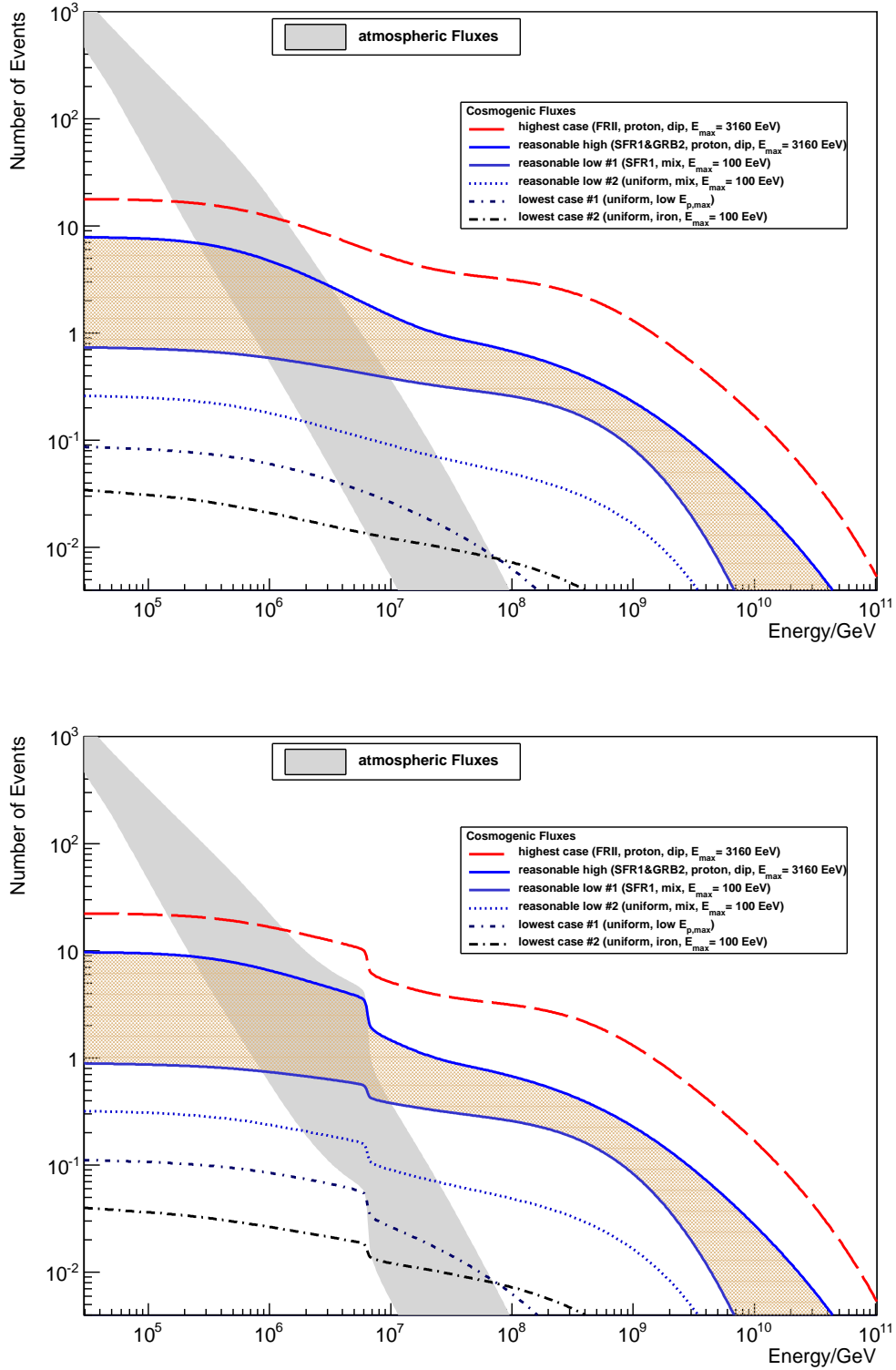[5]The cross section data was given with $s \approx 0.35$, the flux data with $s = 0.1$.

Figure 7.7: The cumulative event number per year with (bottom) and without (top) the Glashow resonance. The resonance can be seen as a step in the spectrum. The highest and lowest atmospheric flux predictions that limit the gray shaded area are, for the upper border, given by the Bartol model combined with the high RQPM prompt neutrino flux prediction, and for the lower border the Bartol model combined with the low pQCD prompt prediction. For low energies ($E \leq 55 \cdot 10^3$ GeV) the lower limit is given by the Fluka model combined with the low pQCD prediction.

Atm. model	Cosm. model	w/o Gl.		w/ Gl.	
		N_C	E / GeV	N_C	E / GeV
lowest	highest	17	$1,6 \cdot 10^5$	22	$1.4 \cdot 10^5$
	reas. high	6.9	$2.5 \cdot 10^5$	8.9	$2.3 \cdot 10^5$
	reas. low #1	0.59	$9.4 \cdot 10^5$	0.75	$8.7 \cdot 10^5$
	reas. low #2	0.15	$1.9 \cdot 10^6$	0.21	$1.9 \cdot 10^6$
	lowest #1	0.040	$3.7 \cdot 10^6$	0.052	$6.2 \cdot 10^6$
	lowest #2	0.013	$6.3 \cdot 10^6$	0.015	$7.0 \cdot 10^6$
highest	highest	11	$1.4 \cdot 10^6$	16	$1.3 \cdot 10^6$
	reas. high	2.7	$3.2 \cdot 10^6$	2.9	$6.3 \cdot 10^6$
	reas. low #1	0.38	$9.9 \cdot 10^6$	0.38	$1.0 \cdot 10^7$
	reas. low #2	0.069	$2.5 \cdot 10^7$	0.070	$2.5 \cdot 10^7$
	lowest #1	0.0085	$6.8 \cdot 10^7$	0.0085	$6.8 \cdot 10^7$
	lowest #2	0.0080	$7.0 \cdot 10^7$	0.0080	$7.0 \cdot 10^7$

Table 7.3: The expected cosmogenic neutrino event rates N_C per year for the different models. The numbers as well as the energy E are given by the intersection points in Figures 7.7. Considered are all cosmogenic neutrino flux models presented in [7] and the highest and lowest atmospheric flux model, respectively. The numbers are given with (w/) and without (w/o) the Glashow resonance, which increases the total energy integrated event number by approximately 30 % in case of the cosmogenic neutrinos. The highest number that could be expected from cosmogenic neutrinos is about 22 events per year while the lowest prediction leads to approximately 0.8 events per century. The highest atmospheric flux prediction is the Bartol model combined with the high RQPM prompt neutrino flux prediction, the lowest atmospheric flux prediction is given by the Bartol model combined with the low pQCD prompt prediction. Note that the final size of KM3NeT is planned to be roughly twice the size used in the calculations so that the event numbers would roughly double as well. For comparison, the event numbers that could be expected in ANTARES are a factor of roughly 35 smaller than those listed in the table since the can volume of ANTARES is approximately $0.17 \, \text{km}^3$.

for the lowest predictions with only 0.8 events per century, the discovery of the cosmogenic neutrinos from today's perspective would be nearly impossible in an experiment like KM3NeT. Note that the final size of KM3NeT could reach a value twice as large as used in the calculations, leading to event numbers roughly twice as large as well. In any case, a few years of measurements would put strong constraints on the parameter space of the cosmogenic neutrino flux and thus give valuable information on the characteristics of highest energy cosmic rays and their sources. For comparison, the event numbers that could be expected in ANTARES are a factor of roughly 35 smaller, thus excluding a possible detection of the cosmogenic neutrino flux by ANTARES for most predictions.

7.3   Smeared Event Rates

Because of imperfect detector characteristics, the measured energy of the neutrino events will be smeared around the actual energy deposited in the detector volume. To account for this, a simple model for the energy resolution of the detector is introduced. In this model it is assumed that for an event, the

measured or reconstructed energy spreads around the actual energy deposit in the detector following a Gaussian $g(\log E - \log E'; \sigma)$ with respect to the logarithm of the energy and with a width[6] of $\sigma = 0.3$:

$$g(\log E - \log E'; \sigma) = \frac{1}{\sqrt{2\pi\sigma^2}} \cdot \exp\left(-\frac{(\log E - \log E')^2}{2\sigma^2}\right) \tag{7.23}$$

with E being the reconstructed energy and E' being the energy deposit in the detector.

As seen in chapter 4, the energy deposit of a hadronic shower produced in neutrino events is not the energy E_ν of the interacting neutrino but rather given by the inelasticity multiplied with the neutrino energy. Only for $\nu_e N$ CC events and for resonant production of hadrons at the Glashow resonance the total energy of the neutrino is deposited as showers. Consequently, as showers are the considered signatures in this section, this has to be included in the smearing of the event rates. To account for this, a mean value of $\langle y \rangle = 0.2$ is taken for the inelasticity[7] so that for all NC events and ν_μ-, ν_τ-CC events as well as the resonant process $\bar\nu_e e^- \to \bar\nu_e e^-$ the differential event rate before smearing is shifted towards lower energies:

$$\frac{dN_{\text{dep}}}{d\log E}(E) = \frac{dN}{d\log E}(\langle y \rangle^{-1} \cdot E) = \frac{dN}{d\log E}(5 \cdot E), \tag{7.24}$$

where now E is the mean energy of the produced shower at the interaction vertex. For $\nu_e N$-CC events and the process $\bar\nu_e e^- \to q\bar q$ the deposited energy is equal to the neutrino energy:

$$\frac{dN_{\text{dep}}}{d\log E}(E) = \frac{dN}{d\log E}(E). \tag{7.25}$$

The resonant production of muons $\bar\nu_e e^- \to \bar\nu_\mu \mu^-$ and tau leptons $\bar\nu_e e^- \to \bar\nu_\tau \tau^-$ is not considered in this section as they do not leave a direct shower signature at the interaction vertex, so that for these processes:

$$\frac{dN_{\text{dep}}}{d\log E}(E) = 0. \tag{7.26}$$

The index 'dep' denotes that this corresponds to the differential event rate of events depositing the energy E in the detector.

The smeared event rate for a specific interaction channel is then given by the convolution of the differential event rate with the Gaussian:

$$\frac{dN_{\text{sm}}}{d\log E}(E) = \frac{1}{\sqrt{2\pi\sigma^2}} \cdot \int_{-\infty}^{+\infty} \frac{dN_{\text{dep}}}{d\log E}(E') \cdot e^{-\frac{(\log E - \log E')^2}{2\sigma^2}} \, d\log E'. \tag{7.27}$$

The smearing must conserve the total number of events N_{tot} such that

$$N_{\text{tot}} = \int_{-\infty}^{+\infty} \frac{dN_{\text{dep}}}{d\log E} \, d\log E \overset{!}{=} \int_{-\infty}^{+\infty} \frac{dN_{\text{sm}}}{d\log E} \, d\log E. \tag{7.28}$$

---

[6]The value of the width is taken according to studies in [33].

[7]Due to time constraints, the results for detailed $\langle y \rangle$ calculations are not included in calculations in this chapter.

A short calculation shows that this is true:

$$\int\limits_{-\infty}^{+\infty} \frac{\mathrm{d}N_{\mathrm{sm}}}{\mathrm{d}\log E}(E)\,\mathrm{d}\log E = \int\limits_{-\infty}^{+\infty} \frac{1}{\sqrt{2\pi\sigma^2}} \int\limits_{-\infty}^{+\infty} \frac{\mathrm{d}N_{\mathrm{dep}}}{\mathrm{d}\log E}(E')\,\mathrm{e}^{-\frac{(\log E - \log E')^2}{2\sigma^2}}\,\mathrm{d}\log E'\,\mathrm{d}\log E$$

$$= \int\limits_{-\infty}^{+\infty} \frac{1}{\sqrt{2\pi\sigma^2}} \frac{\mathrm{d}N_{\mathrm{dep}}}{\mathrm{d}\log E}(E') \underbrace{\int\limits_{-\infty}^{+\infty} \mathrm{e}^{-\frac{(\log E - \log E')^2}{2\sigma^2}}\,\mathrm{d}\log E}_{= \int\limits_{-\infty}^{+\infty} \mathrm{e}^{-\frac{(x-x')^2}{2\sigma^2}}\,\mathrm{d}x = \sqrt{2\pi\sigma^2}}\,\mathrm{d}\log E'$$

$$= \int\limits_{-\infty}^{+\infty} \frac{\mathrm{d}N_{\mathrm{dep}}}{\mathrm{d}\log E}(E')\,\mathrm{d}\log E'$$

The evaluation of the integral is again done by approximating it as a sum:

$$\frac{\mathrm{d}N_{\mathrm{sm}}}{\mathrm{d}\log E}(E_i) \approx \frac{1}{\sqrt{2\pi\sigma^2}}\,\Delta\log E \sum_{j=-N_{4\sigma}(E_i)}^{+N_{4\sigma}(E_i)} \frac{\mathrm{d}N_{\mathrm{dep}}}{\mathrm{d}\log E}(E_j)\cdot\mathrm{e}^{-\frac{\left(\log E_i - \log E_j\right)^2}{2\sigma^2}} \tag{7.29}$$

where the sum goes from $-N_{4\sigma}$ to $+N_{4\sigma}$, the numbers that corresponds to the energy where the Gaussian becomes small enough, $g(\pm 4\sigma\,;\sigma)/g(0\,;\sigma) = 3.4\cdot 10^{-4}$, such that the contribution from energies outside that region is negligible.

The smeared differential event rate for all models is shown in Figure 7.8. The strong peak of the Glashow resonance is smoothed out together with the whole spectrum, which is in large parts shifted towards lower energies. Still it is noticeable how the Glashow resonance enlarges the intersection area of cosmogenic models with atmospheric background models. Consequently the total expected event rate highly depends on the considered model.

Cumulative smeared event rate

In the same way as for the non-smeared event rates, the calculation of the cumulative event rate is done for the smeared differential event rates so that we get the smeared cumulative event rate:

$$N_{\mathrm{sm},C}(E) = \int\limits_{\log E}^{\infty} \frac{\mathrm{d}N_{\mathrm{sm}}}{\mathrm{d}\log E}(E')\,\mathrm{d}\log E' \tag{7.30}$$

$$\approx \Delta\log E \sum_{i=I(E)}^{N_\infty} \frac{\mathrm{d}N_{\mathrm{sm}}}{\mathrm{d}\log E}(E_i) \tag{7.31}$$

The smeared cumulative event rate is shown in Figure 7.9. Again, the intersection points of the graphs of the cosmogenic numbers with the graphs of the atmospheric numbers give an approximation to the cosmogenic event number that can be expected per year in KM3NeT. The values for these numbers for the smeared event rates and the corresponding energy are summarized in Table 7.4. As above, only the highest and lowest atmospheric model at a given energy is considered in the table. Compared to the non-smeared events the expected event rate decreases, due to the fact that after smearing, the atmospheric background, which is very high for lower energies, covers a wider range. In the best cases, regarding the cosmogenic flux detection, a number of 19 events can now be expected while the lowest predictions lead to roughly 0.6 events per century. Still the KM3NeT experiment will be able to give essential input to the open questions about the cosmic rays and their high energy parameter space, considering also the fact that KM3NeT probably will be larger than the size used for the calculations.
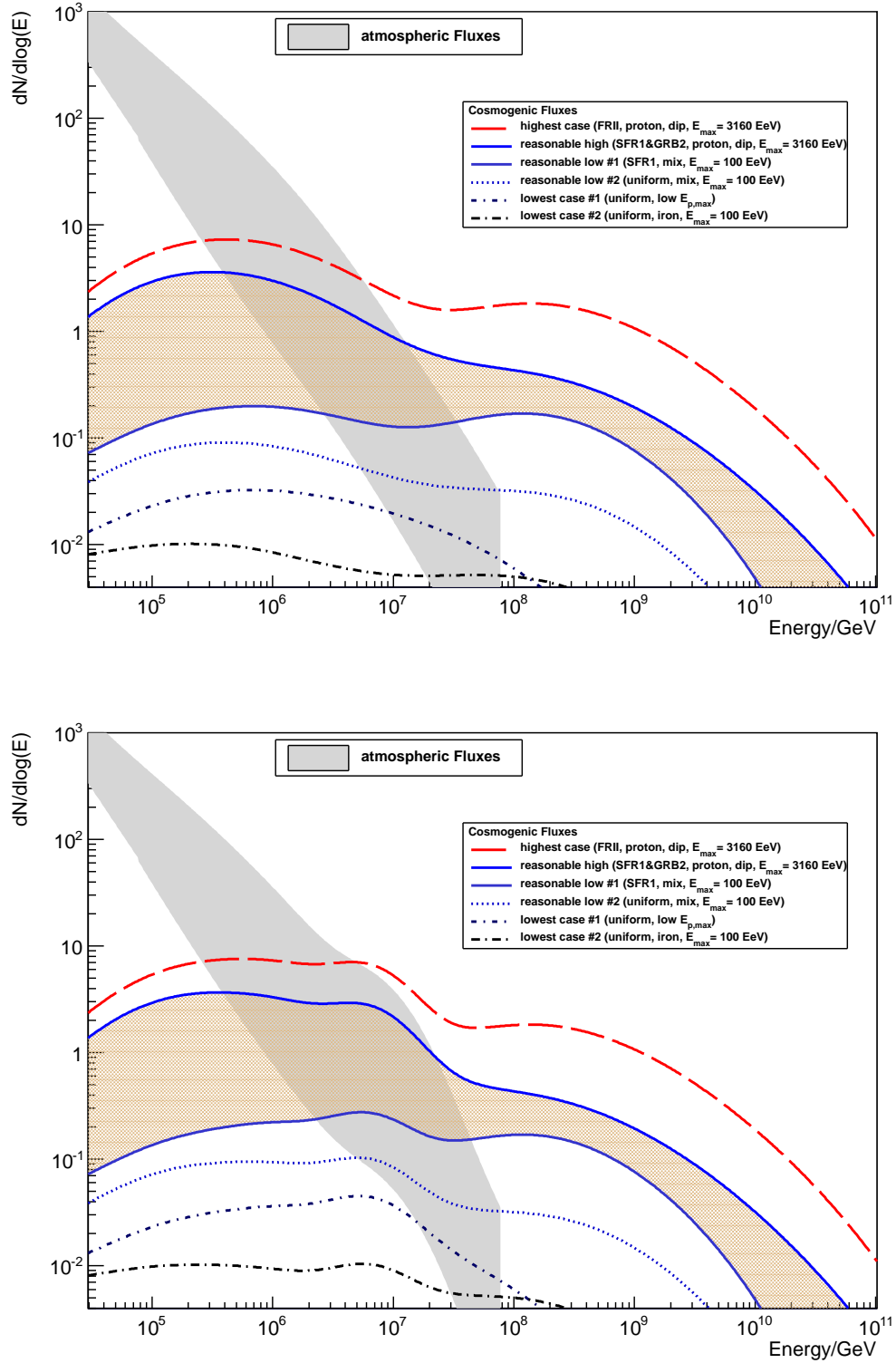
Figure 7.8: The smeared logarithmic differential event rate with (bottom) and without (top) the Glashow resonance. Compared to the non-smeared event rates, the whole spectrum is shifted towards lower energies (see also section 7.4). The Glashow resonance smears out giving a small bump at 6.3 PeV. The cut of the atmospheric spectrum at approximately $10^{7.8}$ GeV is explained by the fact that atmospheric predictions are only given up to $\approx 10^9$ GeV and that the smearing is done for a range of $4\sigma = 1.2$ in $\log E$, so that for $E > 10^{7.8}$ GeV the smearing cannot be done properly.
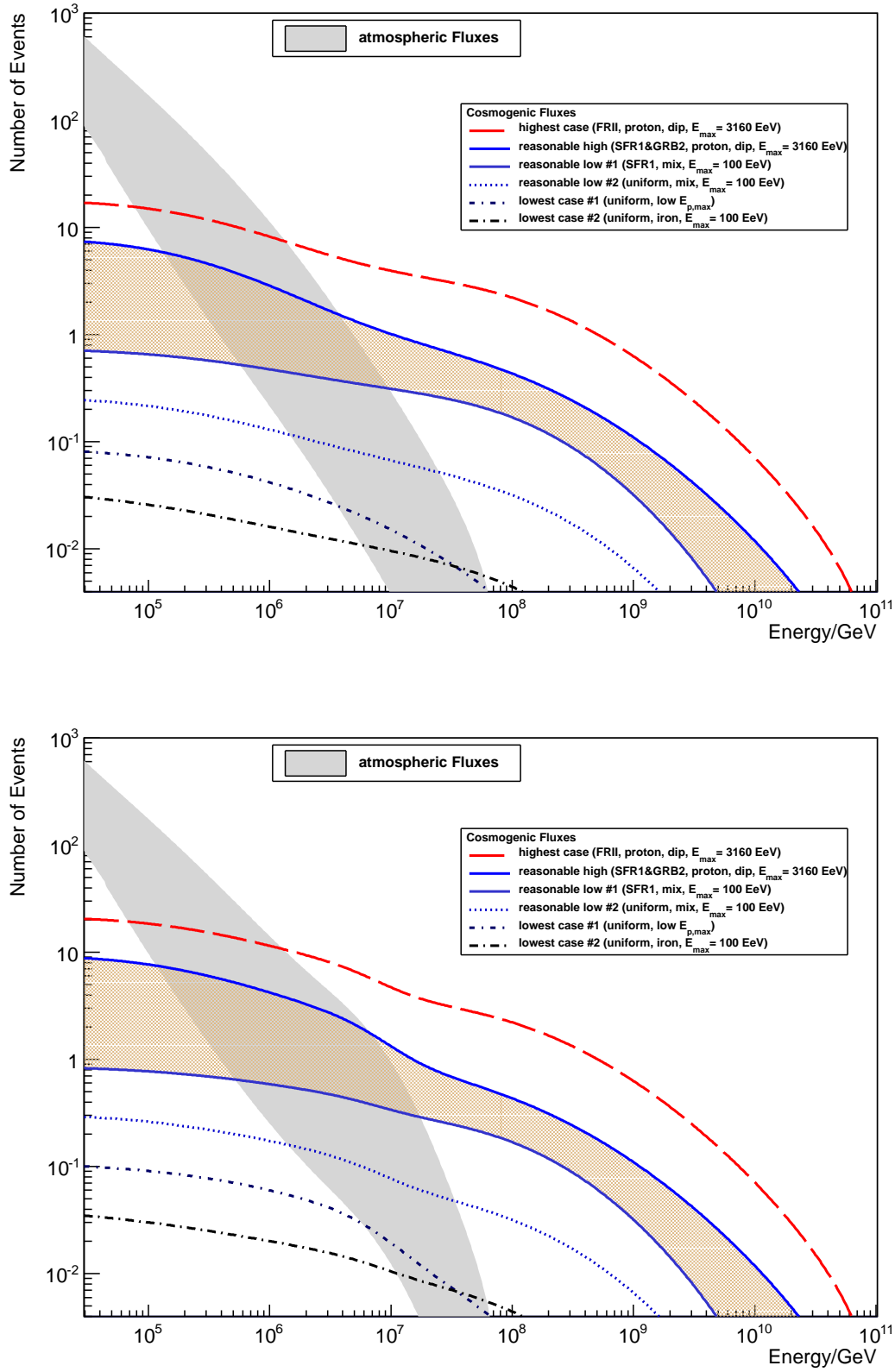
Figure 7.9: The cumulative smeared event rate per year with (bottom) and without (top) the Glashow resonance. Like in the preceding figures, the range of the most likely cosmogenic models is presented as a bright shaded area. See text for more.

Atm. model	Cosm. model	w/o Gl.		w/ Gl.	
		$N_{\text{sm},C}$	E / GeV	$N_{\text{sm},C}$	E / GeV
lowest	highest	16	$7,7 \cdot 10^4$	19	$6.8 \cdot 10^4$
	reas. high	5.9	$1.3 \cdot 10^5$	7.5	$1.2 \cdot 10^5$
	reas. low #1	0.52	$5.7 \cdot 10^5$	0.65	$5.2 \cdot 10^5$
	reas. low #2	0.12	$1.5 \cdot 10^6$	0.16	$1.4 \cdot 10^6$
	lowest #1	0.026	$3.6 \cdot 10^6$	0.029	$5.8 \cdot 10^6$
	lowest #2	0.011	$5.7 \cdot 10^6$	0.010	$1.1 \cdot 10^7$
highest	highest	7.3	$1.4 \cdot 10^6$	11	$1.3 \cdot 10^6$
	reas. high	1.5	$3.8 \cdot 10^6$	1.7	$6.9 \cdot 10^6$
	reas. low #1	0.32	$9.5 \cdot 10^6$	0.29	$1.8 \cdot 10^7$
	reas. low #2	0.052	$2.5 \cdot 10^7$	0.047	$3.4 \cdot 10^7$
	lowest #1	0.0043	$6.2 \cdot 10^7$	0.0040	$6.5 \cdot 10^7$
	lowest #2	0.0056	$5.8 \cdot 10^7$	0.0055	$6.2 \cdot 10^7$

Table 7.4: The expected smeared event rates $N_{\text{sm},C}$ per year for the different cosmogenic and atmospheric models with (w/) and without (w/o) the Glashow resonance. The numbers as well as the energy E are given by the intersection points in Figures 7.9. Depending on the energy a different fraction of events occurring due to the Glashow resonance contributes to the total event rate. In the most beneficial case, the Glashow resonance increases the expected event rate by roughly 24 %. Again, note that for the planned final size of KM3NeT the event numbers would roughly be twice as large.

7.4 All neutrino flavour considerations

This section will give an impression of how the different event rate spectra are formed by the contribution of the different neutrino flavours. Especially for the smeared event rate, where only shower events are considered and the inelasticity has to be taken into account, this is informative. The differential event rate is calculated with C++ code, which was kept very generic. Therefore, any change in predictions or any future models can easily be included in the calculations, be it for a specific kind of neutrino or the sum of all neutrino flavours. This has the advantage that for example just the muon neutrino charged current events, which produce long muon tracks, or events originating from electron antineutrinos, which include the Glashow resonance, can be calculated.

It should be recalled that due to neutrino oscillation the proportion of each neutrino flavour in the cosmogenic neutrino flux is the same, while for the atmospheric flux the amount of tau neutrinos is negligible and the ratio of electron neutrinos to muon neutrinos is a function of the energy and also depends on the different models (see also Figure 3.9). This will also affect the height of the Glashow resonance in the atmospheric spectrum as will be shown in some of the following figures.

Figures 7.10 and 7.11 present the different types of event rates for the cosmogenic and atmospheric neutrinos separately for all neutrino flavours with and without the Glashow resonance. Shown is the range of reasonable cosmogenic models and the total range of atmospheric models. For the non-smeared events, the cosmogenic contributions for all neutrino flavours are identical while for the smeared events, the muon and tau neutrino contributions are shifted towards lower energies according to equation 7.24. The electron neutrino events, therefore, contribute a bigger part to the smeared event rate spectrum at higher energies, i.e. the spectrum at these energies is to a large part influenced by the number of electron neutrinos present in the cosmogenic flux. Additionally, the bumps in the cosmogenic spectrum formed by the electron neutrino contribution are broader, compared to those formed by the other flavours, due to

the fact that only electron neutrino NC events are shifted towards lower energies, while electron neutrino CC events are not (see also below). The contribution from the Glashow resonance only affects the electron antineutrino events and can always be seen as an essential rise in the event rate contribution from electron neutrinos. For more detailed illustrations of the effect of the Glashow resonance, see also Figures 7.14 to 7.17. In the non-smeared atmospheric spectra can be seen that for low prompt predictions, the electron contribution is smaller than the muon neutrino contribution, while for high prompt predictions from $\approx 10^6$ GeV both contributions are the same. In contrast, the smeared shower event spectra for the atmospheric neutrinos is predominated by electron neutrino contributions due to the shift of muon neutrino contributions towards lower energies.

Figures 7.12 and 7.13 show the event rate spectra separately for all neutrino flavours and interaction types, including NC and CC events and the Glashow resonance, together with the total event rate spectrum, which is formed by the aforementioned ones. These spectra are shown for the 'high, reasonable' cosmogenic neutrino flux prediction (for the terminology see legend to figures in section 7.2 and 7.3). While each spectrum is the same for all neutrino flavour NC events and lower than the CC event spectra, one can again see the shift towards lower energies for all νN event types but the $\nu_e N$ CC events in the smeared spectra. Due to the smearing, the Glashow resonance forms two bumps in the differential event rate spectrum: a little one which results from the process $\bar{\nu}_e e^- \to \bar{\nu}_e e^-$ and is thus shifted towards lower energies, and a big one which follows from the process $\bar{\nu}_e e^- \to q\bar{q}$. In the cumulative event rate spectra can be seen that the cumulative event rate at $E \approx 10^5$ GeV resulting from the Glashow resonance is approximately equal to those resulting from charged current DIS events of one neutrino flavour.

Figure 7.14 and 7.15 present the effect of the Glashow resonance in detail by showing only the electron neutrino contributions for the reasonable cosmogenic range of models and the atmospheric models. The contribution from the Glashow resonance is also shown separately. In the differential event rate spectrum can be seen that the Glashow resonance peak forms two bumps after smearing which, as mentioned above, result from the different energy deposit in the detector for the different reaction channels. A smaller one shifted to the energy $E = \langle y \rangle E_{\text{res}} = 0.2 \cdot 6.3 \,\text{PeV} = 1.26 \,\text{PeV} \approx 10^{6.1}$ GeV resulting from the process $\bar{\nu}_e e^- \to \bar{\nu}_e e^-$ and a higher bump at $E = E_{\text{res}} = 6.3 \,\text{PeV}$ following from the resonant quark production $\bar{\nu}_e e^- \to q\bar{q}$. The latter bump is roughly seven times higher than the smaller one, since roughly 70 % of the Glashow resonance processes produce the hadronic shower and only about 10 % result into an $\bar{\nu}_e$ and e^-. The bump at $E = 6.3 \,\text{PeV}$ is substantially higher than the DIS event rate of electron neutrinos, resulting in a rise of electron neutrino events by a factor of more than 2 around $E = 6.3 \,\text{PeV}$ in the smeared event rate spectrum.

Figures 7.16 and 7.17 present a closer look on the event rates for different conventional atmospheric models combined with a high (high RQPM) and a low (low pQCD) prompt prediction around the Glashow resonance energy. From the resonance peak for the low pQCD model in the non-smeared differential event rates can be seen that the electron antineutrino component is completely determined by the prompt model since the absolute height of the peak is independent of the conventional atmospheric models. On the other hand, for the high prompt model at these energies both the electron and muon neutrino component is fixed by that prompt model as the event rate over the whole shown energy region is independent of the conventional model. Apart from the resonance, the conventional models differ for low prompt models meaning that the muon neutrino component in that case is still in a large extent determined by the conventional model.

The considerations done here make clear how different neutrino flavour contributions affect the total cascade event rate spectrum after smearing. Therefore, any possible changes in predictions of neutrino flavour ratios for regardless of which kind of neutrino flux can be translated in the respective cascade event rate spectrum considering the approximations that have been done in this chapter.
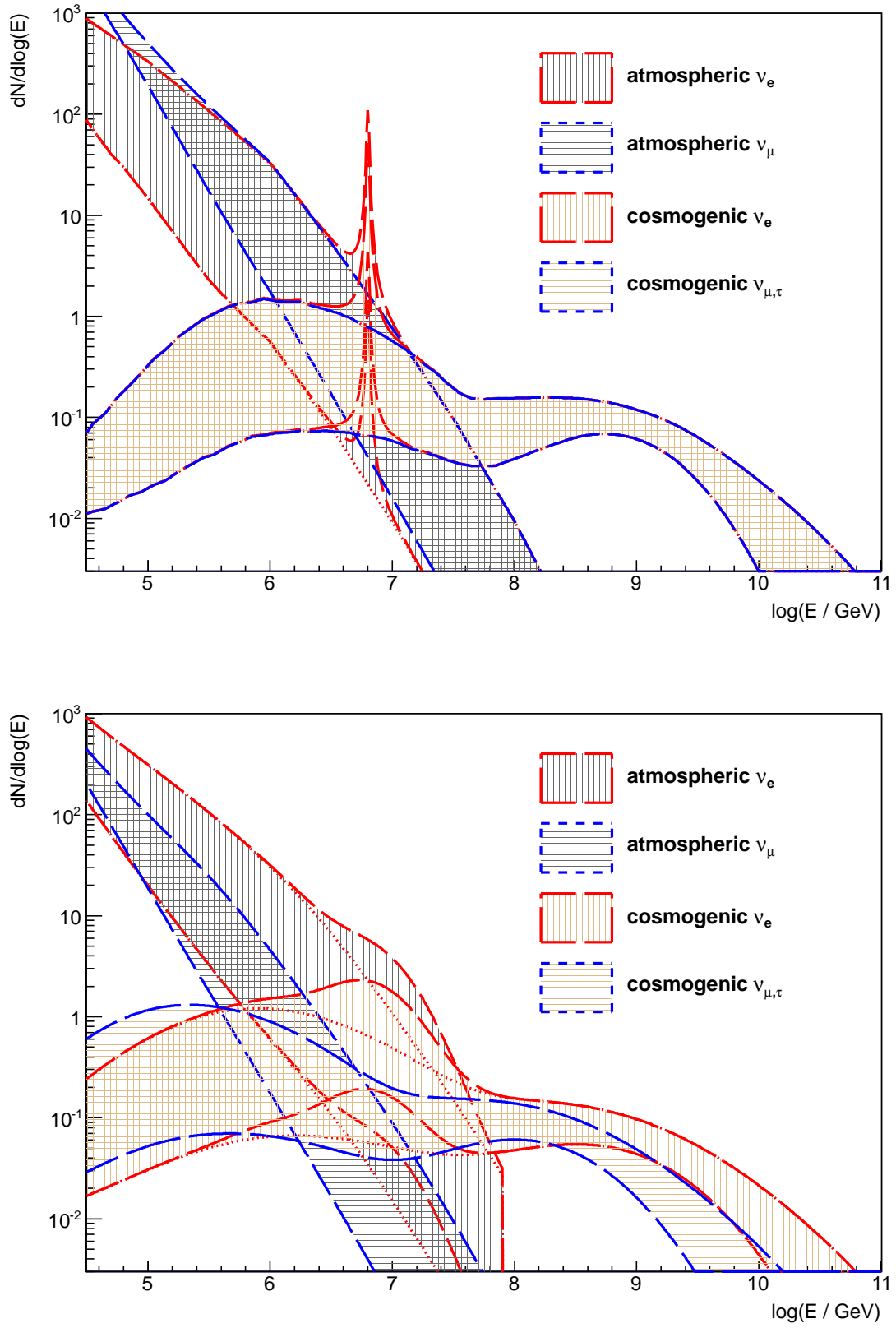
Figure 7.10: The non-smeared (top) and smeared (bottom) differential event rate spectra for shower events for all neutrino flavours. Electron neutrino contributions framed in red, other neutrino flavour contributions framed in blue (ν_μ for atmospheric, $\nu_{\mu,\tau}$ for cosmogenic). The reasonable cosmogenic models are presented (brightly dashed) with the atmospheric models (dark dashed) (see also Figure 7.11). See text for more.
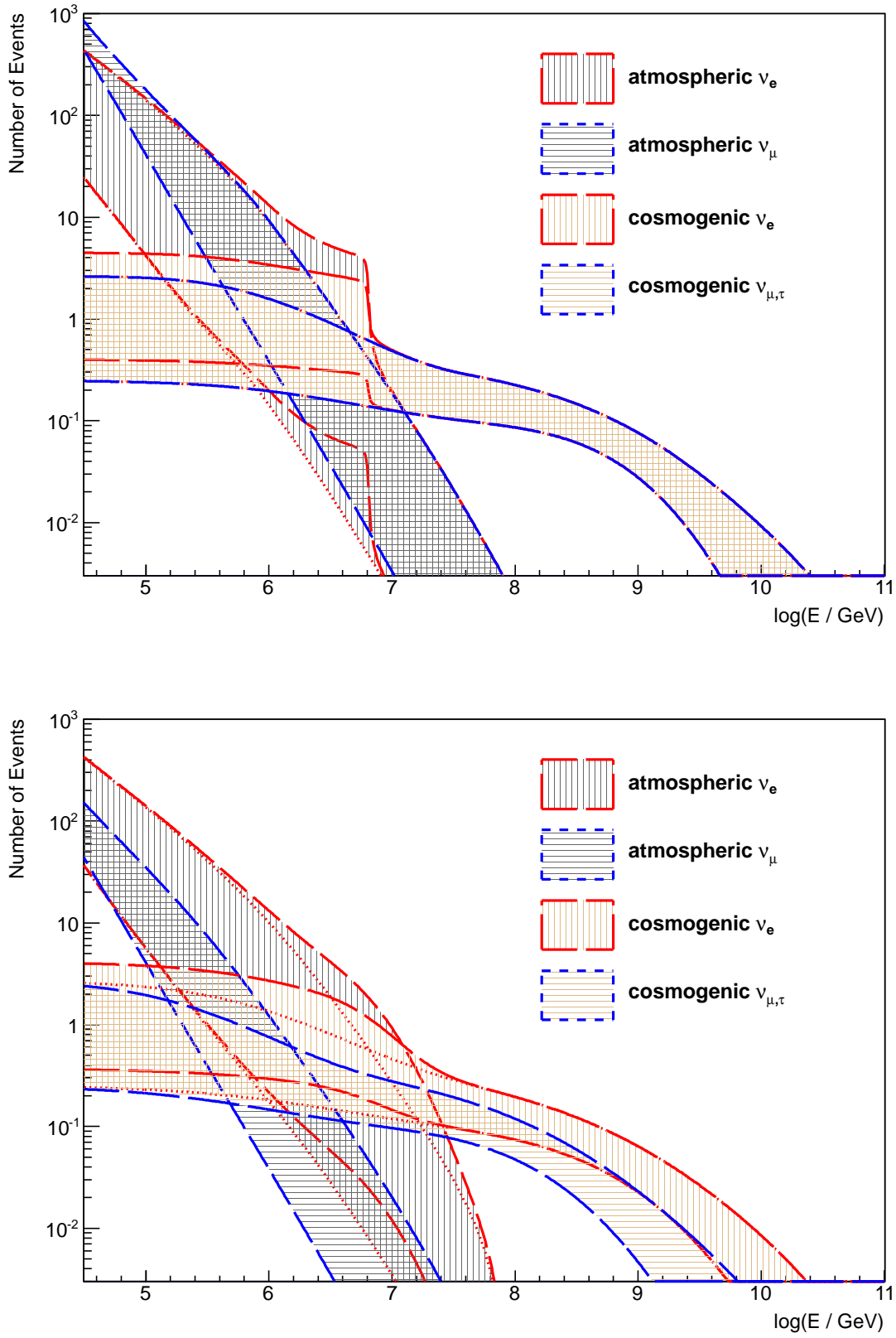
Figure 7.11: The non-smeared (top) and smeared (bottom) cumulative shower event rate spectra for all neutrino flavours. See Figure 7.10 for the corresponding differential event rates. See text for more.
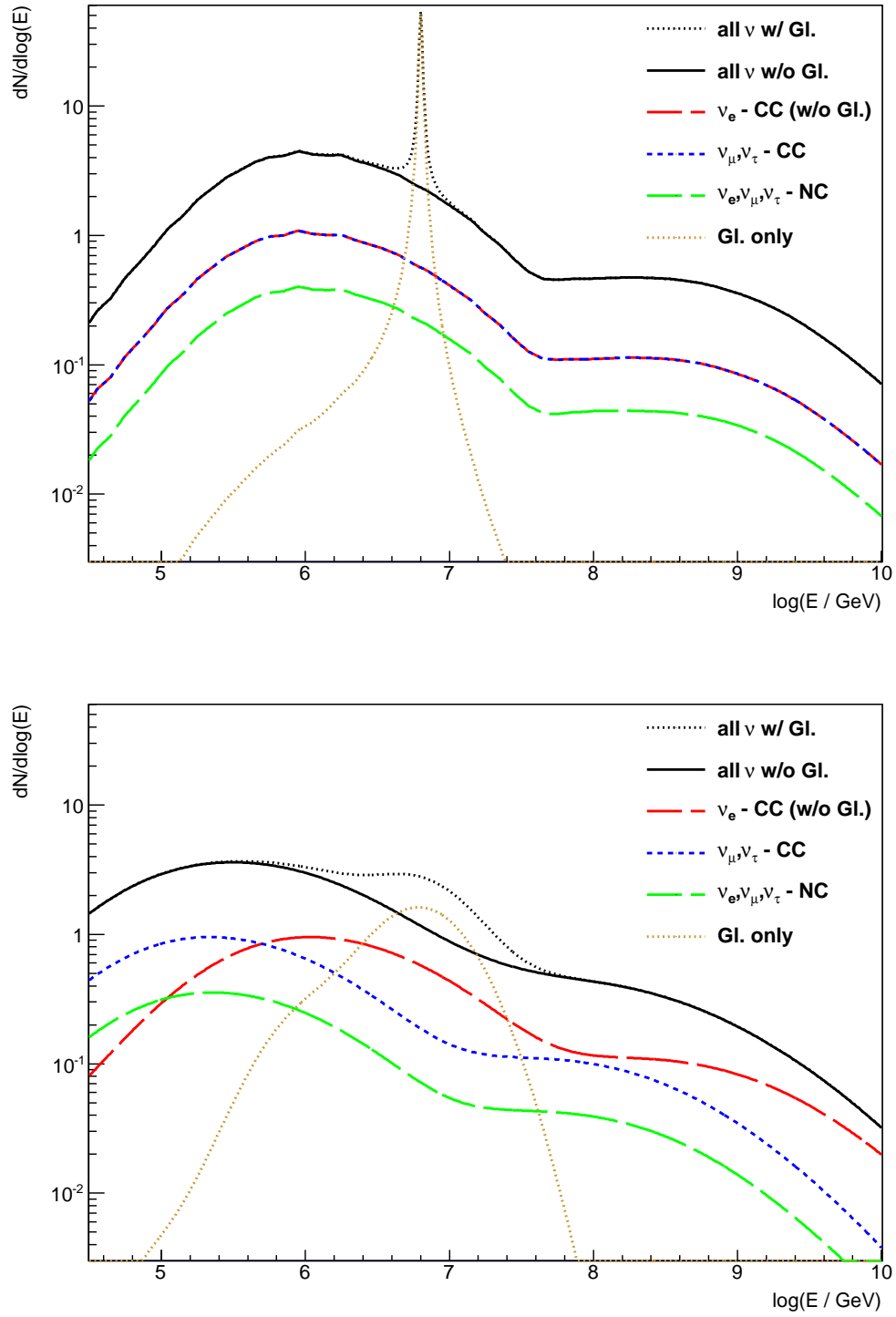
Figure 7.12: The non-smeared (top) and smeared (bottom) differential event rate spectrum for the 'high, reasonable' cosmogenic neutrino flux prediction together with its contributions from all neutrino flavours and interaction types. See Figure 7.13 for the cumulative event rates. Total event rate (black dotted), total event rate without Glashow resonance (black), ν_e CC (red), $\nu_{\mu,\tau}$ CC (blue), $\nu_{e,\mu,\tau}$ NC (green), and $\nu_e e^-$ events (dotted). See text for more.
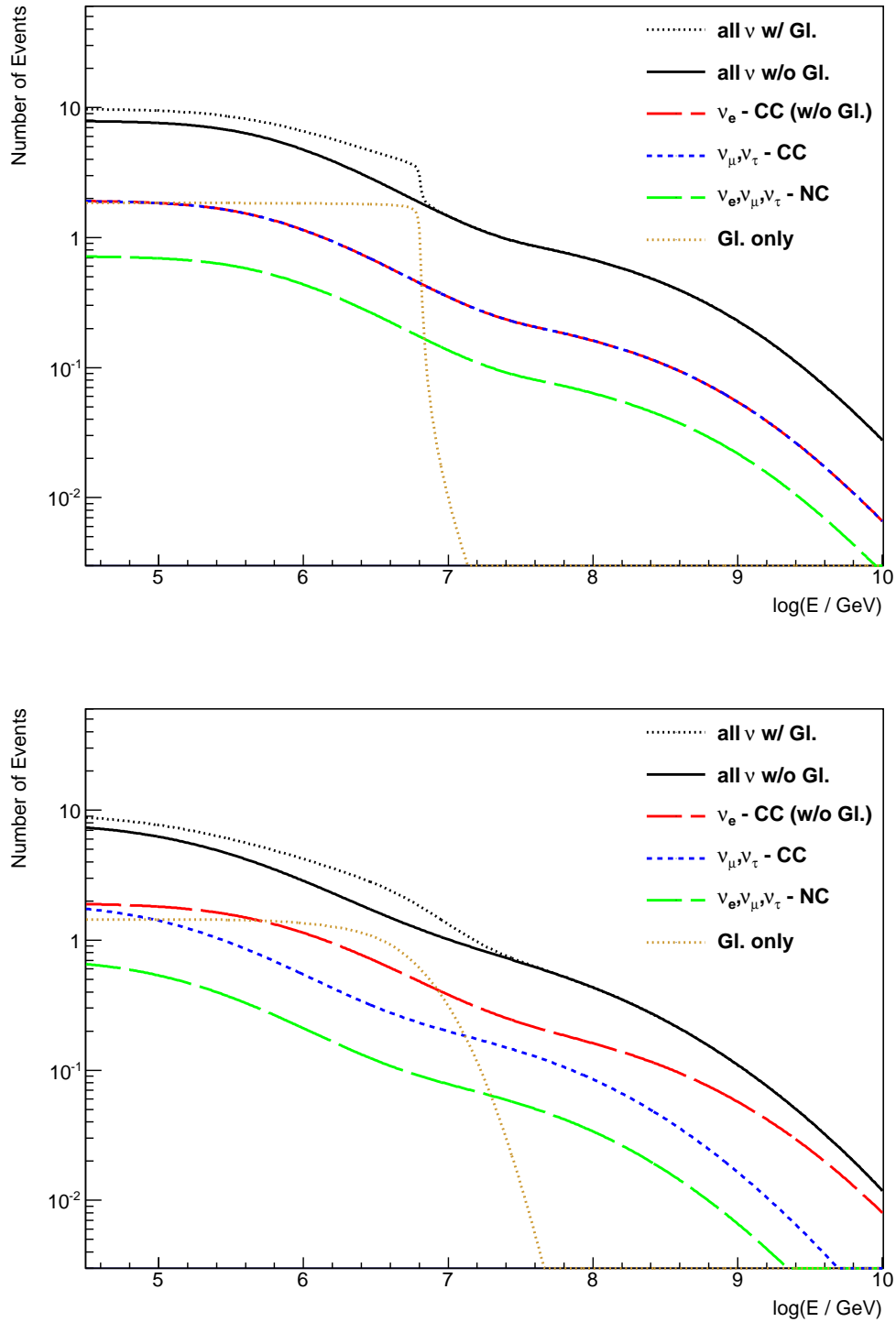
Figure 7.13: The non-smeared (top) and smeared (bottom) cumulative event rate spectrum for the 'high, reasonable' cosmogenic neutrino flux prediction' together with its contributions from all neutrino flavours and interaction types. See Figure 7.12 for the differential event rates. See text for more.
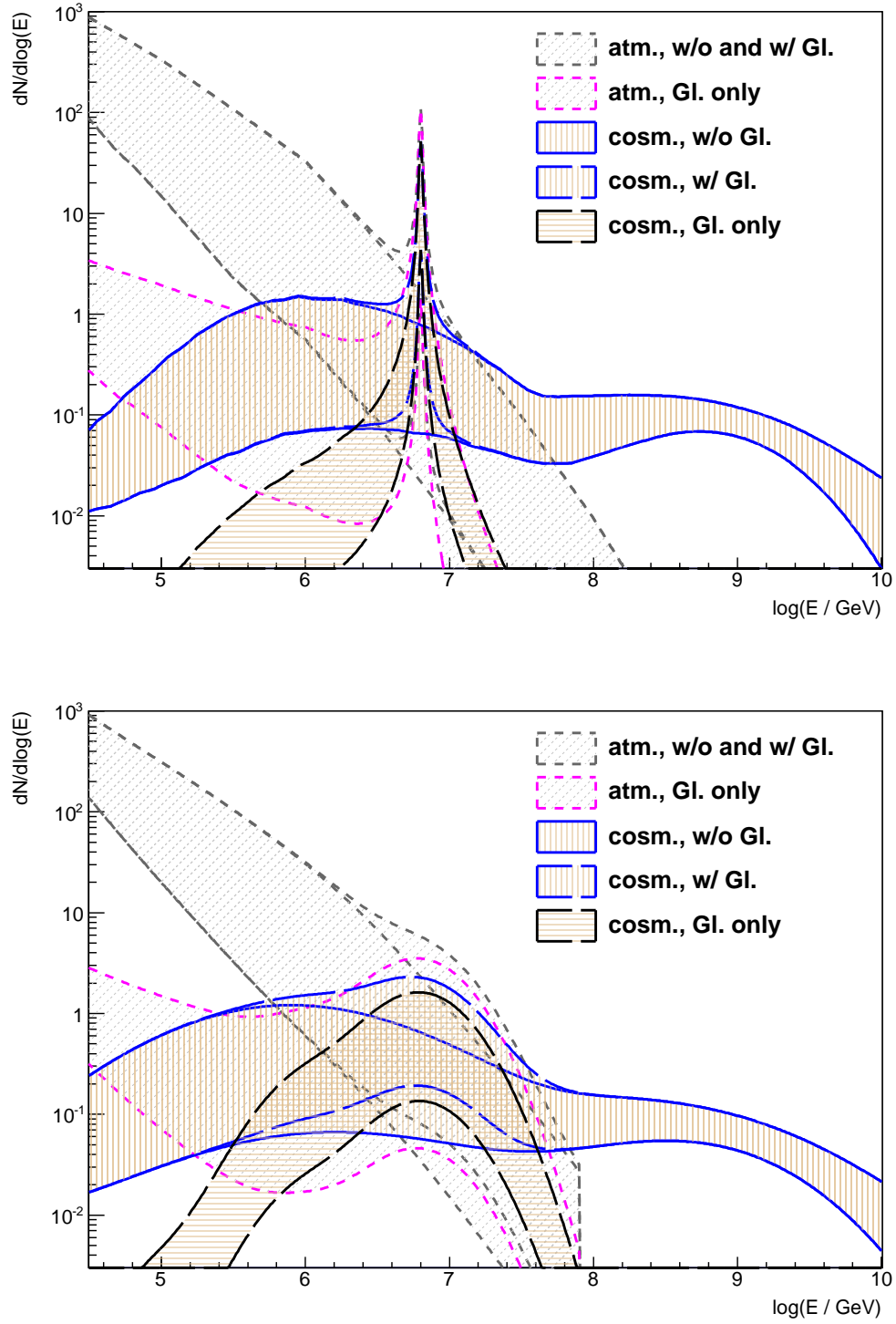
Figure 7.14: The non-smeared (top) and smeared (bottom) differential event rates for the atmospheric models and the reasonable cosmogenic models resulting from electron neutrinos with and without Glashow resonance (blue lines and brightly dashed area for cosmogenic, gray dashed line and area for atmospheric) and those resulting from the Glashow resonance only (black dashed line for cosmogenic, pink dashed line for atmospheric). See Figure 7.15 for the cumulative event rates. See text for more.
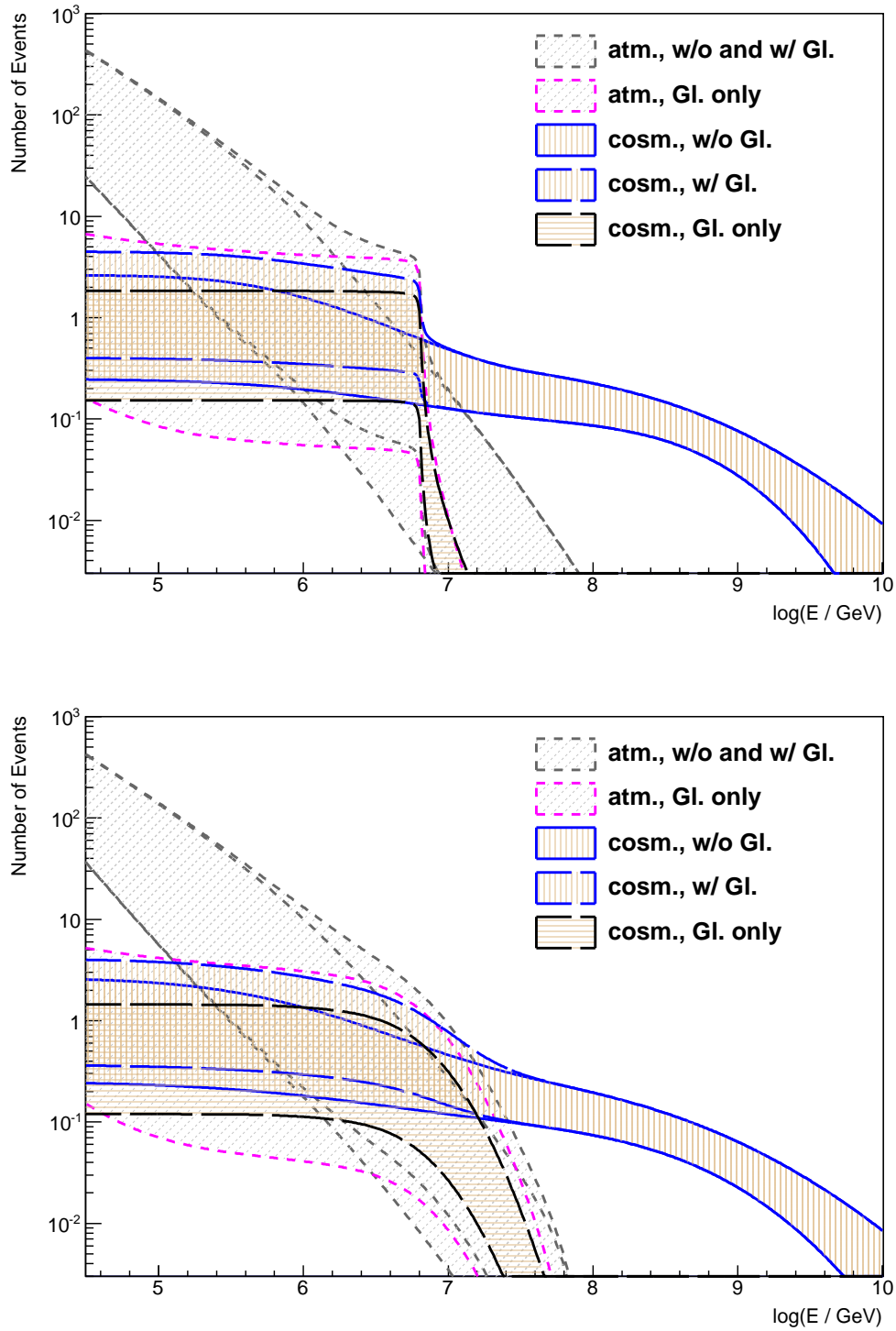
Figure 7.15: The non-smeared (top) and smeared (bottom) cumulative event rates for the atmospheric models and the reasonable cosmogenic models resulting from electron neutrinos with and without Glashow resonance (blue lines and brightly dashed area for cosmogenic, gray dashed line and area for atmospheric) and those resulting from the Glashow resonance only (black dashed line for cosmogenic, pink dashed line for atmospheric). See Figure 7.14 for the differential event rates. See text for more.
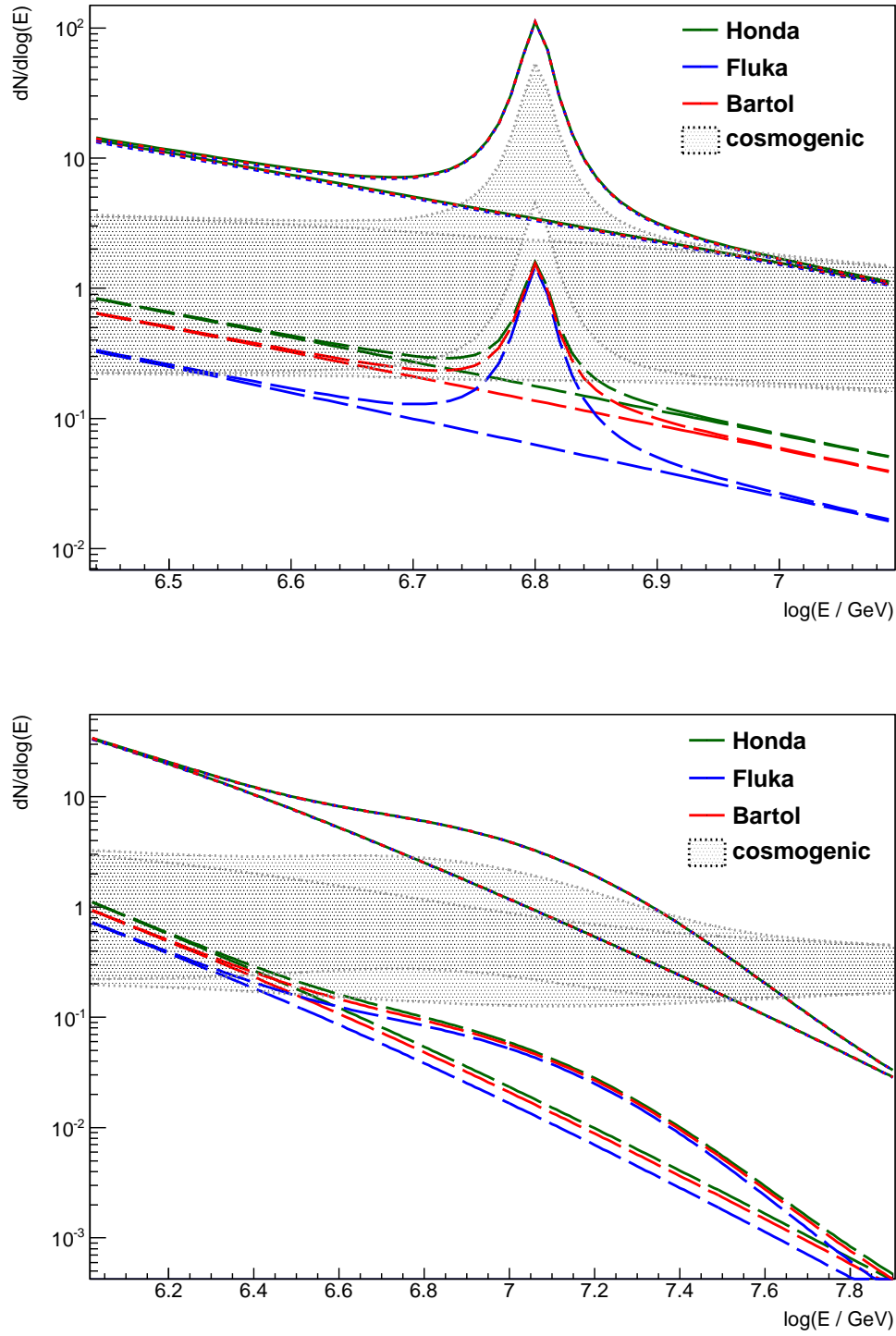
Figure 7.16: The non-smeared (top) and smeared (bottom) differential event rate with and without the Glashow resonance around the resonance energy for three atmospheric flux models, Honda (green), Fluka (blue), Bartol (red), combined with two prompt predictions. The lower prompt model is 'low pQCD', the higher model is 'high RQPM'. The range of reasonable cosmogenic models in this energy region is plotted as a gray shaded area. See Figure 7.17 for the cumulative event rates. See text for more.
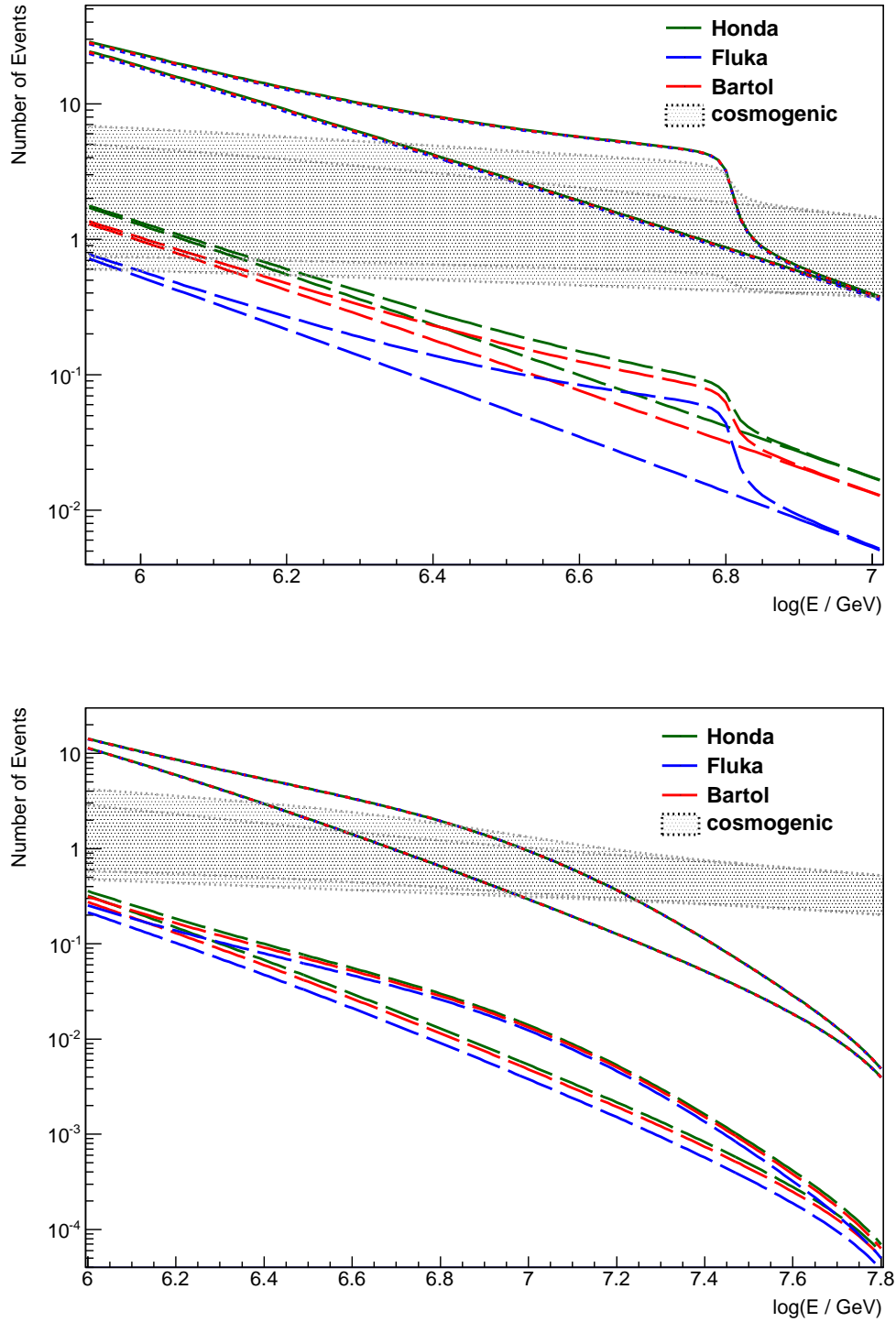
Figure 7.17: The non-smeared (top) and smeared (bottom) cumulative event rate with and without the Glashow resonance around the resonance energy for three atmospheric flux models, Honda (green), Fluka (blue), Bartol (red), combined with two prompt predictions. The lower prompt model is 'low pQCD', the higher model is 'high RQPM'. The range of reasonable cosmogenic models in this energy region is plotted as a gray shaded area. See Figure 7.16 for the differential event rates. See text for more.

Chapter 8

Summary and Outlook

The cosmogenic neutrino flux possesses valuable information on the characteristics of ultra high energy cosmic rays (UHECR). In this work, it was investigated the potential to detect cosmogenic neutrinos with the future deep-sea neutrino telescope KM3NeT. This was done by approximating the event rates of various cosmogenic neutrino flux models. For an exact event rate prediction, detailed event simulations have to be performed. It was shown that present ANTARES/KM3NeT software tools are not yet capable of doing that. Therefore, a perfect detection efficiency was assumed for the event rate calculation. It could be shown, that in this case and for very high cosmogenic models, the expected event rate, depending on the actual design of KM3NeT, can reach a few tens up to approximately 40 events per year considering the largest possible KM3NeT design. Reasonable cosmogenic flux models result in approximately 0.3 to nearly 10 detectable events per year, considering an instrumented volume of roughly $3\,\mathrm{km}^3$. The latter event rates account for the irreducible atmospheric background and the energy smearing of the events due to imperfect detector characteristics. Therefore, all of these events will at least deposit an energy of roughly $10^5\,\mathrm{GeV}$ in the detector. In any case, no matter if or how many events originating from cosmogenic neutrinos KM3NeT will measure, strong constraints can be given on the parameter space of UHECR after several years of measurement.

In this work, the effect of the Glashow resonance, peaked at $6.3\,\mathrm{PeV}$, has been investigated. It is an increase of the event rates, generated by electron antineutrinos, compared to standard high energy neutrino nucleon interaction. The number of events resulting solely from the Glashow resonance is comparable to the number of events generated by charged current interactions of one neutrino flavour in the cosmogenic flux over the whole high energy spectrum (from $10^5\,\mathrm{GeV}$). Recently, two neutrino initiated cascade events with energies of order 1 to $10\,\mathrm{PeV}$ have been reported by the IceCube collaboration. Barger et al. [65] proposed an interpretation of these two neutrino events. They conjecture that both events result from the Glashow resonance. This would have significant physics implications for cosmic neutrinos and their detection. For instance, this discovery presents an opportunity for KM3NeT to focus on cascade detection in its design, which is not yet fixed. Furthermore, if the IceCube PeV showers are electron antineutrino Glashow resonance events, then higher energy muon neutrino events should also be detected in the future.

As mentioned above, precise event rate predictions for the cosmogenic neutrino flux in KM3NeT will have to take into account the detection efficiency to ultra high energy (UHE) events. First considerations to approximate this quantity have been performed, with the result that probably 75 % to 85 % of the calculated number of shower events could be detectable. Nevertheless, future work considering cosmogenic event rate predictions will have to focus on complete simulations of contained events to quantify the trigger and reconstruction efficiency of the detector and to get an impression of the quality of the energy reconstruction of the contained events. It has been pointed out in this work, how the different neutrino flavours will influence the total shower event rate spectrum with a given energy resolution. The spectrum in the relevant energies (from roughly $1\,\mathrm{PeV}$) is therefore to a large part influenced by the ratio

of electron neutrinos, due to the fact that most electron neutrino interactions deposit the entire neutrino energy in the detector. Furthermore, to get a complete and final analysis of the cosmogenic neutrino flux, full detector simulations for UHE events with track-like signature, i.e. events where a muon or tau is produced, are necessary. With the results of such simulations, it will also be possible to calculate a precise and model independent differential sensitivity and the discovery potential of KM3NeT to UHE neutrino fluxes. Definitely, there is a lot of exciting work to do and ever interesting physics to be discovered.

List of Figures

List of Tables

Bibliography

[1] J. Abraham et al. Observation of the suppression of the flux of cosmic rays above 4×10^{19}eV. *Phys.Rev.Lett.*, 101:061101, 2008.

[2] Kenneth Greisen. End to the cosmic ray spectrum? *Phys.Rev.Lett.*, 16:748–750, 1966.

[3] G.T. Zatsepin and V.A. Kuzmin. Upper limit of the spectrum of cosmic rays. *JETP Lett.*, 4:78–80, 1966.

[4] V.S. Berezinsky and G.T. Zatsepin. Cosmic rays at ultrahigh-energies (neutrino?). *Phys.Lett.*, B28:423–424, 1969.

[5] Christopher T. Hill and David N. Schramm. The Ultrahigh-Energy Cosmic Ray Spectrum. *Phys.Rev.*, D31:564, 1985.

[6] Ralph Engel, David Seckel, and Todor Stanev. Neutrinos from propagation of ultrahigh-energy protons. *Phys.Rev.*, D64:093010, 2001.

[7] K. Kotera, D. Allard, and A.V. Olinto. Cosmogenic Neutrinos: parameter space and detectabilty from PeV to ZeV. *JCAP*, 1010:013, 2010.

[8] C. Grupen. Astroparticle physics. 2005.

[9] J. Bluemer, R. Engel, and J.R. Hoerandel. Cosmic Rays from the Knee to the Highest Energies. *Prog.Part.Nucl.Phys.*, 63:293–338, 2009.

[10] F. Arqueros et al. Energy spectrum and chemical composition of cosmic rays between 0.3-PeV and 10-PeV determined from the Cherenkov light and charged particle distributions in air showers. *Astron.Astrophys.*, 359:682–694, 2000.

[11] Tadeusz Wibig and Arnold W. Wolfendale. At what particle energy do extragalactic cosmic rays start to predominate? *J.Phys.G*, G31:255–264, 2005.

[12] R.U. Abbasi et al. Measurement of the flux of ultrahigh energy cosmic rays from monocular observations by the High Resolution Fly's Eye experiment. *Phys.Rev.Lett.*, 92:151101, 2004.

[13] A. Creusot. Latest results of the Pierre Auger Observatory. *Nucl.Instrum.Meth.*, A662:S106–S112, 2012.

[14] D. Ikeda. Results from the Telescope Array Experiment. *Astrophys.Space Sci.Trans.*, 7:257–263, 2011.

[15] J.G. Learned and K. Mannheim. High-energy neutrino astrophysics. *Ann.Rev.Nucl.Part.Sci.*, 50:679–749, 2000.

[16] John F. Beacom, Nicole F. Bell, Dan Hooper, Sandip Pakvasa, and Thomas J. Weiler. Measuring flavor ratios of high-energy astrophysical neutrinos. *Phys.Rev.*, D68:093005, 2003.

[17] Q.R. Ahmad et al. Measurement of charged current interactions produced by ^{8}B solar neutrinos at the Sudbury Neutrino Observatory. *Phys.Rev.Lett.*, 87:071301, 2001.

[18] Bernhard Voigt. Sensitivity of the IceCube Detector for Ultra-High Energy Electron-Neutrino Events. 2008.

[19] Eli Waxman. Cosmological origin for cosmic rays above 10**19-eV. *Astrophys.J.*, 452:L1–L4, 1995.

[20] L.V. Volkova. Energy Spectra and Angular Distributions of Atmospheric Neutrinos. *Sov.J.Nucl.Phys.*, 31:784–790, 1980.

[21] G. Battistoni, A. Ferrari, T. Montaruli, and P.R. Sala. High-energy extension of the FLUKA atmospheric neutrino flux. 2003.

[22] G. Fiorentini, Vadim A. Naumov, and F.L. Villante. Atmospheric neutrino flux and muon data. 2001.

[23] Vivek Agrawal, T.K. Gaisser, Paolo Lipari, and Todor Stanev. Atmospheric neutrino flux above 1-GeV. *Phys.Rev.*, D53:1314–1323, 1996.

[24] M. Honda, T. Kajita, K. Kasahara, and S. Midorikawa. Calculation of the atmospheric neutrino flux improved with recent cosmic ray observations. pages 1162–1165, 2001.

[25] C.G.S. Costa. The Prompt lepton cookbook. *Astropart.Phys.*, 16:193–204, 2001.

[26] Vadim A. Naumov. Atmospheric muons and neutrinos. pages 31–46, 2002.

[27] P. Gondolo, G. Ingelman, and M. Thunman. Charm production and high-energy atmospheric muon and neutrino fluxes. *Astropart.Phys.*, 5:309–332, 1996.

[28] S.I. Sinegovsky, O.N. Petrova, and T.S. Sinegovskaya. High-energy spectrum and zenith-angle distribution of atmospheric neutrinos. 2011.

[29] M. Honda, T. Kajita, K. Kasahara, and S. Midorikawa. Calculation of the flux of atmospheric neutrinos. *Phys.Rev.*, D52:4985–5005, 1995.

[30] G. Battistoni, A. Ferrari, T. Montaruli, and P.R. Sala. The FLUKA atmospheric neutrino flux calculation. *Astropart.Phys.*, 19:269–290, 2003.

[31] R. Abbasi et al. The Energy Spectrum of Atmospheric Neutrinos between 2 and 200 TeV with the AMANDA-II Detector. *Astropart.Phys.*, 34:48–58, 2010.

[32] R. Abbasi et al. Measurement of the atmospheric neutrino energy spectrum from 100 GeV to 400 TeV with IceCube. *Phys.Rev.*, D83:012001, 2011.

[33] Bettina Hartmann. Reconstruction of Neutrino-Induced Hadronic and Electromagnetic Showers with the ANTARES Experiment. 2006.

[34] Amy Connolly, Robert S. Thorne, and David Waters. Calculation of High Energy Neutrino-Nucleon Cross Sections and Uncertainties Using the MSTW Parton Distribution Functions and Implications for Future Experiments. *Phys.Rev.*, D83:113009, 2011.

[35] Raj Gandhi, Chris Quigg, Mary Hall Reno, and Ina Sarcevic. Neutrino interactions at ultrahigh-energies. *Phys.Rev.*, D58:093009, 1998.

[36] Raj Gandhi, Chris Quigg, Mary Hall Reno, and Ina Sarcevic. Ultrahigh-energy neutrino interactions. *Astropart.Phys.*, 5:81–110, 1996.

[37] K. Nakamura et al. Review of particle physics. *J.Phys.G*, G37:075021, 2010.

[38] Amanda Cooper-Sarkar, Philipp Mertsch, and Subir Sarkar. The high energy neutrino cross-section in the Standard Model and its uncertainty. *JHEP*, 1108:042, 2011.

[39] Atri Bhattacharya, Raj Gandhi, Werner Rodejohann, and Atsushi Watanabe. The Glashow resonance at IceCube: signatures, event rates and pp vs. $p\gamma$ interactions. *JCAP*, 1110:017, 2011.

[40] Ulrich F. Katz and Christian Spiering. High-Energy Neutrino Astrophysics: Status and Perspectives. *Prog.Part.Nucl.Phys.*, 67:651–704, 2012.

[41] The KM3NeT Consortium. Detector Simulations for KM3NeT, Work Package D, V2.3, 2011. Internal note available online at `http://www.km3net.org/internal.php`; visited on June 18th 2012.

[42] Antares homepage. Available from `http://antares.in2p3.fr`; visited on June 26th 2012.

[43] J.A. Aguilar et al. AMADEUS - The Acoustic Neutrino Detection Test System of the ANTARES Deep-Sea Neutrino Telescope. 2010.

[44] P. Bagley et al. (The KM3NeT Consortium). Conceptual Design Report, 208. Available online at `http://www.km3net.org`; visited on July 6th 2012.

[45] P. Bagley et al. (The KM3NeT Consortium). Technical Design Report, 2011. Available online at `http://www.km3net.org`; visited on July 6th 2012.

[46] Teresa Montaruli Annalisa L'Abbate and Igor Sokalski. GENHEN v6: ANTARES neutrino generator extension to all neutrino flavors and inclusion of propagation through the Earth, 2004. ANTARES internal note.

[47] Teresa Montaruli Konstantin Kuzmin and Igor Sokalski. GENHEN v6r3: implementation of the Glashow resonance and of the MUSIC transport code, 2004. ANTARES internal note.

[48] David J.L. Bailey. Genhen v5r1: Software Documentation, 2002. ANTARES internal note.

[49] ANTARES Collaboration. Geasim, 2012. Available online at `http://antares.in2p3.fr/internal/dokuwiki/doku.php?id=geasim`; visited on June 25th 2012.

[50] S. Agostinelli et al. Geant4 - a simulation toolkit. *Nuclear Instruments and Methods in Physics Research Section A: Accelerators, Spectrometers, Detectors and Associated Equipment*, 506(3):250 – 303, 2003.

[51] S. Biagi. Simulation of MC events: Electron Neutrinos and NC, Jan. 2008. Talk on ANTARES Collaboration Meeting in Pisa.

[52] M. Spurio. ν_e-CC, ν_x-NC productions: KM3 vs geasim, Jan. 2008. Talk on ANTARES Collaboration Meeting in Pisa.

[53] F. Folger G. de Bonis. GEASIM: OPA vs noOPA, Nov. 2011. Talk on ANTARES Collaboration Meeting in Strasbourg.

[54] Geant4 Collaboration. Geant4 user documentation, 2012. Available online at `https://geant4.web.cern.ch/geant4/support/userdocuments.shtml`; visited on June 25th 2012.

[55] Valentin Niess and V. Bertin. Underwater acoustic detection of ultrahigh energy neutrinos. *Astropart.Phys.*, 26:243–256, 2006.

[56] J. Brunner. Cherenkov Light from HE Electromagnetic and Hadronic Showers, 2002. ANTARES internal note.

[57] Christopher Henrik V. Wiebusch. The Detection of faint light in deep underwater neutrino telescopes. 1995.

[58] L.D. Landau and I. Pomeranchuk. Electron cascade process at very high-energies. *Dokl.Akad.Nauk Ser.Fiz.*, 92:735–738, 1953.

[59] Florian Folger. Reconstruction of neutrino induced hadronic showers with the ANTARES neutrino telescope, 2009. Diploma thesis. University of Erlangen-Nuremberg, Germany.

[60] Thomas Seitz. Detector simulation studies for the KM3NeT neutrino telescope, 2009. Diploma thesis. University of Erlangen-Nuremberg, Germany.

[61] Ralf Auer. Reconstruction of hadronic cascades in large-scale neutrino telescopes. *Nucl.Instrum.Meth.*, A602:84–87, 2009.

[62] Sebastian Kuch. Design studies for the KM3NeT neutrino telescope. 2007.

[63] Donald E. Groom, Nikolai V. Mokhov, and Sergei I. Striganov. Muon stopping power and range tables 10-MeV to 100-TeV. *Atom.Data Nucl.Data Tabl.*, 78:183–356, 2001.

[64] S. Iyer Dutta, M.H. Reno, I. Sarcevic, and D. Seckel. Propagation of muons and taus at high-energies. *Phys.Rev.*, D63:094020, 2001.

[65] V. Barger, J. Learned, and S. Pakvasa. IceCube Neutrino Initiated Cascade Events: PeV Electron-antineutrinos at Glashow Resonance. 2012.

Danksagung

Ich danke in erster Linie meiner Freundin Aurélie für alles, insbesondere die mentale Unterstützung, und meiner Familie, die mich sicherlich auch sehr unterstützt hat.

In zweiter Linie danke ich Uli Katz und meinem Betreuer Rezo, die mir beide jegliche Freiheiten ließen und mindestens ein offenes Ohr für jede Frage hatten.

In dritter Linie danke ich meinen Zimmergenossen Lew Classen und Jonas Reubelt die, sofern anwesend, immer bereit waren über jede Frage und jedes Problem zu diskutieren. Insbesondere danke ich Jonas sowohl für Bilder, diverse Zeitfahren und Bergankünfte u.ä. als auch für die kreativsten Tafelbemalungen.

In vierter Linie danke ich allen Leuten im Institut und um mich herum, insbesondere Robert Lahmann und Thomas Seitz für die Korrekturlesungen.

In fünfter Linie danke ich Roland Richter und Björn Herold, die mich hier grad nerven während ich diese Zeilen schreibe.

In sechster Linie danke ich all meinen Freunden.

In siebter Linie ...

...

In tausendster Linie danke ich Frau Angela Merkel und ihrem Kabinett, das die Gelder für Bildung und Forschung noch auf einem Niveau hält, das mir ermöglicht, auch meine Promotion am ECAP durchzuführen, einem Ort, an dem man sich sehr wohl und geborgen fühlt. Manchmal zu wohl ...

Erklärung

Hiermit bestätige ich, dass ich diese Arbeit selbstständig und nur unter Verwendung der angegebenen Literatur und Hilfsmittel angefertigt habe.

Erlangen, 25.07.2012

Dominik Stransky